

# **Towards Scalable Electronic Devices with Sorted Carbon Nanotube Thin-Films**

by

*HeeBong Yang*

A thesis

presented to the University Of Waterloo

in fulfilment of the

thesis requirement for the degree of

Master of Applied Science

in

Electrical and Computer Engineering

Waterloo, Ontario, Canada, 2019

© HeeBong Yang 2019

## **Declaration**

I hereby declare that I am the sole author of this thesis. This is a true copy of the thesis, including any required final revisions, as accepted by my examiners.

I understand that my thesis may be made electronically available to the public.

## Abstract

The year 2021 is the 30<sup>th</sup> anniversary of carbon nanotube (CNT) discovery in 1991 by Sumio Iijima. CNTs, a cylindrical hollow shape, exhibit fascinating electrical and optical properties. CNTs have been at the heart of the fundamental research and engineering applications in various studies last three decades. Especially, CNTs are attractive because they have unique electronic structures which show different band gap energy as a function of their size. Nevertheless, we face two serious technical challenges with regards creating large-scale electronic and photonic devices using CNTs. First, we need to solve a sorting problem to extract a specific size of CNTs. Second, we have to control the alignment and orientation of sorted CNTs. Here, we present research progresses to master a sorting technique and to form an aligned CNT thin-film followed by device fabrication and characterization of sorted films.

We decide to apply aqueous two-phase extraction (ATPE) method to purify various CNT synthesis sources. ATPE shows strong advantages in scalability and relatively simple and low-cost processing steps over other methods. We manage to achieve high purity metallic and semiconducting CNTs in large volumes. We attempt a vacuum filtration method to make thin-films with sorted CNT solutions for devices. Although we need a transferring step to place films on substrates, we enjoy the flexibility to choose a variety of substrate form factors with size and thickness control.

In order to characterize electrical performance of CNT films, we fabricate planar two-terminal devices using different sizes of metallic and semiconducting CNT films with and without alignment. We examine the film quality and basic electrical performance via DC resistance and low frequency noise properties from temperature-dependent measurements. Our lessons are that aligned CNT film devices behave better than other conditions in terms of smaller resistance and more linear-like current-voltage characteristics at low temperatures. All film devices follow the  $1/f$  noise behavior and we will pursue further quantitative assessment of their noise properties in depth. We envision that we will make high performance quantum devices based on sorted CNT thin-films.

## Acknowledgements

I would like to thank all the people who made this thesis possible.

First of all, I would like to express the deepest appreciation to my advisor Prof. Na Young Kim. Prof. Kim gives me a lot of opportunities to learn various fields. Especially, Prof. Kim brings me from industry to academia studying further and deeper. The door to Prof. Kim office was always open whenever I ran into a trouble spot or had a question about my research or writing. She consistently allowed this paper to be my own work but steered me in the right direction whenever she thought I needed it.

I would like to thank the readers for this thesis Prof. Bo Cui and Prof. Christopher Wilson for their time. I am grateful for their thoughts and reviews.

I would like to thank Dr. Jeffrey A. Fagan who guides and advises ATPE process.

I would like to thank all our group members: Mats Powlowski, Dr. Taehyun Yoon, Dr. Daniel D. Kang, Alan James Malcolm, Aaron Gross, Marko Pejic, Steven Gassner, Nina Brown.

I would like to thank collaborators: Prof. Michael Pope and Prof. Pope's group member (Luzhu Xu, Azam Nasr) and Prof. Junichiro Kono and Prof. Kono's group member (Dr. Weilu Gao and Natsumi Komatsu)

I would also like to thank all QNFCF staffs, Peter Sprenger, Deler Langenberg, Don Carkner, Francois Sfigakis, Mohsen Asad, Dr. Hyun Ho Kim, Dr. Ho Sung Kim, Dr. Long Cheng who helps me to fabricate and characterize samples.

Finally, I would express my very profound gratitude to my parents, wife's parents and to my wife and children for providing me with unfailing support and continuous encouragement throughout my years of study and through the process of researching and writing this thesis.

This accomplishment would not have been possible without them. Thank you.

# Contents

<b>List of Tables</b>	<b>ix</b>
<b>List of Figures</b>	<b>x</b>
<b>Abbreviations</b>	<b>xv</b>
<b>1 Introduction</b>	<b>1</b>
<b>2 Carbon Nanotubes</b>	<b>3</b>
2.1 History of Carbon Nanotubes . . . . .	3
2.2 Carbon and Carbon Allotropes . . . . .	4
2.3 Types of Carbon Nanotube . . . . .	6
2.4 Electronic Properties of Carbon Nanotube . . . . .	7
2.4.1 Uniqueness of Carbon Nanotube's Electric Property . . . . .	7
2.4.2 Band Structure of Graphene and Carbon Nanotube . . . . .	9
2.5 Energy Band . . . . .	13
2.5.1 Secular Equation . . . . .	14
2.5.2 Tight Binding Method in Graphene . . . . .	16
2.5.3 Carbon Nanotube Energy Band with Boundary Conditions . . . . .	20

<b>3</b>	<b>Preparation of Sorted Carbon Nanotubes</b>	<b>25</b>
3.1	Methods of Carbon Nanotube Synthesis . . . . .	26
3.1.1	Arc Discharge (ADC) . . . . .	26
3.1.2	Laser Ablation (LA) . . . . .	27
3.1.3	Chemical Vapour Deposition (CVD) . . . . .	28
3.1.4	Other Chemical methods : High Pressure Carbon Monoxide® (HiPCO) and Cobalt-Molybdenum Catalyst®(CoMoCAT) . . . . .	28
3.1.5	Summary of Synthesis Methods . . . . .	29
3.2	Sorting Methods . . . . .	30
3.2.1	Ion Exchange Chromatography . . . . .	31
3.2.2	Density Gradient Ultracentrifugation (DGU) . . . . .	31
3.2.3	Selective Extraction . . . . .	32
<b>4</b>	<b>Aqueous Two-Phase Extraction (ATPE)</b>	<b>34</b>
4.1	Principle . . . . .	35
4.1.1	Polymers and Phase Diagram . . . . .	35
4.2	Process . . . . .	41
4.2.1	Schemaitc of ATPE Process and Result with Surfactant Concen- tration . . . . .	42
4.2.2	Pre-Process: Make SWNT Solution and Prepare Stocks . . . . .	43
4.2.3	Main Process: Proceed aqueous two-phase extraction (ATPE) Re- peatably . . . . .	45
4.2.4	Post-Process: Characterize solution for chirality and do polymer exchange . . . . .	48
4.3	Optical Characterization . . . . .	48
4.3.1	Absorption Spectroscopy . . . . .	50
4.3.2	Background Extraction . . . . .	51
4.3.3	Analysis with Protocol through Background Extraction . . . . .	53
4.3.4	Raman Spectroscopy . . . . .	54
4.3.5	Separation Results by Aqueous Two-Phase Extraction . . . . .	56

<b>5</b>	<b>Preparation of Carbon Nanotube Films</b>	<b>67</b>
5.1	Methods of making films . . . . .	67
5.1.1	Direct Deposition . . . . .	67
5.1.2	Solution-Based Deposition . . . . .	68
5.2	Method of making films: Vacuum filtration . . . . .	69
5.2.1	Preparing Apparatus and Solution . . . . .	69
5.2.2	Making Film with Vacuum Filtration . . . . .	70
5.2.3	Transferring on a Substrate . . . . .	71
5.2.4	Alignment Film: Another Advantage of Vacuum Filtration . . . . .	72
5.3	Characterization of Films . . . . .	74
5.3.1	Film Thickness and Surface Roughness . . . . .	74
5.3.2	Surface observation by Scanning Electron Microscope (SEM) . . . . .	76
5.3.3	Resistance and Resistivity with Two-Probe Measurement . . . . .	77
5.3.4	Resistance with Four-Probe Measurement . . . . .	79
5.3.5	Resistance with Annealing Effect . . . . .	80
<b>6</b>	<b>Carbon Nanotube Film Electronics</b>	<b>83</b>
6.1	Motivation . . . . .	83
6.2	Low Frequency Noise . . . . .	84
6.2.1	Types of Noises . . . . .	84
6.2.2	$1/f$ Noise and Random Telegraph Noise in Low Frequency Noise . . . . .	85
6.3	Device Design . . . . .	87
6.4	Device Fabrication . . . . .	88
6.4.1	Preparing Substrates . . . . .	88
6.4.2	Preparing Carbon Nanotube Pads . . . . .	89
6.4.3	Metallization . . . . .	90
6.5	Device Characterization . . . . .	91
6.5.1	Fabrication Results . . . . .	91

6.5.2	I-V Characteristics . . . . .	93
6.5.3	Temperature-Dependent Resistance . . . . .	95
6.5.4	Low Frequency Noise . . . . .	95
6.6	Discussions . . . . .	97
<b>7</b>	<b>Conclusion</b>	<b>101</b>
7.1	Summary . . . . .	101
7.2	Future Work . . . . .	102
	<b>References</b>	<b>103</b>
	<b>APPENDICES</b>	<b>113</b>
<b>A</b>		<b>114</b>
A.1	Preparing Substrates from 4-inch Wafer . . . . .	114
A.2	History of Devices . . . . .	115
<b>B</b>		<b>116</b>
B.1	SWNT Table [90, 31] . . . . .	116
B.2	Physical Constant . . . . .	117

# List of Tables

2.1	Table of carbon allotropes [78]. . . . .	6
2.2	Table of parameters for carbon nanotube (CNT) [78]. . . . .	21
3.1	Table of comparison of synthesis methods of CNTs [74] . . . . .	32
4.1	Information of carbon nanotubes which we used for ATPE [46, 47, 48, 45, 44] . . . . .	45
4.2	Table of information of stocks for ATPE [25]. . . . .	45
4.3	Recipes of preparation steps [18]. *NI (NanoIntegris), SA (Sigma-Aldrich)	46
4.4	Raman modes in SWNTs [23]. . . . .	57
4.5	Absorbance data for common color solutions from SG65i and SG76. . . . .	61
4.6	Absorbance data for simple sorting process with SG65i. . . . .	63
4.7	Absorbance data for simple sorting process with HiPCO. . . . .	63
5.1	Resistance and resistivity comparison between CNT films. . . . .	80
A.1	Table of CNT device history. . . . .	115
B.1	Table of SWNT transition energy and wavelength. . . . .	116

# List of Figures

2.1	Hybridized orbital by combination of $s$ orbital and $p$ orbital . . . . .	4
2.2	Electron configuration of carbon and three different hybridizations. Each arrow represents the spin of electron. . . . .	5
2.3	Structure of hybridizations. . . . .	6
2.4	Types of CNTs. (Reprinted with permission from reference [57]. Copyright 2017 Elsevier Ltd.) . . . . .	7
2.5	(a) Energy diagrams and DOS for metallic and semiconducting SWNTs. (Reprinted with permission from reference [30].) (b) The Kataura plot which shows the relations between a diameter of single-walled nanotube (SWNT)s and energy band gap. Open circles are semiconducting, solid circles are metallic, and double circles are armchair metallic SWNTs. (Reprinted with permission from reference [54]. Copyright 1999 Elsevier Science S.A..) . . . . .	8
2.6	Images of real and reciprocal space of graphene sheet. (a) Real space in a graphene. (b) Reciprocal space in a graphene. . . . .	10
2.7	Structure of spread CNT with $\vec{C}_h$ and $\vec{T}$ and an example of chirality (6,2). . . . .	11
2.8	Series of chiral vectors on hexagonal lattice. . . . .	12
2.9	There are various band structure calculation methods and tight binding model will be used for carbon nanotube calculation [73] . . . . .	13
2.10	Hexagonal lattice for graphene in real space. The numbers represent the level of distance from carbon atoms in the unit cell. . . . .	17
2.11	Nearest neighbors in terms of atom $A$ in a unit cell. . . . .	18
2.12	Energy diagram of graphene as a result of $E_{g2D}$ with $\epsilon_{2p} = s = 0$ , and $t = 1$ . . . . .	19

2.13	Energy dispersion diagrams for armchair cases. (a) Energy dispersion for (5,5). (b) Energy dispersion for (10,10). . . . .	22
2.14	Energy dispersion diagrams for zigzag semiconducting cases. (a) Energy dispersion for (5,0). (b) Energy dispersion for (10,0). . . . .	23
2.15	Energy dispersion diagrams for zigzag metallic case. . . . .	23
2.16	Energy dispersion diagrams for (6,5) and (7,6). . . . .	24
3.1	Drawing of arc discharge synthesis method. (Reprinted with permission from reference [20].) . . . . .	26
3.2	Drawing of laser ablation synthesis method. (Reprinted with permission from reference [20].) . . . . .	27
3.3	Schematic of chemical vapor deposition synthesis method. (Reprinted with permission from reference [88].) . . . . .	29
3.4	Drawing of High Pressure Carbon Monoxide synthesis method. (Reprinted with permission from reference [14]. Copyright 2001 America Vacuum Society.) . . . . .	30
3.5	Sketches of a CoMoCAT synthesis method. (Reprinted with permission from reference [20].) . . . . .	31
3.6	Large diameter range in each SWNT synthesis method. (Reprinted with permission from reference [24]. Copyright 2013 Woodhead Publishing Limited..) . . . . .	33
4.1	Phase diagrams with two-different polymers. (a) General phase diagram. (Reprinted with permission from reference [7]. Copyright 2016 American Chemical Society.) (b) Phase diagram with and without surfactant in PEG 6 kDa and DX 70 kDa. (Reprinted with permission from reference [25].) (c) Phase diagram with and without surfactant in PEG 6 kDa and DX 70 kDa done by ourselves [21]. . . . .	37
4.2	Separation coefficient diagrams. (a) Separation coefficient with varied SDS concentration at fixed DOC for diameter separation. (Reprinted with permission from reference [25].) (b) Separation coefficient with varied SDS concentration at fixed SC for metallic and semiconducting separation. (Reprinted with permission from reference [25].) . . . . .	38

4.3	Chemical structure of SDS and DOC. (Reprinted with permission from reference [91]. Copyright 2004 WILEY-VCH Verlag GmbH & Co. KGaA, Weinheim.) . . . . .	39
4.4	Separation results in reduced or oxidized solutions. (Reprinted with permission from reference [33]. Copyright 2015 American Chemical Society.)	40
4.5	A schematic of separation of SWNTs in biphasic system. (Reprinted with permission from reference [25].) . . . . .	41
4.6	A schematic of ATPE process. (Reprinted with permission from reference [25].) . . . . .	42
4.7	The relation between the concentration of SDS and the diameter of SWNTs at a fixed DOC 0.45 %. (Reprinted with permission from reference [25].)	43
4.8	Generalization of ATPE process for CoMoCAT and HiPCO SWNTs. (Reprinted with permission from reference [25].) . . . . .	49
4.9	(a) Absorbance results with sorted solutions of SWNT. (Reprinted with permission from reference [27]. Copyright 2014 WILEY-VCH Verlag GmbH & Co. KGaA, Weinheim.) (b) Photoluminescence map of (6,5) SWNT solution. (Reprinted with permission from reference [6]. . . . .	51
4.10	Absorbance spectrum with background spectrum. (Reprinted with permission from reference [25].) . . . . .	52
4.11	Analysis protocol program of background extraction. [17] (a) Main control panel of analysis protocol program. (b) Plot of background extraction result. (c) Plot of deconvolution results. . . . .	55
4.12	Picture of the principle of Raman spectroscopy. (Reprinted with permission from reference [84].) (a) Image of scattering mode. (b) Image of position in wave number domain. . . . .	56
4.13	Common colors of ATPE separation results from SG65i and SG76. . . . .	58
4.14	Absorbance spectrum for common colors of ATPE separation results from SG65i and SG76. . . . .	59
4.15	RBM mode in Raman spectroscopy for common colors. . . . .	60
4.16	D and G mode in Raman spectroscopy for common colors. . . . .	60
4.17	Simple process sorting results with SG65i in bulk bottles. . . . .	62
4.18	Simple process sorting results with HiPCO SWNTs. . . . .	62

4.19	Absorbance comparison with and without polymer. . . . .	64
4.20	Raman spectroscopy RBM results of forest green solution with 532 nm and 632 nm incident laser. . . . .	65
4.21	Raman spectroscopy RBM results of purple solution with 532 nm and 632 nm incident laser. . . . .	66
5.1	(a) Vacuum filtration apparatus and (b) thickness of CNT films for reference solution. . . . .	70
5.2	(a) CNT film on a membrane after vacuum filtration (b) transfer on a substrate with vacuum filtrated film. . . . .	71
5.3	Recipe of transferring a CNT film on a substrate. . . . .	73
5.4	(a) atomic force microscopy (AFM) topological image of a CNT film on a silicon substrate. Width of the film is 30 $\mu\text{m}$ (b) The cross section of profiles at positions ① and ② indicated in Figure (a). . . . .	74
5.5	(a) Scanning the middle of the CNT film which is same in figure (4.4) (b) 3-dimension plotting for film surface. . . . .	75
5.6	A scheme of scanning a strain CNT with a bigger AFM tip. . . . .	76
5.7	(a) AFM result with small probe (b) Height of cross section for thickness measurements. . . . .	76
5.8	CNT films observation under SEM. (a) random direction of (6,5) dominant film (b) random direction of MWNT film (c) aligned with mixed SWNT film. . . . .	77
5.9	The schematic of a 2-terminal device. This is not a real size of ratio. . . .	78
5.10	Resistivity results of 2-terminal measurement for SWNT film devices with different design factors: (a) for the width and (b) for the gap. . . . .	79
5.11	Resistance comparison before and after annealing for four different MWNT films. . . . .	81
6.1	Types of noises in a frequency domain [60]. . . . .	85
6.2	Fabrication process - Case 1. . . . .	92
6.3	Fabrication process - Case 2. . . . .	92

6.4	(a) The microscope image of overall fabricated devices. Scale bar is 200 $\mu\text{m}$ (b) Zoomed in view of microscope image for the device width 10 $\mu\text{m}$ and gap 250 nm. Scale bar is 10 $\mu\text{m}$ . (c) SEM image of observation of gap for the device whose design values are width 10 $\mu\text{m}$ and gap 250 nm. Scale bar is 100 nm. . . . .	93
6.5	I-V measurement results for four cases at room temperature and low temperature. All the measurements are voltage sweep results. (a) Results for case 1. Voltage range is -200 mV to 200 mV, interval 1 mV. (b) Results for case 2. Voltage range is -200 mV to 200 mV, interval 1 mV. (c) Results for case 3. Voltage range is -1 V to 1 V, interval 1 mV. (d) Results for case 4. Voltage range is -100 mV to 100 mV, interval 1 mV. . . . .	94
6.6	Temperature-dependent resistance measurements results. Four cases results are normalized by room temperature resistance and represents as a function of temperature. Inset reprinted plot removing case 1 in order to adjust range of y-axis. . . . .	95
6.7	Graphical user interface of low frequency analysis coding python [29]. . .	96
6.8	PSD data of each case with different temperatures. . . . .	97
6.9	(a) Log-log plot of temperature-dependent resistivity from SWNT film fitting with VRH and FIT. (Reprinted with permission from reference [9]. Copyright 2010 American Physical Society.) (b) Log-log plot of temperature-dependent relative resistance from our device results. . . . .	98
6.10	1/f noise coefficient, $A/R$ and $\beta$ comparison between cases. . . . .	99
A.1	(a) Drawing for multiple 1 cm by 1 cm substrates. (b) Drawing for an 1 cm by 1 cm substrate. . . . .	114

# Abbreviations

**ADC** arc discharge 25–27

**AFM** atomic force microscopy xiii, 74, 75, 80

**Al** Aluminum 84

**ATPE** aqueous two-phase extraction vi, 2, 25, 32–36, 40–48, 54, 56, 59, 63, 64, 101, 102

**ATPS** aqueous two-phase system 36

**Au** gold 78, 87

**CNT** carbon nanotube ix, 2–7, 9–11, 13, 20, 21, 25–31, 43–46, 56, 67–75, 77–80, 83, 84, 86–91, 94, 101, 102, 114

**CNTFET** carbon nanotube field-effect transistor 2

**CO** carbon monoxide 29

**Co** cobalt 26, 29

**CoMoCAT** cobalt and molybdenum catalysts and CO gases 25, 28, 29, 32, 45, 47, 57, 73

**CVD** chemical vapor deposition 3, 25, 28, 30, 45, 67

**Da** dalton 35

**DGU** density gradient ultracentrifugation 32, 34, 35

**DI** deionized water 89, 90

**DMD** digital mirror device 89

**DOC** sodium deoxycholate 32, 35–43, 45–48, 72

**DOS** density of states 7, 8, 22–24

**DWNT** double-walled nanotube 6

**DX** dextran 34–36, 38–41, 45–48

**EBL** e-beam lithography 90, 91, 115

**Fe** iron 26

**Fe(CO)<sub>5</sub>** iron pentacarbonyl 29

**FIT** fluctuation-induced tunneling 97, 98

**GaAs** Gallium arsenide 8

**gcd** greatest common divisor 11, 21

**GUI** graphic user interface 53

**He** helium 27

**HiPCO** high pressure carbon monoxide 25, 28, 29, 32, 45, 47, 57, 61

**InP** indium phosphide 8

**IPA** isopropyl alcohol 72, 88–91

**IR** infrared 83

**LA** laser ablation 25, 27

**LB** Langmuir-Blodgett 68, 79, 80, 115

**MLA** Maskless aligner 89, 90, 115

**Mo** molybdenum 29

**MOSFET** metal-oxide-semiconductor field-effect transistor 1

**MQW** Milli-Q water 44, 45, 71

**MWNT** multi-walled nanotube 3, 4, 6, 7, 25–27, 43, 76, 77, 79, 80, 82–84, 87, 115

**NaClO** sodium hypochlorite 35, 38, 40, 45, 47, 59

**Nb** niobium 87

**Ni** nickel 26

**NIST** National Institute of Standards and Technology 34

**NMP** N-Methyl-2-Pyrrolidone 70, 72, 89

**Pd** palladium 78, 87

**PECVD** plasma enhanced chemical vapor deposition 28

**PEG** polyethylene glycol 34–36, 38–41, 45–48

**PSD** power spectral density 85, 86, 96, 97, 99

**PVP** polyvinylpyrrolidone 70, 72

**QNFCF** Quantum-Nano Fabrication and Characterization Facility 88, 101

**qubit** quantum bit 83, 84

**RBM** radial breathing mode 56–58, 65

**RIE** reactive-ion etching 89

**SC** sodium cholate 32, 35, 37–40, 43, 45–48

**SDS** sodium dodecyl sulfate 35–42, 45–48

**SEM** scanning electron microscope 3, 74, 76, 77, 91, 93

**Si** silicon 1

**SWNT** single-walled nanotube [x](#), [xi](#), [2–8](#), [12](#), [13](#), [22](#), [25–43](#), [45–48](#), [50](#), [52–54](#), [56](#), [57](#), [64](#), [65](#), [70](#), [72](#), [74–80](#), [82–84](#), [87](#), [91](#), [93](#), [94](#), [98](#), [100–102](#), [115](#)

**TEM** transmission electron microscope [3](#), [77](#)

**Ti** titanium [87](#), [88](#)

**UV** ultraviolet [83](#), [88](#), [89](#)

**VF** vacuum filtration [69–71](#), [78](#), [115](#)

**VHS** van Hove singularities [7](#), [8](#)

**VRH** variable-range hopping [97](#), [98](#)

# Chapter 1

## Introduction

The history of human beings evolves with the discovery of materials. The first age of a specific material occurred in the Stone Age, when people made knapped stones for use in hunting. Next in the Bronze Age and the Iron Age, people used fire cast weapons and household items with bronze and iron each era. At this point, people who discovered and were good at dealing with new materials ruled territories and led the era. We observe a similar phenomenon in our Modern Age. When we consider the evolutionary progresses of transistors which are the main part of integrated circuits in computers, [silicon \(Si\)](#) has had an indispensable role in making transistors. Especially, since [metal-oxide-semiconductor field-effect transistor \(MOSFET\)](#) was invented in 1959 by Mohamed Atalla and Dawon Kahng at Bell Labs [67], [Si](#) has been cemented as a king of materials. There is no compatible material substituting [Si](#) which is as abundant in the earth and non-toxic for the environment with reasonable mobility and energy band gap. Because all electrical equipment has this [Si](#) circuit, this current era is called "the Silicon Age", the successor of the Iron Age. This impactful material has governed the whole world over 60 years. It is not visibly or physically enforced like war in prehistoric era rather than it permeates in our lives without recognition and conquers contemporary people all over the world. This phenomenon implies the history of human beings is not made by man-kind, but by dominant material. Therefore, we think searching for and developing a good material is a worthwhile task for a scientist.

We usually refer to Moore's law predicted by Gordon Moore, who is a co-founder of Intel, when we discuss the development of computers [65]. This law says the number of transistors in a integrated circuit doubles every 18 months, in other words, integrated circuits get smaller exponentially. So far this has held true, but we are talking about the next generation of integrated circuits as physically the size of [Si](#) transistors seem

almost at the end of their limit. For the next generation material, we study CNTs. Scientists have called CNTs a promising material since Sumio Iijima discovered CNTs in 1991 [42], which triggered a boom of research into CNTs. This material has outstanding electrical, chemical, mechanical, and optical properties. Thanks to these properties, an article was published recently which demonstrated another improved carbon nanotube field-effect transistor (CNTFET) computer. Although it was not the first demonstration, this demonstration confirms CNT is a viable material in future computers [37]. Specifically, SWNT, which is one form of CNT, can be either metallic or semiconducting depending on the chirality of the CNT, and the semiconducting SWNT has different band gap energies so that we can manipulate them for different applications.

In order to separate SWNTs into metallic or semiconducting groups, or even one specific chirality, we need to sort them because synthesis does not result in a homogenized target. Among many methods, I performed ATPE which is able to separate them by diameter, or metallic or semiconducting status, in a relatively economic way and at a large volume. By using sorted metallic and semiconducting SWNTs [25], we benchmarked electrical devices in the former, we have fabricated and characterized CNT two-terminal electrical devices.

With these motivations, we introduce general information of CNTs in Chapter 2 and Chapter 3: what CNT is and its properties in Chapter 2, and synthesis and sorting in Chapter 3. Specifically, we will discuss one sorting method, ATPE, in Chapter 4. In Chapter 5, fabrication and characterization of CNT film are discussed and device level discussions are presented in Chapter 6.

# Chapter 2

## Carbon Nanotubes

CNT is a member of the carbon family which includes: fullerene which is a zero-dimensional structure of  $C_{60}$  discovered in 1985, graphene which has a two-dimensional structure, and CNT which is a one-dimensional structure.

### 2.1 History of Carbon Nanotubes

CNTs are widely known to have been discovered by Sumio Iijima, in the form of multi-walled nanotube (MWNT) in 1991, and form of SWNT in 1993 [42, 43]. Although Iijima gave scientists all over the world the chance to study these materials by introducing carbon cylindrical tube structures called 'microtubules', CNTs, similar carbon tubule structures were clearly observed in 1952 in the form of the MWNTs which were 50 nm diameter and detected by transmission electron microscope (TEM) [75]. As those were discovered by two Russian scientists publishing in a Russian journal, the Journal of Physical Chemistry of Russia, and it was during the Cold War period, this discovery was not widely distributed amongst the world wide research communities. Until publishing the papers by Iijima, there were several other discoveries in 1976, 1981, and 1987. The first SWNT, grown by a chemical vapor deposition (CVD) like method, was observed by Oberlin *et al.* under a scanning electron microscope (SEM)[71]. Russian scientists found that CNTs consist of graphene wrapped like into a cylindrical shape in 1981 and Howard Tennet applied for a patent of this cylindrical shape as carbon fibrils [75].

After fullerene had a spotlight in 1985 when it was first discovered and published, and then Kroto, Curl, and Smalley got a Nobel prize in 1996 [59], CNTs were starting to get attention from 1991 when Sumio Iijima observed MWNTs [42]. These have diameters which range from 4 to 30 nm, and were named microtubules of graphitic carbon initially. Iijima and his colleague Ichihashi observed SWNTs, whose diameter was around 1 nm two years later, in 1993 [43]. Although these discoveries by Iijima were not the first, they were what caused huge interest in scientists all over the world because CNTs show outstanding electrical and mechanical properties with nano-size scale.

## 2.2 Carbon and Carbon Allotropes

Electrons in atoms occupy orbitals following Hund's rules, filling from the lowest energy level orbitals first. However, there are different orbitals forming between  $2s$  orbital and  $2p$  orbitals through hybridization. These hybridized orbitals are made by combination of  $s$  orbital and  $p$  orbitals in Fig.2.1.



Figure 2.1: Hybridized orbital by combination of  $s$  orbital and  $p$  orbital

CNTs are made of carbon atoms whose symbol is 'C', atomic number is 6, and that have 6 electrons, located in group 4 and period 2 in the Periodic table. According to the electron configuration in  $s$  and  $p$  orbitals  $1s^2 2s^2 2p^2$ , it has four outer electrons [78]. Even though carbon itself is non-metal element, carbon allotropes show either metallic or semiconducting properties according to the formation of electron orbitals and carbon structures. These 4 electrons in  $2s$  orbital and  $2p$  orbitals transform into orbitals which is called 'Hybridization' in order to minimize the total energy level and angular momentum. There are three different hybridization forms as shown in Fig.2.2.

Depending on the number of hybridized orbitals, the hybridization name and structure are denoted,  $sp$ -,  $sp^2$ -, and  $sp^3$ -hybridization. In case of  $sp^2$ -hybridization, there are three  $sp^2$  orbitals and one  $2p_z$  orbital to minimize angular momentum. Carbon atoms are connecting through these hybridized orbitals presenting in Fig.2.3.

$sp$ -,  $sp^2$ -, and  $sp^3$ -hybridization form linear, trigonal planar, and tetrahedral structures, respectively. These structures are found in different allotropes of carbon as

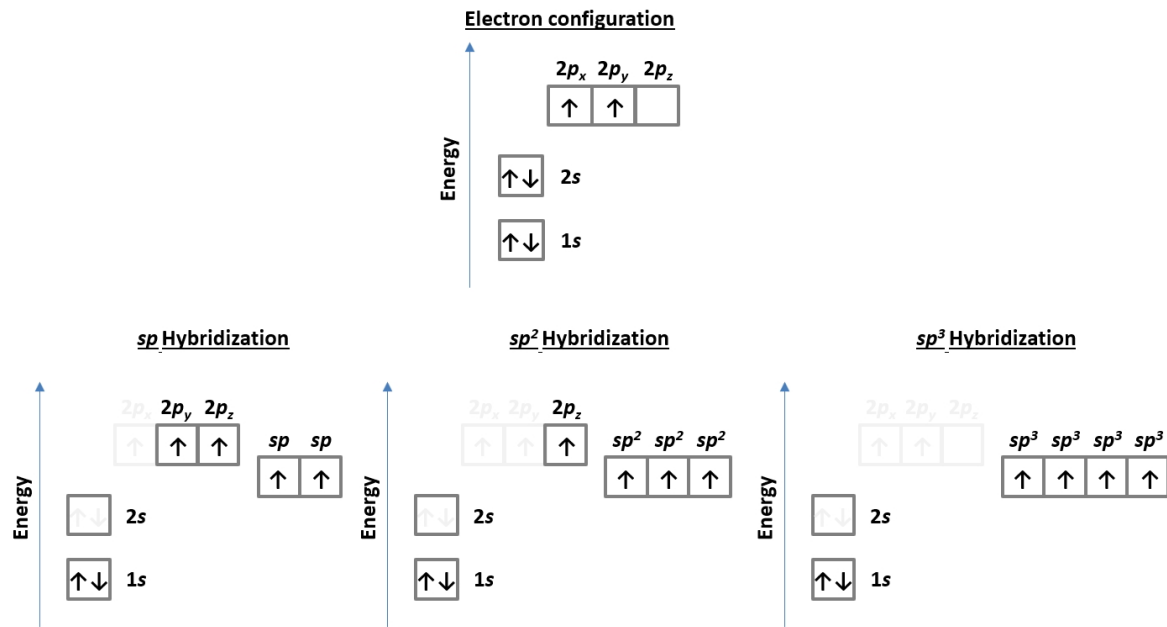


Figure 2.2: Electron configuration of carbon and three different hybridizations. Each arrow represents the spin of electron.

shown in Table 2.1. Carbon allotropes are grouped by dimension from 0-dimension to 3-dimension. They can also be classified by hybridization:  $sp^3$  is a well-known orbital which is common in diamond,  $sp$  is carbyne which is predicted but it is under study, and  $sp^2$  shows three different allotropes, fullerene, graphene, and carbon nanotube. This  $sp^2$  hybridization basically has a trigonal planar structure but allotropes are divided by form of dimension, sphere for fullerene, cylinder for carbon nanotube, and plane for graphene. Interestingly, CNTs have unique electronic properties of metals or semiconductors. Even among semiconducting SWNTs, the band gap energy can vary because the band gap energy is defined according to the chirality, which will be further explained in section 2.4. On the other hand, fullerene is a semiconductor with fixed band gap energy 1.9 eV and graphene is semi-metal with zero band gap energy.

These CNT properties arise from  $sp^2$  hybridization, specifically determined by the  $p_z$  orbital. This is explained by a tight binding model of with boundary conditions along the circumferal direction of CNTs.

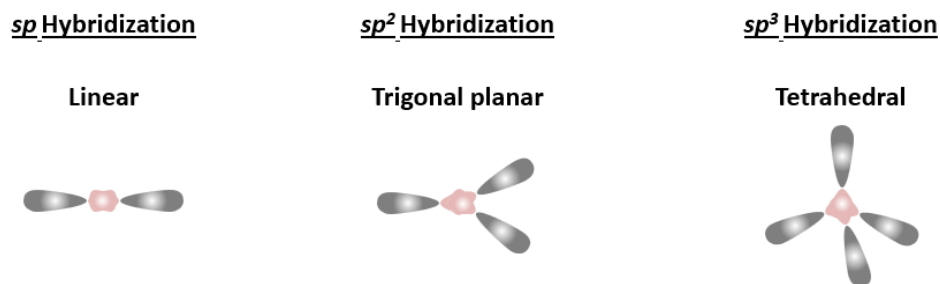


Figure 2.3: Structure of hybridizations.

Dimension	0-D	1-D	2-D	3-D
Allotropes	Fullerene	Carbon Nanotube / Carbyne	Graphene	Diamond
Hybridization	$sp^2$	$sp^2 / sp$	$sp^2$	$sp^3$
Density [g/cm <sup>3</sup> ]	1.72	1.2-2.0 / 2.68-3.13	2.26	3.515
Bond length [Å]	1.40 (C=C)	1.44 (C=C)	1.42 (C=C)	1.54 (C-C)
Electronic properties	Semiconductor $E_g=1.9\text{eV}$	Metal or semiconductor	Semimetal	Insulator $E_g=5.47\text{eV}$

Table 2.1: Table of carbon allotropes [78].

## 2.3 Types of Carbon Nanotube

CNT is a so called one-dimensional material because it has a cylindrical shape with diameter 0.7 - 10.0 nm and length which lie on the nano-meter to centi-meter scale. Normally the ratio of length and diameter is  $10^4 - 10^5$ , this is the reason why we call CNT a one-dimensional structure. In order to imagine this structure, we are able to think of a cylindrical shape like a prolonged version of zero-dimension of fullerene or a 2-dimension graphene sheet which is rolled up. CNTs are composed by a hexagonal lattice outer shell and hollow interior. There are interesting features depending on the number of wrapping sheets: SWNT for one sheet, double-walled nanotube (DWNT) for two sheet, and MWNT for more than three sheets in Fig.2.4 [57]. Apparently, the number of sheets is increased, the diameter become thicker. Generally, the thickness of SWNT is thinner than 2 nm. Furthermore, SWNT and DWNT show either semicon-

ducting or metallic properties depending on the chirality [78, 87]. On the other hand, MWNTs are known to be metallic [92].

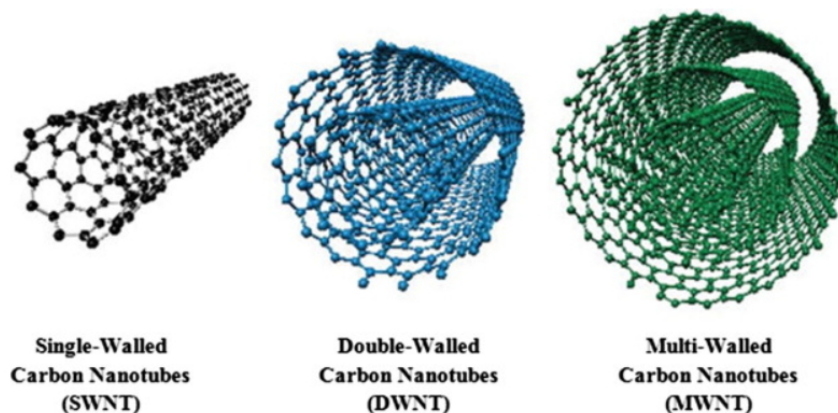


Figure 2.4: Types of CNTs. (Reprinted with permission from reference [57]. Copyright 2017 Elsevier Ltd.)

## 2.4 Electronic Properties of Carbon Nanotube

### 2.4.1 Uniqueness of Carbon Nanotube's Electric Property

CNTs, especially SWNTs have a unique electrical property; unlike other materials, they can be metallic or semiconducting with various band gap energy values depending on the chirality. This is a powerful advantage in material because other materials have their own determined energy band gap so that we have to search different material if we need specific band gap energies.

Fig.2.5(a) represents energy diagrams of semiconducting and metallic SWNTs matched with density of states (DOS) [30]. As we know, the metallic materials do not have band gap energy due to the touched energy diagram, whereas, the semiconducting diagram has the gap between valence band and conduction band. When we take it account the DOS, there are non-smooth points attributed to van Hove singularities (VHS). Energy transitions occur between these flat areas and generate band gap energies. And interesting result is that metallic SWNTs have also band gap energies.

According to the Kataura plot explanation [54], different diameters of SWNTs are matched with different band gap energies and even metallic SWNTs have band gap

energies due to VHS in the DOS. A smaller diameter SWNT has higher band gap energy and there are several electric transitions which are denoted transition levels such as  $E_{11}$ ,  $E_{22}$ ,  $E_{33}$ , and  $E_{44}$ , where  $E_{11}$  is the transition between the first valence and conduction band. It is also separate metallic and semiconducting cases,  $M_{11}$ ,  $M_{22}$ ,  $M_{33}$ , and  $M_{44}$  for metallic and  $S_{11}$ ,  $S_{22}$ ,  $S_{33}$ , and  $S_{44}$  for semiconducting, because the range of energy gaps varies. And as the transition energy value is larger, the energy gap is higher. For diameter between 0.7 and 1 nm in  $S_{11}$  case, the band gap energy range is 1.00 - 1.42 eV, which corresponds to near infrared wavelength range, 873 - 1240 nm [90]. In Fig.2.5(b), we can see the range of band gap energies depending on the diameter and transition type. Open circles are semiconducting, solid circles are metallic, and double circles are armchair metallic.  $S_{11}$  is starting from the bottom open circle plot.

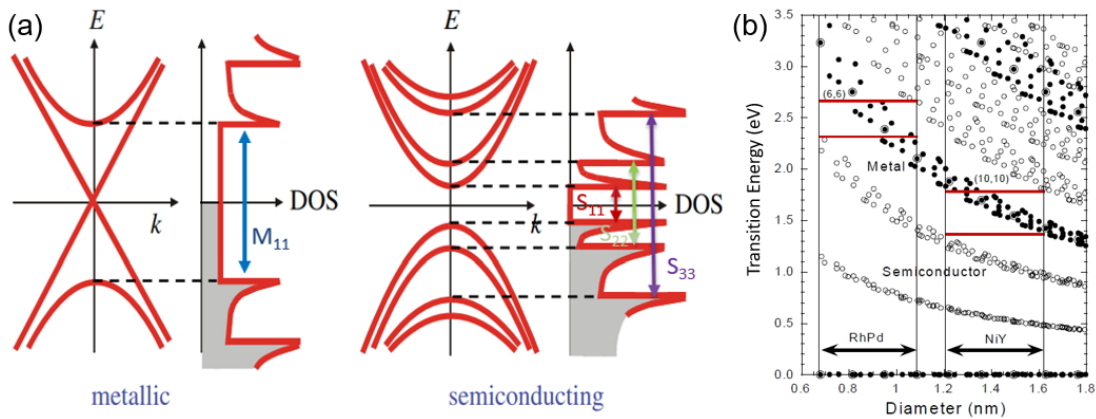


Figure 2.5: (a) Energy diagrams and DOS for metallic and semiconducting SWNTs. (Reprinted with permission from reference [30].) (b) The Kataura plot which shows the relations between a diameter of SWNTs and energy band gap. Open circles are semiconducting, solid circles are metallic, and double circles are armchair metallic SWNTs. (Reprinted with permission from reference [54]. Copyright 1999 Elsevier Science S.A..)

Gallium arsenide (GaAs) and indium phosphide (InP) are able to be substituted by SWNTs regarding energy band. Since band gap energy of GaAs is 1.43 eV which is similar  $S_{11}$  band gap for chirality (6,4) and energy band of InP is 1.35 eV which is  $S_{11}$  band gap for chirality (9,1). This energy band gap associated with diameter is coming from the boundary condition of circumferential direction. We will discuss the details in energy band calculation section.

## 2.4.2 Band Structure of Graphene and Carbon Nanotube

This section describes the band structure of CNTs. Graphene is a mother material of CNTs so that we start with a graphene bands structure and impose a specific periodic boundary condition to derive the CNT band structure.

### Graphene

Starting with a graphene structure is a simple way to figure out the CNT structure. As can be seen in Fig.2.6, graphene is a single sheet of carbon hexagonal arrays which is coming from carbon  $sp^2$  hybridization. The typical starting point is to define two primitive vectors,  $\vec{a}_1$  and  $\vec{a}_2$ , which in real space are not orthogonal and so require special care or attention when we calculate energy bands and express vector form and position,

$$\vec{a}_1 = \left(\frac{\sqrt{3}}{2}a, \frac{1}{2}a\right), \quad \vec{a}_2 = \left(\frac{\sqrt{3}}{2}a, -\frac{1}{2}a\right).$$

where  $a = |\vec{a}_1| = |\vec{a}_2|$ . Note that  $a$  is not the distance between carbon atoms which is denoted as  $a_{c-c}$ . Distances ( $a_{c-c}$ ) for graphene and CNT are different as CNTs are curved whereas graphene is planar.  $a_{c-c}$  in graphene is 1.42 Å and in CNT is 1.44 Å. A unit cell is drawn using four adjacent hexagonals with a rhombus shape connected four centers of hexagons. This unit cell contains two carbon atoms, which is a starting point of the band structure calculation.  $\vec{R}_i, (i = 1, 2, 3)$  in Fig.2.6(a) are vectors to describe positions of nearest-neighbor carbon atoms explicitly specified,

$$\vec{R}_1 = \left(-\frac{\sqrt{3}}{6}a, \frac{1}{2}a\right), \quad \vec{R}_2 = \left(-\frac{\sqrt{3}}{6}a, -\frac{1}{2}a\right), \quad \vec{R}_3 = \left(\frac{1}{\sqrt{3}}a, -\frac{1}{2}a\right).$$

Regarding reciprocal space, there are two reciprocal lattice vectors,  $\vec{b}_1$  and  $\vec{b}_2$ , defined by the relation between primitive vectors and reciprocal lattice vectors,  $\vec{a}_i \cdot \vec{b}_j = 2\pi\delta_{ij}$ . The Brillouin zone is a hexagonal shape as in Fig.2.6(b). There are three crucial points, which are called critical points or high symmetry points, in reciprocal space which are denoted as  $\Gamma$ ,  $K$ , and  $M$ . The  $\Gamma$  point represents the center of the Brillouin zones,  $K$  points are the corners of a hexagonal lattice in 2-dimension, and  $M$  points are center of a hexagonal lattice edge [41, 13, 79]. The triangle made by  $\Gamma$ ,  $K$ , and  $M$  is called "Irreducible Brillouin Zone" which is the crucial and smallest zone not being folded anymore. Due to the hexagonal geometry, this is three-fold rotation symmetry so that an edge point is not folded right next edge point. Therefore, the inequivalent  $K'$  exists.

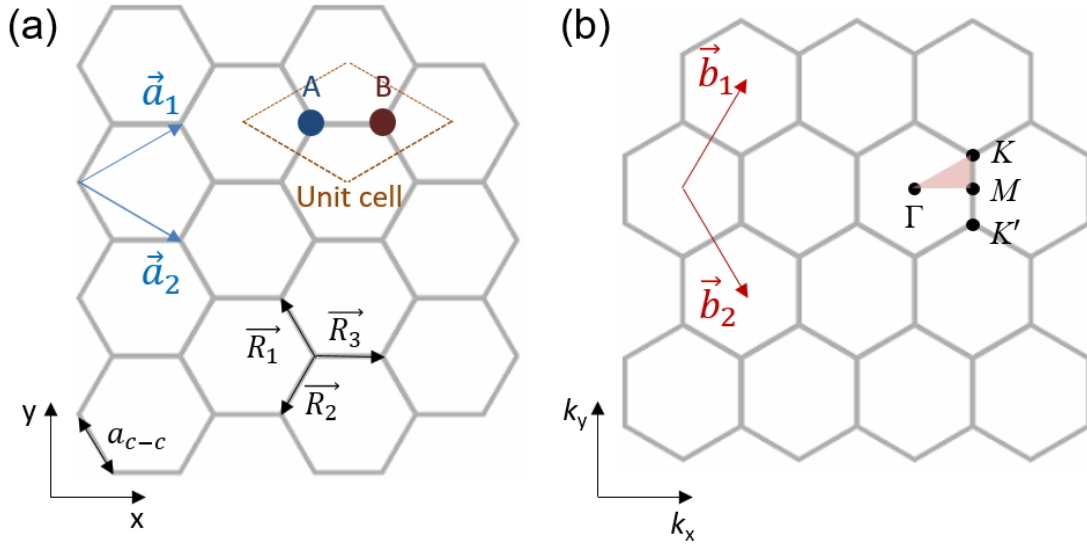


Figure 2.6: Images of real and reciprocal space of graphene sheet. (a) Real space in a graphene. (b) Reciprocal space in a graphene.

### Carbon Nanotube

As the CNT structure is cylindrical, it can be spread like a graphene sheet and examined with graphene information. Using the primitive vectors,  $\vec{C}_h$  which is a chiral vector and written in terms of the primitive vectors of a graphene denote like,  $\vec{a}_1$  and  $\vec{a}_2$ ,

$$\vec{C}_h = n\vec{a}_1 + m\vec{a}_2 \equiv (n, m), \quad (2.1)$$

where  $n$  and  $m$  are integers. In this case,  $\vec{C}_h$  can be a circumference of the CNT. Then, the diameter is calculated as,

$$\text{diameter } d_t = \frac{|\vec{C}_h|}{\pi} = \frac{\sqrt{(\vec{C}_h \cdot \vec{C}_h)}}{\pi} = \frac{a\sqrt{n^2 + m^2 + nm}}{\pi}. \quad (2.2)$$

The angle between  $\vec{a}_1$  and  $\vec{a}_2$  is  $60^\circ$ , where should be careful to calculate because it is normally  $90^\circ$  for common unit vectors. In order to express the longitudinal axis of CNT, translational vector, we introduce a  $\vec{T}$ , which is perpendicular to the chiral vector.

Using the perpendicular relation between two vectors,  $\vec{C}_h \cdot \vec{T} = 0$ ,  $\vec{T}$  is represented by definition in terms of  $\vec{a}_1$  and  $\vec{a}_2$ ,

$$\vec{T} = t_1 \vec{a}_1 + t_2 \vec{a}_2 \equiv (t_1, t_2), \quad (2.3)$$

where  $t_1 = \frac{2m+n}{d_R}$ ,  $t_2 = -\frac{2n+m}{d_R}$ .  $d_R$  is defined as **greatest common divisor (gcd)**( $2n+m, 2m+n$ ) of two integers from  $2n+m$  and  $2m+n$ . The relation of two integers,  $2n+m$  and  $2m+n$ , can be expressed by  $(n-m)$ , whether  $(n-m)$  is multiples of 3 or not. If  $(n-m)$  is the number of multiple of 3,  $d_R = \text{gcd} = (n, m)$ . If  $(n-m)$  is not the number of multiples of 3,  $d_R = \text{gcd}(n, m) \times 3$ .

Let's consider an explicit example. Fig.2.7 shows a CNT with chirality (6,2) unrolled into a graphene sheet. The primitive vectors,  $\vec{C}_h$  and  $\vec{T}$  are directly drawn and the values  $(n, m)$  and  $(t_1, t_2)$  are written. Then two vectors,  $\vec{C}_h$  and  $\vec{T}$ , define a red-colored rectangular region, a unit cell of a CNT.

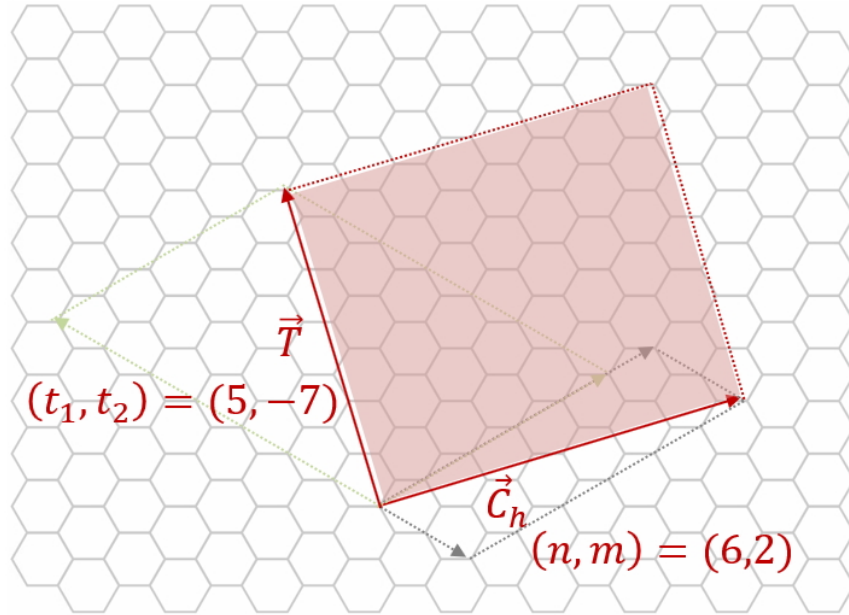


Figure 2.7: Structure of spread CNT with  $\vec{C}_h$  and  $\vec{T}$  and an example of chirality (6,2).

Fig.2.8 includes the series of  $\vec{C}_h$  at a same hexagonal lattice. Chiral vectors are located between  $0^\circ$  and  $30^\circ$  when  $n \geq m$ , and the angle is defined from the 'Zigzag' direction to chiral vector. On the other hand,  $n \leq m$ , the angle range between  $30^\circ$  and  $60^\circ$ ,

is mirror symmetry case we call as an enantiomer. Because the ‘Zigzag’ is represented simply by  $\vec{a}_1$ , the angle can be expressed with a cosine form,

$$\cos \theta = \frac{\vec{C}_h \cdot \vec{a}_1}{|\vec{C}_h| |\vec{a}_1|} = \frac{2n + m}{2\sqrt{n^2 + m^2 + nm}}. \quad (2.4)$$

When we look into chiral vector series, we can group metallic and semiconducting SWNTs by chirality. If  $(n - m)$  is multiples of 3, it is metallic and marked with red dots in Fig. 2.8, whereas semiconducting SWNTs are marked with blue dots. Specifically, there are two symmetric chirality cases which are  $(n, n)$  and  $(n, 0)$ . As can be seen shapes in the figure, interesting names were coined such as  $(n, n)$  for an ‘Armchair’ and  $(n, 0)$  for a ‘Zigzag’ SWNT. Only  $n = \text{multiple of } 3$  in zigzag cases are metallic, whereas all armchairs are metals.

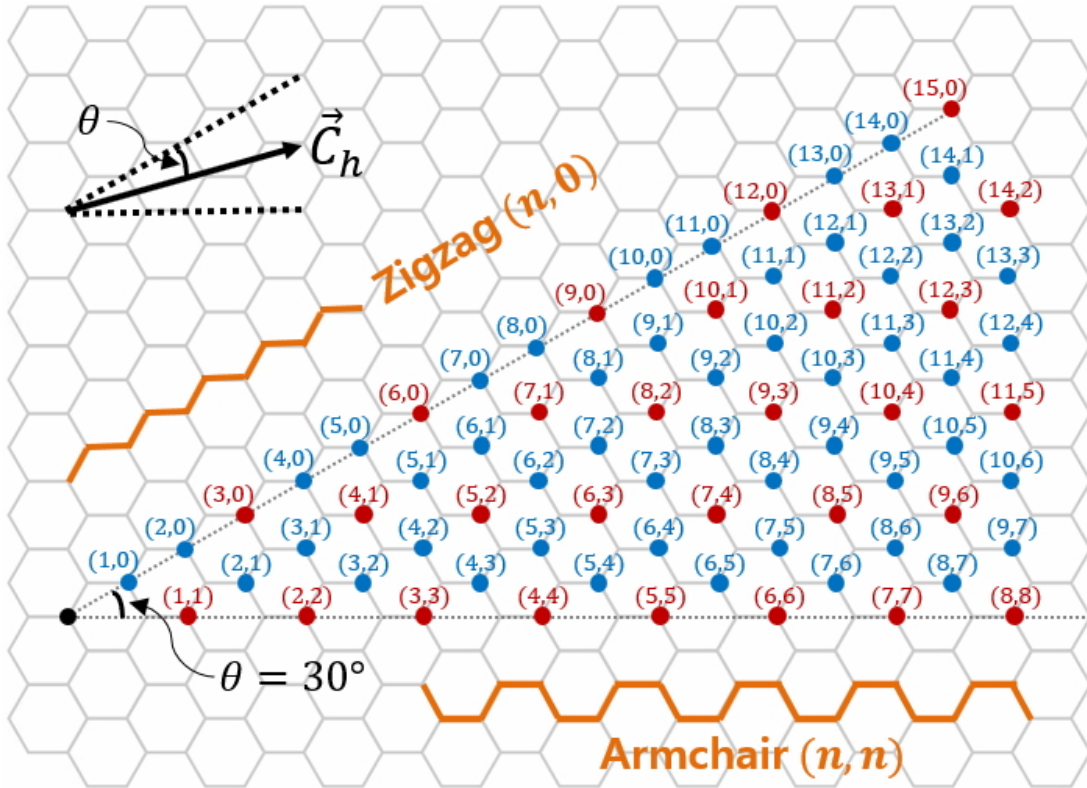


Figure 2.8: Series of chiral vectors on hexagonal lattice.

## 2.5 Energy Band

Energy band calculation of CNT is done by a tight binding method among various methods in Fig.2.9 [73]. A tight binding model is one of the methods based on atomic orbitals which periodic potential is strong enough where an electron in an atom is bounded so that it is calculated as lattices or atomic orbitals. As CNT is formed by  $sp^2$  hybridization and each carbon atom has  $p_z$  orbital and carbon atoms form the hexagonal lattice, tight binding model is applied for energy band calculation of CNT.

Energy band calculations are basically solving a secular equation of Hamiltonian matrix (section 2.5.1). After we layout the mathematical framework of secular equation calculation explicitly, whose method is first applied to calculate graphene band structure (section 2.5.2), followed by a SWNT band structure (section 2.5.3)

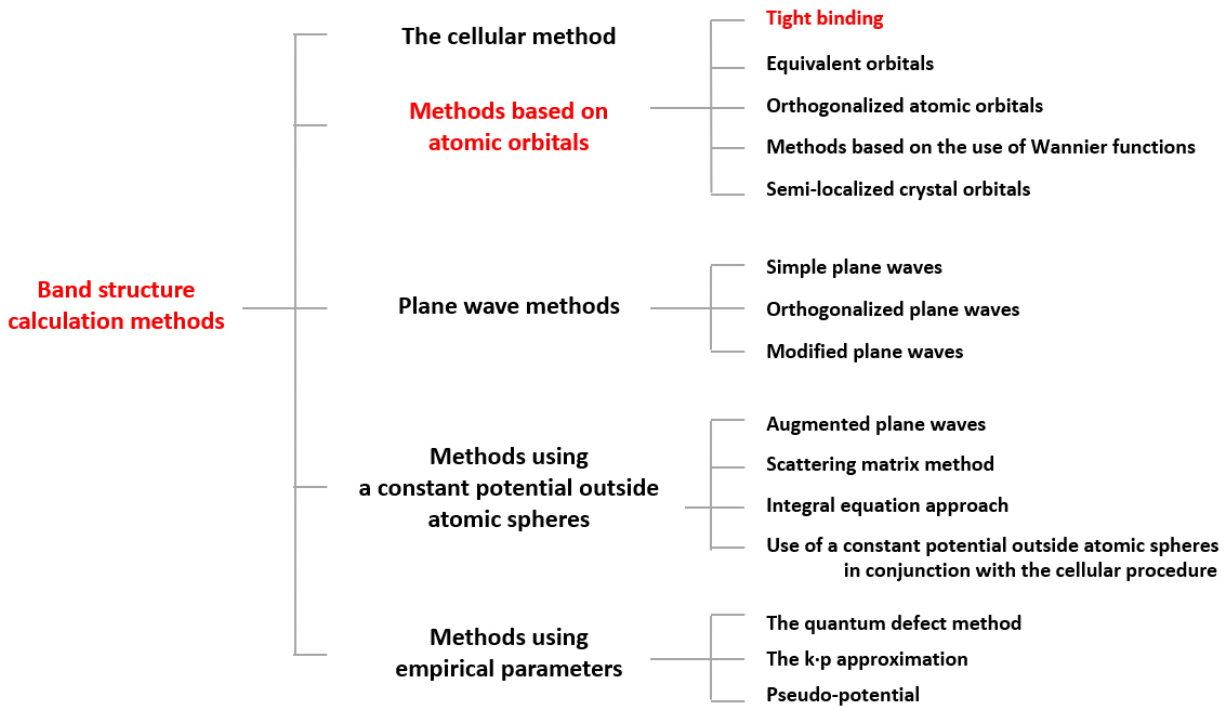


Figure 2.9: There are various band structure calculation methods and tight binding model will be used for carbon nanotube calculation [73]

## 2.5.1 Secular Equation

A wave function  $\Psi$  is required to meet a Bloch's theorem in a crystal due to the translational crystal structure symmetry for the direction of the lattice vector  $\vec{a}_j$ ,

$$T_{\vec{a}}\Psi = e^{i\vec{k}\cdot\vec{a}_j}\Psi_j, \quad (2.5)$$

where  $\vec{a}_j$  is lattice vectors ( $j = 1, 2, 3$ ),  $\Psi$  is any wave function of the lattice,  $T_{\vec{a}}$  is translational operator along the lattice vector  $\vec{a}_j$ , and  $\vec{k}$  is a wave vector. A Bloch function  $\Phi_j(\vec{k}, \vec{r})$  is written as,

$$\Phi_j(\vec{k}, \vec{r}) = \frac{1}{\sqrt{N}} \sum_{\vec{R}} e^{i\vec{k}\cdot\vec{R}} \varphi_j(\vec{r} - \vec{R}), \quad (j = 1, \dots, n) \quad (2.6)$$

where  $\vec{R}$  is a position of the atom,  $\varphi_j$  is an atomic wavefunction in state,  $N$  is the number of unit cells, and  $n$  is the number of atomic wavefunctions in the unit cell.

Eq.(2.6) satisfies Eq.(2.5) as below.

$$\Phi_j(\vec{k}, \vec{r} + \vec{a}) = \frac{1}{\sqrt{N}} \sum_{\vec{R}} e^{i\vec{k}\cdot\vec{R}} \varphi_j(\vec{r} + \vec{a} - \vec{R}), \quad (2.7)$$

$$= e^{i\vec{k}\cdot\vec{a}} \frac{1}{\sqrt{N}} \sum_{\vec{R}-\vec{a}} e^{i\vec{k}\cdot(\vec{R}-\vec{a})} \varphi_j(\vec{r} + (\vec{R} - \vec{a})), \quad (2.8)$$

$$= e^{i\vec{k}\cdot\vec{a}} \Phi_j(\vec{k}, \vec{r}) \quad (2.9)$$

Then, the eigen function  $\Psi_j(\vec{k}, \vec{r})$  is represented by the sum of linear combination of Bloch functions,

$$\Psi_j(\vec{k}, \vec{r}) = \sum_{j'}^n C_{jj'}(\vec{k}) \Phi_{j'}(\vec{k}, \vec{r}), \quad (2.10)$$

where  $C_{jj'}$  is coefficient to be determined. As the energy eigenvalues can be expressed by Hamiltonian,

$$E_j(\vec{k}) = \frac{\langle \Psi_j | \mathcal{H} | \Psi_j \rangle}{\langle \Psi_j | \Psi_j \rangle} = \frac{\int \Psi_j^* \mathcal{H} \Psi_j dr}{\int \Psi_j^* \Psi_j dr}, \quad (2.11)$$

where  $\mathcal{H}$  is Hamiltonian.

Plugging Eq.(2.10) into Eq.(2.11),

$$E_i(\vec{k}) = \frac{\sum_{jj'=1}^n \mathbf{C}_{ij}^* \mathbf{C}_{ij'} \langle \Phi_j | \mathcal{H} | \Phi_{j'} \rangle}{\sum_{jj'=1}^n \mathbf{C}_{ij}^* \mathbf{C}_{ij'} \langle \Phi_j | \Phi_{j'} \rangle}, \quad (2.12)$$

$$= \frac{\sum_{jj'=1}^n \mathcal{H}_{ij'}(\vec{k}) \mathbf{C}_{ij}^* \mathbf{C}_{ij'}}{\sum_{jj'=1}^n \mathcal{S}_{ij'}(\vec{k}) \mathbf{C}_{ij}^* \mathbf{C}_{ij'}}. \quad (2.13)$$

Here we define  $\mathcal{H}_{ij'}(\vec{k})$  as transfer integral matrices and  $\mathcal{S}_{ij'}(\vec{k})$  as overlap integral matrices in Eq.(2.14) and Eq.(2.15).

$$\mathcal{H}_{ij'}(\vec{k}) = \langle \Phi_j | \mathcal{H} | \Phi_{j'} \rangle, \quad (2.14)$$

$$\mathcal{S}_{ij'}(\vec{k}) = \langle \Phi_j | \Phi_{j'} \rangle. \quad (2.15)$$

In order to minimize  $E_i(\vec{k})$ , the coefficient  $\mathbf{C}_{ij}^*$  should be optimized by using partial differentiation,

$$\frac{\partial E_i(\vec{k})}{\partial \mathbf{C}_{ij}^*} = \frac{\sum_{j'=1}^N \mathcal{H}_{jj'}(\vec{k}) \mathbf{C}_{ij'}}{\sum_{jj'=1}^N \mathcal{S}_{jj'}(\vec{k}) \mathbf{C}_{ij}^* \mathbf{C}_{ij'}} - \frac{\sum_{j,j'=1}^N \mathcal{H}_{jj'}(\vec{k}) \mathbf{C}_{ij}^* \mathbf{C}_{ij'}}{(\sum_{jj'=1}^N \mathcal{S}_{jj'}(\vec{k}) \mathbf{C}_{ij}^* \mathbf{C}_{ij'})^2} \sum_{j'=1}^n \mathcal{S}_{ij'}(\vec{k}) \mathbf{C}_{ij'} = 0 \quad (2.16)$$

By multiplying both side with  $\sum_{jj'=1}^N \mathcal{S}_{jj'}(\vec{k}) \mathbf{C}_{ij}^* \mathbf{C}_{ij'}$  and plugging in Eq.(2.13),

$$\sum_{j'=1}^N \mathcal{H}_{jj'}(\vec{k}) \mathbf{C}_{ij'} = E_i(\vec{k}) \sum_{j'=1}^N \mathcal{S}_{jj'}(\vec{k}) \mathbf{C}_{ij'} \quad (2.17)$$

Introducing the matrix form of  $\mathbf{C}_i$  as  $\mathbf{C}_i = \begin{pmatrix} C_{i1} \\ \vdots \\ C_{iN} \end{pmatrix}$ , Eq.(2.17) is simply written in terms matrix forms, reaching Eq.(2.18) as below.

$$\mathcal{H}\mathbf{C}_i = E_i(\vec{k})\mathcal{S}\mathbf{C}_i \quad (2.18)$$

In order to obtain the allowed energy,  $E_i(\vec{k})$ , we can make the formula all in the left side and rearrange them with common part,  $\mathbf{C}_i$ , then result is  $[\mathcal{H} - E_i(\vec{k})\mathcal{S}]\mathbf{C}_i = 0$ . If there is a inverse matrix of  $[\mathcal{H} - E_i(\vec{k})\mathcal{S}]$ ,  $\mathbf{C}_i$  should be a null vector which is not the eigenfunction. Therefore,  $[\mathcal{H} - E_i(\vec{k})\mathcal{S}]$  has not to have inverse matrix which we reach to the last equation, the secular equation in Eq.(2.19).

$$\det[\mathcal{H} - E_i(\vec{k})\mathcal{S}] = 0 \quad (2.19)$$

## 2.5.2 Tight Binding Method in Graphene

According to the secular equation method, we need to figure out 2 by 2 matrix for transfer integral matrix and overlap integral matrix so as to obtain the energy matrix. In terms of graphene case, there are two carbon atoms we need to think about as two carbon atoms exit in a unit cell.

When we look into 2 by 2 matrix of transfer integral matrix which is Hamiltonian  $\mathcal{H}_{ij}$ , ( $i, j = A, B$ ), there are four terms grouped by two, interaction between same folded atoms,  $\mathcal{H}_{AA}$  and  $\mathcal{H}_{BB}$ , and interaction between different folding atoms,  $\mathcal{H}_{AB}$  and  $\mathcal{H}_{BA}$ .

$$\mathcal{H} = \begin{pmatrix} \mathcal{H}_{AA} & \mathcal{H}_{AB} \\ \mathcal{H}_{BA} & \mathcal{H}_{BB} \end{pmatrix} \quad (2.20)$$

At first, the diagonal terms in the Hamiltonian can be explained sum of Hamiltonian which is applied certain position of carbon atom  $A$  in Fig.2.10 interacting same folding atoms, blue position atoms, 0 is the very itself position which is a most dominant term, 1 is the next nearest, etc. There are different distance results in a  $\mathcal{H}_{AA}$ , we can take the nearest term for further calculation because it is the most dominant term in the Hamiltonian. When we add normalized term  $\frac{1}{N}$ ,  $\mathcal{H}_{AA}$  can be expressed  $\epsilon_{2p}$  and is equal to  $\mathcal{H}_{BB}$ .

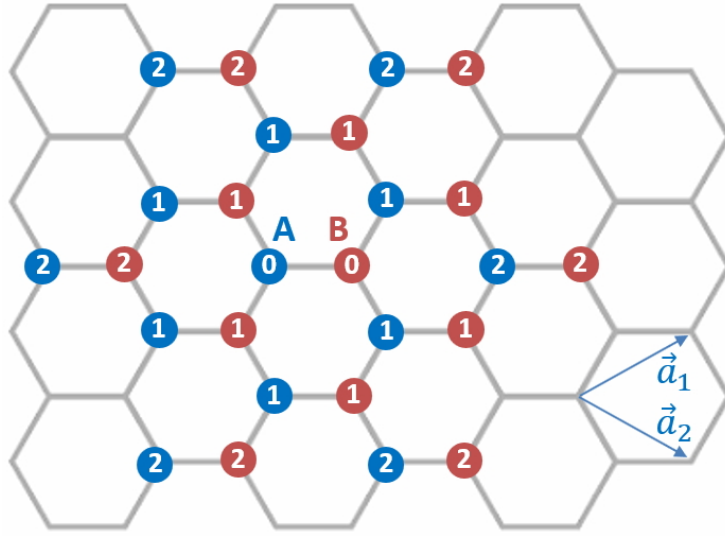


Figure 2.10: Hexagonal lattice for graphene in real space. The numbers represent the level of distance from carbon atoms in the unit cell.

$$\mathcal{H}_{AA}(r) = \frac{1}{N} \sum_{R,R'} e^{ik(R-R')} \langle \varphi_A(r-R') | \mathcal{H} | \varphi_A(r-R) \rangle, \quad (2.21)$$

$$= (\text{between blue interactions}) \textcircled{0} \text{ term} + \textcircled{1} \text{ terms} + \textcircled{2} \text{ terms} \cdots, \quad (2.22)$$

$$\cong \epsilon_{2p}, \quad (2.23)$$

$$= \mathcal{H}_{BB}(r). \quad (2.24)$$

The next part is off-diagonal terms between different folding atoms case. Methodology is same as  $\mathcal{H}_{AA}$  except interaction carbons. Suppose calculating  $\mathcal{H}_{AB}$ .  $A$  is the reference carbon atom, then there are three nearest carbon atoms which is positioned as  $R_i$  described brown colored  $\textcircled{1}$  in Fig.2.11. It is finally denoted as transfer integral  $t$  and phase factor  $f(k)$ ,

$$\mathcal{H}_{AB}(r) = \frac{1}{N} \sum_{i=1,2,3} \sum_R e^{i\vec{k} \cdot \vec{R}_i} \langle \varphi_A(r-R) | \mathcal{H} | \varphi_B(r-R_i) \rangle, \quad (2.25)$$

$$\cong t(e^{i\vec{k} \cdot \vec{R}_1} + e^{i\vec{k} \cdot \vec{R}_2} + e^{i\vec{k} \cdot \vec{R}_3}), \quad (2.26)$$

$$= tf(k) = \mathcal{H}_{BA}(r)^*. \quad (2.27)$$

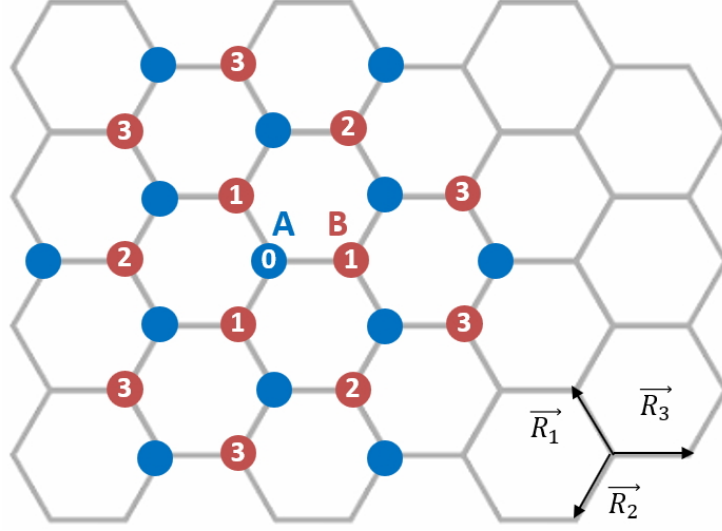


Figure 2.11: Nearest neighbors in terms of atom A in a unit cell.

where  $t = \langle \varphi_A(r-R) | \mathcal{H} | \varphi_B(r-R_i) \rangle$  and  $f(k)$  is simplified with  $k_x$  and  $k_y$  applying position vector  $\vec{R}_i$ ,

$$\vec{R}_1 = \left(-\frac{a}{2\sqrt{3}}, \frac{a}{2}\right), \quad \vec{R}_2 = \left(-\frac{a}{2\sqrt{3}}, -\frac{a}{2}\right), \quad \vec{R}_3 = \left(\frac{a}{\sqrt{3}}, 0\right),$$

$$f(k) = e^{i\vec{k} \cdot \vec{R}_1} + e^{i\vec{k} \cdot \vec{R}_2} + e^{i\vec{k} \cdot \vec{R}_3}, \quad (2.28)$$

$$= e^{\frac{ik_y a}{\sqrt{3}}} + 2e^{-\frac{ik_x a}{2\sqrt{3}}} \cos \frac{k_y a}{2}. \quad (2.29)$$

By definition of the overlap integral matrix  $\mathcal{S}$ , it can be derived same as the transfer integral matrix  $\mathcal{H}$ . Then,  $\mathcal{H}$  and  $\mathcal{S}$  are prepared for solution for  $E(\vec{k})$ .

$$\mathcal{H} = \begin{pmatrix} \epsilon_{2p} & tf(k) \\ tf(k)^* & \epsilon_{2p} \end{pmatrix}, \quad \mathcal{S} = \begin{pmatrix} 1 & sf(k) \\ sf(k)^* & 1 \end{pmatrix}. \quad (2.30)$$

Plugging these two results in secular equation, solutions of the eigenvalue  $E(\vec{k})$  can be expressed as below.

$$E_{g2D}(\vec{k}) = \frac{\epsilon_{2p} \pm t w(\vec{k})}{1 \pm s w(\vec{k})}, \quad (2.31)$$

where  $w(\vec{k}) = \sqrt{|f(\vec{k})|^2} = \sqrt{1 + 4 \cos \frac{\sqrt{3}k_x a}{2} \cos \frac{k_y a}{2} + 4 \cos^2 \frac{k_y a}{2}}$ . Here we take  $\epsilon_{2p} = 0$  and  $s = 0, t = 1$ , then  $E_{g2D}(\vec{k})$  becomes both  $\pi$  energy band which is positive sign result and anti- $\pi$  energy band which is negative sign result are symmetry and energy diagram of Eq (2.32) is shown in Fig.2.12.

$$E_{g2D}(k_x, k_y) = \pm t \sqrt{1 + 4 \cos \frac{\sqrt{3}k_x a}{2} \cos \frac{k_y a}{2} + 4 \cos^2 \frac{k_y a}{2}}, \quad (2.32)$$

There are six  $K$  points which are known as Dirac cone and  $\Gamma$  point at the center.

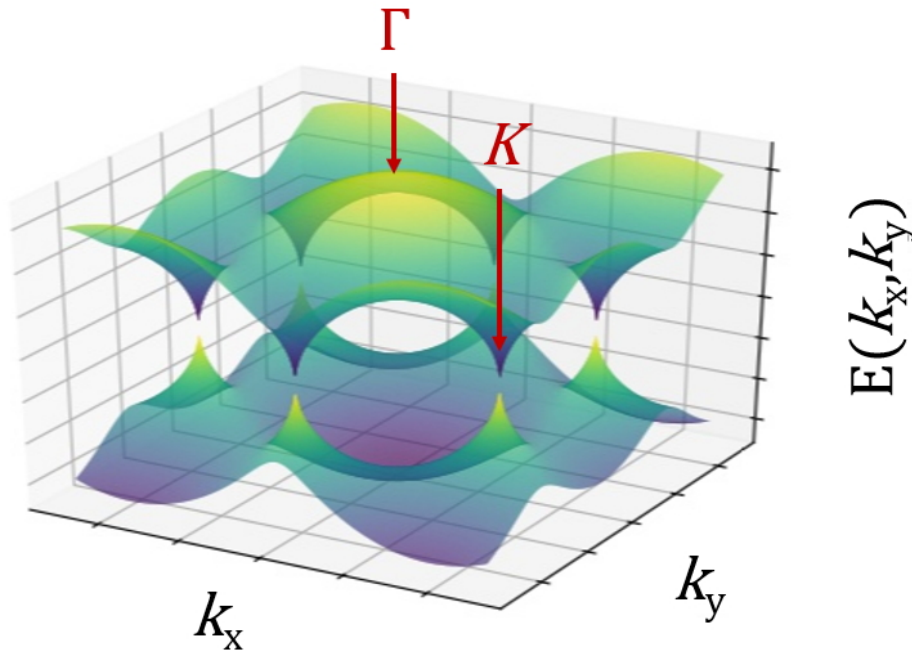


Figure 2.12: Energy diagram of graphene as a result of  $E_{g2D}$  with  $\epsilon_{2p} = s = 0$ , and  $t = 1$ .

### 2.5.3 Carbon Nanotube Energy Band with Boundary Conditions

CNTs' band structure calculation is starting from graphene's band structure calculation results. In addition, we need to take into account of the boundary conditions of CNTs because they are wrapped as cylindrical shape. According to the  $\vec{C}_h$ , circumference of CNT is determined and calculate energy dispersion of CNT  $E_\mu$ .

$$E_\mu(k) = E_{g2D}\left(k \frac{\vec{K}_2}{|\vec{K}_2|} + \mu \vec{K}_1\right), \quad (\mu = 0, \dots, N-1, \& -\frac{\pi}{T} < k < \frac{\pi}{T}) \quad (2.33)$$

Here, it looks it is consisted of two vectors, reciprocal vector for CNT  $\vec{K}_1$  and  $\vec{K}_2$ , but it is mainly impacted by  $\vec{K}_1$  because  $\vec{K}_2$  is just described different form and fixed, and the only  $\vec{K}_1$  can be varied and determine the  $E_\mu(k)$  depending on the  $\mu$  which comes from chirality.  $\vec{K}_1$  and  $\vec{K}_2$  are defined with  $\vec{C}_h$  and  $\vec{T}$  in CNT level. Following the formula between primary vector and reciprocal vector, primary vector and reciprocal vector in the CNT region relations can be described as below.

$$\begin{aligned} \vec{C}_h \cdot \vec{K}_1 &= 2\pi & \vec{C}_h \cdot \vec{K}_2 &= 0 \\ \vec{T} \cdot \vec{K}_1 &= 0 & \vec{T} \cdot \vec{K}_2 &= 2\pi \end{aligned} \quad (2.34)$$

$$\vec{K}_1 = \frac{1}{N_g}(-t_2 \vec{b}_1 + t_1 \vec{b}_2) \quad \vec{K}_2 = \frac{1}{N_g}(m \vec{b}_1 - n \vec{b}_2). \quad (2.35)$$

where,  $N_g$  is the number of hexagons per unit cell,  $N_g = \frac{2(n^2+m^2+nm)}{d_R}$ .

In Table 2.2, there is a summary of parameters for the energy band calculation for CNT.

#### Symmetry Carbon Nanotube Cases: Armchair and Zigzag

Symmetry CNT cases such as armchair which is  $(n, n)$  and zigzag which is  $(n, 0)$  are readily approached as the chiral vector direction is on the  $k_y$  and  $k_x$ , respectively. Based on the definition of relation between chirality vector and reciprocal lattice vector,  $\vec{C}_h$  is

Symbol	Name	Formula	Remark
$a$	length of unit vector	$a = \sqrt{3}a_{c-c} = 2.49\text{\AA}$	$a_{c-c} = 1.44\text{\AA}$
$\vec{a}_1, \vec{a}_2$	unit vectors	$(\frac{\sqrt{3}}{2}a, \frac{1}{2}a), (\frac{\sqrt{3}}{2}a, -\frac{1}{2}a)$	$x, y$ coordinate
$\vec{b}_1, \vec{b}_2$	reciprocal lattice vectors	$(\frac{2\pi}{\sqrt{3}a}, \frac{2\pi}{a}), (\frac{2\pi}{\sqrt{3}a}, -\frac{2\pi}{a})$	$x, y$ coordinate
$\vec{C}_h$	chiral vector	$\vec{C}_h = n\vec{a}_1 + m\vec{a}_2 \equiv (n, m)$	$0 \leq m \leq n$
$L$	length of $\vec{C}_h$	$L =  \vec{C}_h  = a\sqrt{n^2 + m^2 + nm}$	
$d_t$	diameter	$d_t = L/\pi$	
$d$	$\text{gcd}(n, m)$		
$d_R$	$\text{gcd}(2n + m, 2m + n)$	$d_R = \begin{cases} d, & \text{if } (n - m) \text{ is multiple of } 3d \\ 3d, & \text{if } (n - m) \text{ is not multiple of } 3d \end{cases}$	
$\vec{T}$	translational vector	$\vec{T} = t_1\vec{a}_1 + t_2\vec{a}_2 \equiv (t_1, t_2)$ $t_1 = \frac{2m+n}{d_R}, t_2 = -\frac{2n+m}{d_R}$	$\text{gcd}(t_1, t_2) = 1$
$N_g$	number of hexagons in the nanotube unit cell	$N_g = \frac{2(n^2+m^2+nm)}{d_R}$	
$\vec{K}_1, \vec{K}_2$	reciprocal lattice vectors for CNT	$\vec{K}_1 = \frac{1}{N_g}(-t_2\vec{b}_1 + t_1\vec{b}_2), \vec{K}_2 = \frac{1}{N_g}(m\vec{b}_1 - n\vec{b}_2)$	

Table 2.2: Table of parameters for CNT [78].

on the  $k_x$  for armchair case so that  $\vec{K}_1$  should be on the  $k_y$ .  $\vec{K}_1$  for zigzag case is on the  $k_x$  with similar manner. From this result, we can get boundary condition as,

$$n\sqrt{3}k_{x,q}a = 2\pi q, \quad (q = 1, \dots, 2n) \quad \text{for armchair} \quad (2.36)$$

$$nk_{y,q}a = 2\pi q, \quad (q = 1, \dots, 2n) \quad \text{for zigzag} \quad (2.37)$$

here  $q$  is integer which is smaller than  $N$ , the number of hexagons in the nanotube unit cell. Because armchair is  $(n, m)$  and zigzag is  $(n, 0)$ ,  $q$  for both cases are same as  $2n$ .

When we write Eq.(2.32) with Eq.(2.36) and Eq.(2.37), we can obtain results of energy dispersions of armchair and zigzag.

$$E_q^a(k) = \pm t \sqrt{1 \pm 4 \cos \frac{q\pi}{n} \cos \frac{ka}{2} + 4 \cos^2 \frac{ka}{2}}, \quad (-\pi < ka < \pi) \quad \text{for armchair} \quad (2.38)$$

$$E_q^z(k) = \pm t \sqrt{1 \pm 4 \cos \frac{\sqrt{3}ka}{2} \cos \frac{q\pi}{n} + 4 \cos^2 \frac{q\pi}{n}}, \quad \left(-\frac{\pi}{\sqrt{3}} < ka < \frac{\pi}{\sqrt{3}}\right) \quad \text{for zigzag} \quad (2.39)$$

Fig.2.13 represents the results of examples with armchair cases,  $(n, m) = (5, 5)$  and  $(10, 10)$ . As can be seen, shapes of the energy band structure are symmetric. DOS is also shown in the same panel at the right side. Transfer matrix value  $t$  is applied 2.9 eV which is same as Kataura plot. From this calculation, we can obtain transition energy  $E_{11}$  for  $(5, 5)$  is 4.498 eV and for  $(10, 10)$  is 1.848 eV. DOS readily shows that armchair is metallic as valence band and conduction band are connected: it is also observed in energy band structure. Furthermore, the chiral number is larger, there are more sub small energy bands observed when we compare  $(5, 5)$  and  $(10, 10)$ . In case of armchair, the number of energy band is  $2n$ . For example, chirality  $(5, 5)$  has 10 energy bands in the valence band and conduction band. However, we cannot see 10 energy bands in the energy band structure because energy band structure has degeneracy. So, for the  $(5, 5)$  case, there are 6 energy bands, which means there are 4 degenerate energy bands.

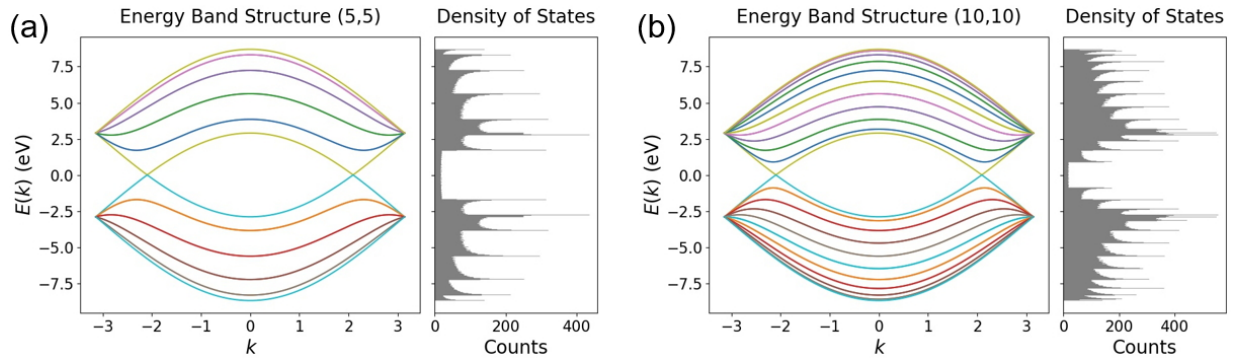


Figure 2.13: Energy dispersion diagrams for armchair cases. (a) Energy dispersion for  $(5, 5)$ . (b) Energy dispersion for  $(10, 10)$ .

Fig.2.14 shows zigzag semiconducting SWNTs,  $(n, m) = (5, 0)$  and  $(10, 0)$ . This diagram is also applied transfer matrix value  $t$  is 2.9 eV. There is no contact point between

conduction band and valence band as we expected it is semiconducting. These results are also observed in DOS. There are large number of energy sub bands in (10,0) than (5,0) similar manner like the armchair example. The transition energy  $E_{11}$  for (5,0) is 2.267 eV and for (10,0) is 1.011 eV.

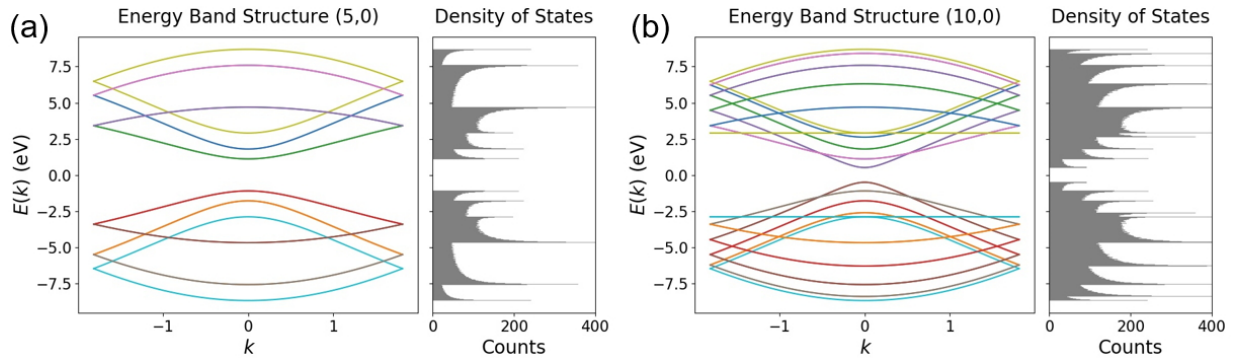


Figure 2.14: Energy dispersion diagrams for zigzag semiconducting cases. (a) Energy dispersion for (5,0). (b) Energy dispersion for (10,0).

From the metallic and semiconducting property relation, we can observe metallic case in zigzag. Chirality (6,0) is an example in Fig.2.15. As can be seen, there is connection between valence band and conduction band in DOS, also it is observed in energy band structure. The transition energy  $E_{11}$  for (6,0) is 2.476 eV, which is higher than semiconducting (5,0).

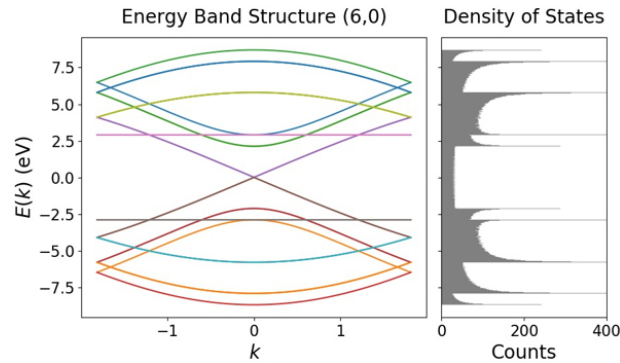


Figure 2.15: Energy dispersion diagrams for zigzag metallic case.

### Non-Symmetry Case: General Chiral Cases

Using Eq.(2.33), we can obtain general form of energy band structure. Chirality (6,5) and (7,6) are examples. Transfer matrix values are different for matching with experimental results [90]. For the (6,5) case,  $t$  is 3.2 eV and for the (7,6) case,  $t$  is 3.2 eV. Energy diagram and DOS are shown in Fig.2.16.

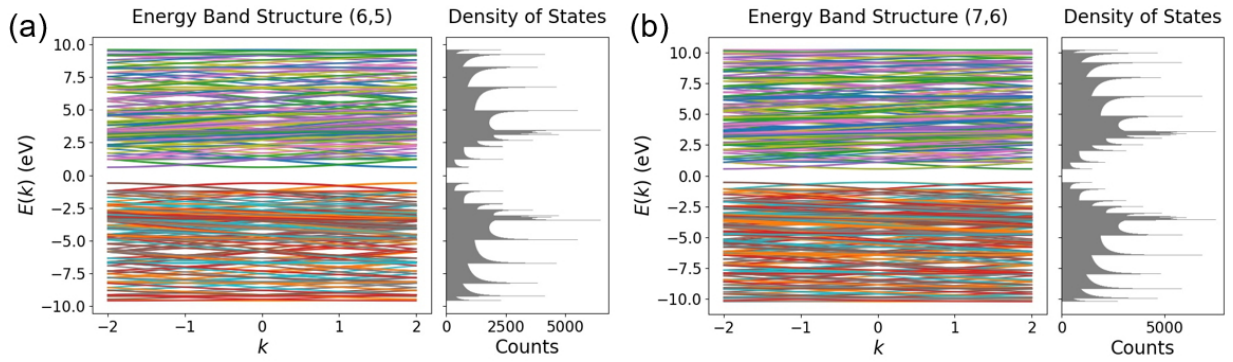


Figure 2.16: Energy dispersion diagrams for (6,5) and (7,6).

## Chapter 3

# Preparation of Sorted Carbon Nanotubes

MWNTs were first discovered accidentally Sumio Iijima in 1991 who introduced to make  $C_{60}$  by arc discharge method for  $C_{60}$ . Two years later, he found SWNT in a similar manner[74]. After Iijima's discovery discovered method of CNT fabrication, there are five different systematic synthesis methods developed: arc discharge (ADC), laser ablation (LA), sono-chemical or hydro-thermal, electrolysis, and CVD. Among them, the CVD method is commonly used and various sub-CVD methods are established; cobalt and molybdenum catalysts and CO gases (CoMoCAT) and high pressure carbon monoxide (HiPCO) are representative methods in the CVD growth. Diameter distributions of CNTs varies depending on the synthesis methods. During synthesis of CNTs specifically for SWNTs, chirality is not controlled factor so that there would be made mixture of SWNTs. Therefore, people have been working on sorting SWNTs in order to obtain pure semiconducting or metallic SWNTs or even single chirality for electrical and optical devices.

Section 3.1 summarizes these synthesis methods to generates raw CNT materials, followed by several purification methods in section 3.2. In particular, we attempt a cost-effective ATPE as our sorting choice, whose details are described in section 3.3 and optical chracterization results in section 3.4.

## 3.1 Methods of Carbon Nanotube Synthesis

### 3.1.1 Arc Discharge (ADC)

An ADC is the method of emergence of CNT introduced by Sumio Iijima [42, 43]. There are two carbon electrodes in the center of chamber and high currents, 200 A for Iijima, are applying to grow CNT on negative carbon electrode. Iijima filled the chamber with methane and argon adding the iron as catalysts on the electrode, whereas Journet *et al.* [53] and Bethune *et al.* [11] with helium and mixture of iron (Fe), nickel (Ni), and cobalt (Co). With this method, SWNTs are synthesized in the 0.7-to 1.65 nm diameter range. A schematic of the ADC chamber is shown in Fig.3.1 [20]. There are graphite electrodes, small carbon fragments are generated by high current in anode and deposited forming the CNT shape on the cathode in parallel. Inert gas becomes plasma in high temperature, > 1500°C, and low pressure, 50 - 700 mbar, affects the formation of CNTs with types of inert gases, temperature in the chamber, current, and catalysts. Specifically, the type of CNTs are determined by existence of the catalysts: SWNT with catalysts or MWNT without catalysts.

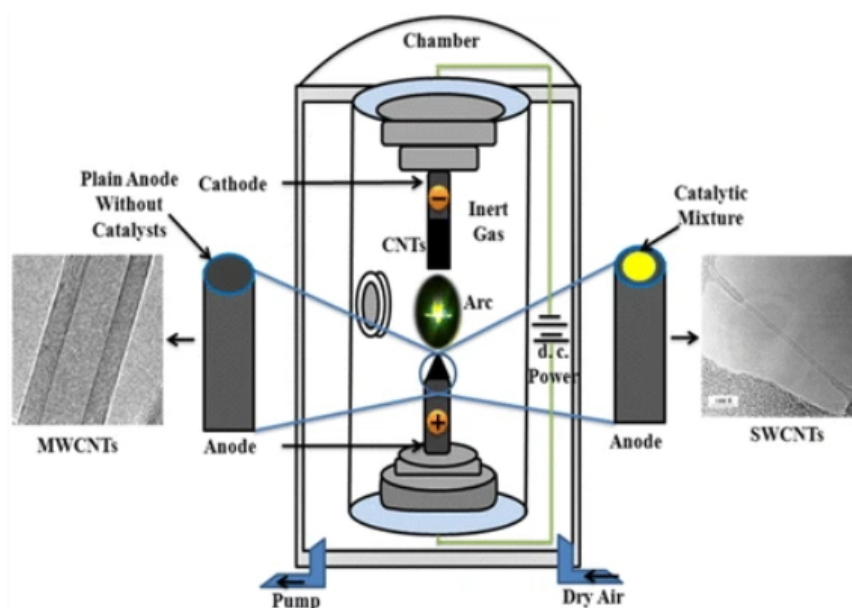


Figure 3.1: Drawing of arc discharge synthesis method. (Reprinted with permission from reference [20].)

### 3.1.2 Laser Ablation (LA)

LA method is another oldest one to synthesize CNTs. A main different step in the laser from the ADC is that laser directly shines the graphite target which contains catalysts and is surrounded by an inert gas like helium (He). Guo et al. demonstrated the LA method in 1995 and pursued since this method is better than ADC in terms of higher yields, better control graphite electrodes, and sustainable operation due to the direct laser exposure on the target [34]. A principle of process is explained in Fig.3.2 [20]. A laser strikes target passing through the inner gas at 1200 °C, evaporating graphite assisted by inert gas and catalysts, and CNTs are formed on the water-cooled collector. In this case, MWNTs or SWNTs are synthesized depending on the catalysts on the graphite similar to the ADC method.

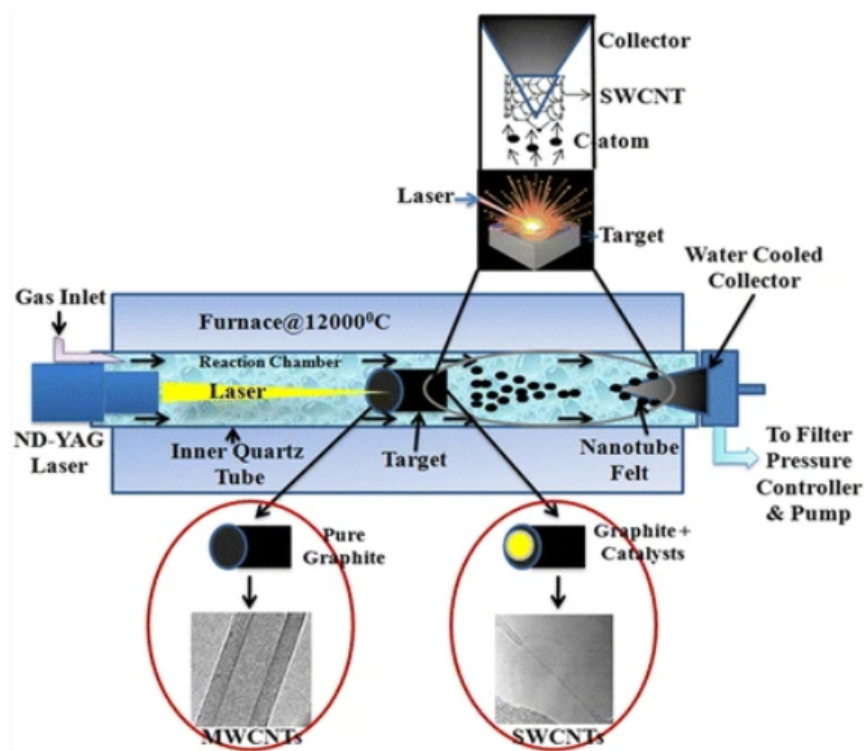


Figure 3.2: Drawing of laser ablation synthesis method. (Reprinted with permission from reference [20].)

Despite these two methods, the ADC and the LA, are the oldest and common ways

from the early stage of CNT synthesis, there are several disadvantages. First, both are required high energy to generate arc or laser so that they have scalability limitation as well as inefficient input energy consumption. Second drawback is that both have evaporation steps which is not sufficient in scalability as well. Last is that they suffer from many contamination such as catalysts not desirable being generated on CNTs. That is why the produced CNTs in these methods needs purification step, another cost expected[74]. Overcoming these three limitation in both old methods, CVD method is common in these days.

### 3.1.3 Chemical Vapour Deposition (CVD)

The CVD technique is a common and popular synthesis of CNTs after arc discharge and laser ablation methods by increasing purity in a relatively well-controlled manner. Unlike previous two methods which physically impact by high voltage or laser, the CVD method forms CNTs on the catalysts decomposing hydrocarbon gas. Li *et al.* demonstrated the CVD methodology in 1996 with acetylene for hydrocarbon gas and iron nanoparticles as a catalyst at 700 °C[62]. CNTs grow directly on the catalysts which are laid on substrates in a furnace as shown in Fig.3.3 [88]. These processes can be performed synthesis continuously as long as hydrocarbon gases are supplied and enough substrates are prepared in the furnace in atmospheric pressure. Through these advantages, CVD can be suitable for mass production with maximizing yield and minimizing cost. However, precise control of catalysts size and temperature of substrates are required because diameter of CNT is related to the size of nanoparticles. There are other derivatives of CVD, such as hot filament, water assisted, oxygen assisted, radio-frequency, thermal, and plasma enhanced. In particular, the plasma enhanced chemical vapor deposition (PECVD) is able to generate vertically aligned CNTs without porous substrates [74].

### 3.1.4 Other Chemical methods : High Pressure Carbon Monoxide® (HiPCO) and Cobalt-Molybdenum Catalyst®(CoMoCAT)

HiPCO and CoMoCAT methodologies are similar CVD methods but advanced synthesis methods for large scale productions. Nikolaev *et al.* claims that SWNTs are synthesized in a gas-phase catalytic process [69]. This process is similar to a standard CVD ; SWNTs are formed on substrates in a furnace. The gas-phase process is unique in

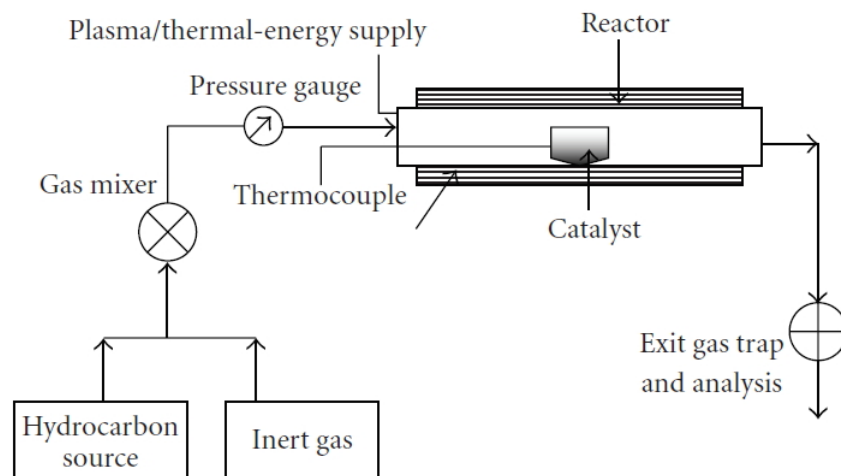


Figure 3.3: Schematic of chemical vapor deposition synthesis method. (Reprinted with permission from reference [88].)

this methodology when applying **carbon monoxide (CO)** for carbon supply and **iron pentacarbonyl (Fe(CO)<sub>5</sub>)** as a catalyst precursor at high pressure, 1 - 10 atmospheric pressure, and high temperature, 800 - 1200°C[69]. Bronikowski *et al.* optimizes the growth parameters of the **HiPCO** process such as pressure, temperature, and they attain the **SWNTs** 10 gram per day. The spray shape in a scheme of the **HiPCO** equipment in Fig.3.4 seems to be a main apparatus in order to generate **SWNTs** [14].

The **CoMoCAT** process is known as high selectivity, reducing the variation of the **SWNT** diameters which means the number of chirality is decreased. The secret of this process is the combination of **Co** and **molybdenum (Mo)**, and the power of those two-element effect is discovered by Resasco *et al.* [76] and Fig.3.5 presents how the **Co** and **Mo** work during growth. There is no reaction existence of each element on a substrate. From the **Co** and **Mo** interaction makes synthesis process.

### 3.1.5 Summary of Synthesis Methods

Above methodologies can be classified by either a physical process or a chemical process. Physical processes are developed in the early stage of the **CNT** synthesis and they are inefficient in all of the comparison aspects. On the other hand, chemical processes are controllable economical Table 3.1. Table 3.1 summarizes three representative **CNT** synthesis methods and compares them in 8 distinct aspects. All of them possess pros

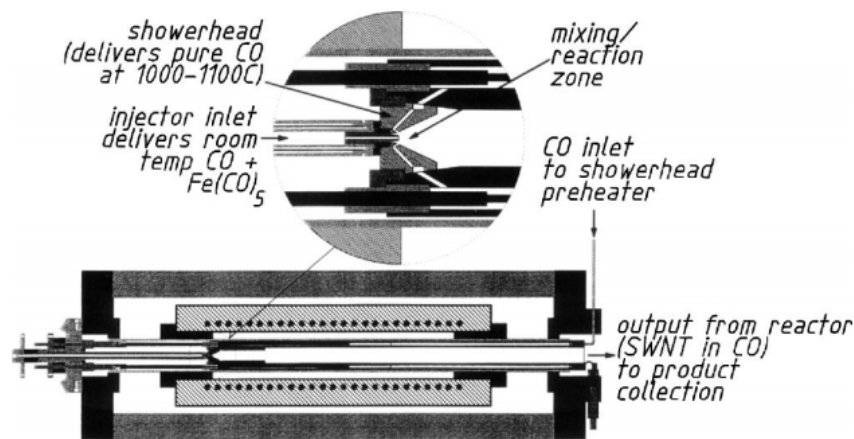


Figure 3.4: Drawing of High Pressure Carbon Monoxide synthesis method. (Reprinted with permission from reference [14]. Copyright 2001 America Vacuum Society.)

and cons and at present CVD-grown CNTs are dominantly available from commercial vendors. The prices are still very high, which is a big challenge for ubiquitous use in future applications.

### 3.2 Sorting Methods

As we discussed in chapter 2, SWNTs exhibit metallic or semiconducting properties, furthermore although they are made of same carbons, they have various energy band gaps in semiconducting cases. These properties are related to the chirality which is represented as  $(n, m)$ , at the moment we can not obtain or synthesize certain or specified chirality by various methods which we discussed in chapter 3. There are quantitative results as our wish we can figure out easily in Fig.3.6 which demonstrate large diameter variation, corresponding chirality variation for synthetic methods. A big challenge produced in CNTs, for functional application is sorting problem, even though it is believed as promising material in numerous fields, we cannot select a pure chirality so as to use special energy band gap or even combination of pure semiconducting or metallic property of CNTs. For this reason, researchers who are inspired by superb material, CNTs, have been exploring lots of sorting methods since it was become widely known by Sumio Iijima. It has been more than 15 years, and several methods are well explained chronologically in a review paper [95].

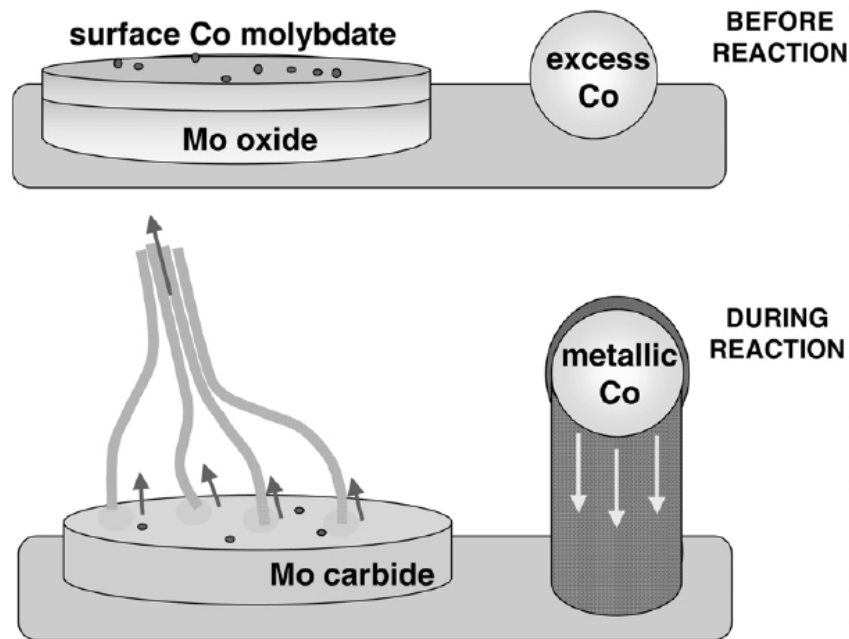


Figure 3.5: Sketches of a CoMoCAT synthesis method. (Reprinted with permission from reference [20].)

### 3.2.1 Ion Exchange Chromatography

A first attempt of the CNT sorting was done by ion exchange chromatography for DNA-wrapped SWNTs [96]. The results were not attractive compared to those from modern techniques, however the early attempt gives us possibilities and clues of strategic of sorting methods of SWNTs. This approach is explained two different manner, atomic structure-based and electronic structure-based. Basically, SWNTs are wrapped by DNA, namely, SWNTS are physically covered with biology background knowledge technique which is atomic structure-based sorting manner, whereas ion exchange chromatography is for electronic structure-based sorting manner in 2003.

### 3.2.2 Density Gradient Ultracentrifugation (DGU)

A next approach is conceptually based on the density of SWNTs because of different of chiralities. Elaborately, large-diameter SWNTs are heavier than small diameter ones, thus separation is done by ultracentrifugation which arranges SWNTs by the or-

Process / Property	Arc-discharge	Laser Ablation	Chemical Vapor Deposition
Raw materials availability	Difficult	Difficult	Easy, abundantly available
Energy requirement	High	High	Moderate
Process control	Difficult	Difficult	Easy, can be automated
Reactor design	Difficult	Difficult	Easy and can be designed as large scale process
Production rate	Low	Low	High (HiPCO, CoMoCAT)
Purity of product	High	High	High
Yield of process	Moderate (70 %)	High (80 - 85 %)	High (95 - 99 %)
Post treatments requirements	Require refining	Require refining	No extensive refining required
Process nature	Batch type	Batch type	Continuous
Per unit cost	High	High	Low

Table 3.1: Table of comparison of synthesis methods of CNTs [74]

der of densities. This is named as **density gradient ultracentrifugation (DGU)** which was starting in 2005 [5]. This also used DNA-wrapped **SWNTs** in dispersion and separating them and density gradients of iodixanol leveling density of **SWNTs**. Before doing **DGU** process, Wenseleers *et al.* attempted to use surfactants, **sodium cholate (SC)**, **sodium deoxycholate (DOC)**, etc. in order to disperse **SWNTs** in water [91]. This attempt was borrowed into **SWNT** sorting and has been influenced not only **DGU** but other methods such as selective extraction, gel chromatography, **ATPE**.

### 3.2.3 Selective Extraction

Another sorting attempt is selective extraction which is first demonstrated in 2007. **SWNTs** produced by **HiPCO** and **CoMoCAT** are soluble in several different polymers, poly[9,9-dioctylfluorenyl-2,7-diyl], poly[9,9-dihexylfluorenyl-2,7-diyl], poly[(9,9-dioctylfluorenyl-2,7-diyl)-co-(1,4-phenylene)], and poly[(9,9-dioctylfluorenyl-2,7-diyl)-alt-co-(1,4-benzo-2,10,3-thiadiazole)], referred as PFO, PFH, PFO-P, and PFO-BT, respectively. Interesting results showed different absorbance and photoluminescence map associ-

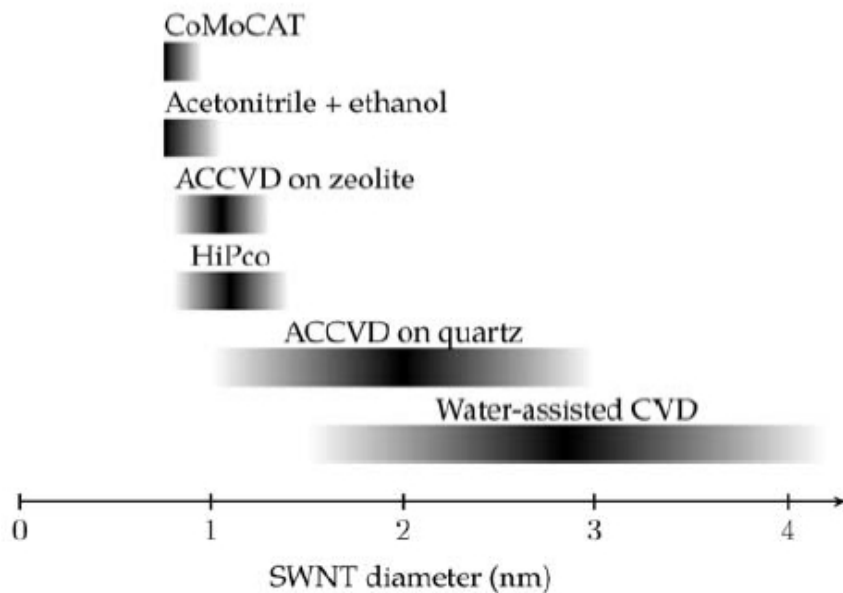


Figure 3.6: Large diameter range in each SWNT synthesis method. (Reprinted with permission from reference [24]. Copyright 2013 Woodhead Publishing Limited..)

ated with specific polymer solutions, which mean that solution contains different chirality and selectively sorted SWNTs in not so big different chemical structured polymers [70]. This study demonstrated a possibility that different solvents selectively dissolve SWNTs, but it is impractical because we are not able to use non-dissolved SWNTs. Gel chromatography sorting method was executed for SWNTs in 2009 [82], which is a standard method in biotechnology. There are four different specific implementation ways with agarose gel, which is polysaccharide and is made from red seaweed resulting in metallic and semiconducting separation; freezing SWNTs in gel and separating by thawing solution of metallic, centrifugating SWNTs in gel, and mixing SWNTs in elution buffer or surfactant with gel and separating. Tanaka *et al.* also mentioned it can be scale up. This method is regarded as a kind of selective extraction method but it would be a different branch of separation method due to the first demonstration of sequential separation to my best knowledge.

The last sorting method is ATPE. This method will be discussed in detail at chapter 4 as it is our choice of the SWNT separation which we have sorted SWNTs.

## Chapter 4

# Aqueous Two-Phase Extraction (ATPE)

An [ATPE](#) method is also called as aqueous two-phase system (ATPS), and has been also developed in the fields of biotechnology from a long time ago with a long history. A two-phase system was found with immiscible aqueous gelatin in 1896 by Martinus Willem Beijerinck by accident [32]. Current [ATPE](#) form of a polymer-polymer immiscible systems was discovered by Per-Åke Albertsson using [polyethylene glycol \(PEG\)](#) and [dextran \(DX\)](#) in 1960 [56]. After his discovery, [ATPE](#) has been improved and applied in various aspects: purification and separation of protein, enzymes, monoclonal antibodies, DNA, virus, drug residues in food and water, etc. [1]. An [ATPE](#) in [SWNTs](#) was first attempted in 2013 by a group of researchers in [National Institute of Standards and Technology \(NIST\)](#) [58]. This [ATPE](#) approach contains some features of previous four different sorting methods, DNA-warpped [SWNTs](#), [DGU](#), selective extraction, and gel chromatography because [SWNTs](#) are wrapped by surfactants selectively and separated due to the density and hydrophobicity differences during [ATPE](#) process. However, [ATPE](#) has homogeneous top and bottom phases such that consecutive separation steps can be done sequentially, and it gives reproducible results with varying the surfactant concentrations. Furthermore, it is relatively low-cost compared to aforementioned methods above and it possesses a great potential to scale up in large quantities. In terms of separation results, [ATPE](#) isolates [SWNTs](#) not only by diameters but also metallic and semiconducting nature via redox process [33].

## 4.1 Principle

Two key factors of successful ATPE sorting are ① two-phase polymer-polymer separation, ② surfactant concentration control. Summary of ATPE sorting process exploiting SWNTs is able to simplify as below.

- Polymers : PEG and DX - must be care of phase diagram to sustain two clear phases
- Surfactants : concentration is determined by diameter of SWNTs
  1. Diameter separation : sodium dodecyl sulfate (SDS) and DOC
  2. Metallic & semiconducting separation : SDS and SC with sodium hypochlorite (NaClO)

### 4.1.1 Polymers and Phase Diagram

ATPE process separates SWNTs by diameters or metallic and semiconducting properties arising from the interplay of polymer and surfactants. As the name of the process indicates, solution is divided to two-phases by two mixed immiscible polymers as we discussed above, PEG and DX, as common and popular choice in biology. Since the molecular masses of polymers play a role in stabilizing bi-phase, similar to DGU, we use 6 kdalton (Da) of PEG and 70 kDa DX so that heavier DX goes down. And depending on the mass-ratio, the solution can exhibit a single phase which should be avoided. Hence, the phase diagram of PEG and DX is the one of the crucial prerequisite tasks for SWNT separation with ATPE because we cannot separate without biphasic condition. A binodal curve in Fig.4.1(a) is the boundary of biphasic or monophasic region for us to establish phase diagram PEG and DX, which identifies monophasic and biphasic..

There is no clear explanation how these phases form so far. One commonly accepted model is by Albertsson's model. A partition coefficient  $K$  is expressed by five different factors,

$$\ln K = \ln K^0 + \ln K_{\text{elec}} + \ln K_{\text{hfob}} + \ln K_{\text{affinity}} + \ln K_{\text{size}} + \ln K_{\text{conf}} \quad (4.1)$$

where elec, hfob, affinity, size, and conf are electrochemical, hydrophobic partitioning, affinity partitioning, molecular size or surface area of molecules, and conformation, respectively.  $K^0$  is all other factors such as environment [1]. This equation indicates

these five factors control ATPE process. Here in this diagram Fig.4.1(a), phases are determined by top and bottom concentrations; in order to make stable biphasic solutions, we should prepare PEG and DX above certain concentrations. The line drawn by T and B which are on the binodal curve is a tie line, namely; combinations on tie line have all equilibrium composition for top and bottom phase. At point C which is a critical point, the top and bottom phases have the same volume theoretically.

Fagan *et al.* demonstrated the phase diagram with and without surfactants in Fig.4.1(b), SDS and DOC, in PEG and DX. The shape of the binodal curves is not exactly symmetric as the general binodal curve in Fig.4.1(a) because of molecular weight differences [7], but it shows the surfactant effect in that surfactants move binodal curve to a upper side [25].

We also established our own phase diagram [21] so as to confirm our ATPE results with our own recipes and to figure out the surfactants concentration effects. The results are shown in Fig.4.1(c). Although we did not obtain the nice shape of the binodal curve, the results clearly conclude that a phase diagram tends to push upward as the concentrations of the surfactants increase. We may not draw the binodal curve in our data because it is difficult to find out the boundary of biphasic and monophasic regions. The key point is that we successfully identify the biphasic region. With these points, we also fit to the data in three aqueous two-phase system (ATPS)-specific coefficients [7]. With a theoretical binodal equation is expressed as below,

$$[PEG] = C_1 e^{C_2[DX]^{0.5} + C_3[DX]^3}, \quad (4.2)$$

where [PEG] and [DX] correspond the concentrations of polymers and  $C_i$  are fitting parameters. Without perceiving the importance of understanding the phase diagram, we did not recognize the reason why the monophasic status came out during sorting process, especially sorting with purple colored SWNT solution when we used higher surfactant concentrations. In addition, we also encountered murky solution from time to time during ATPE, and we attribute the cause to the fact that solutions are near the binodal line, where two polymers are partly mixed so that we did not obtain ideally well-separated SWNT solutions. In conclusion, finding, understanding, and reproducing a good phase diagram is a starting point for successful ATPE outcomes.

### Separation with Surfactants: Partition coefficient, Hydrophobicity, and Structure

Given a phase diagram of two polymers, a next step is making proper concentration combination of surfactants for diameters. We already know that polymers form two

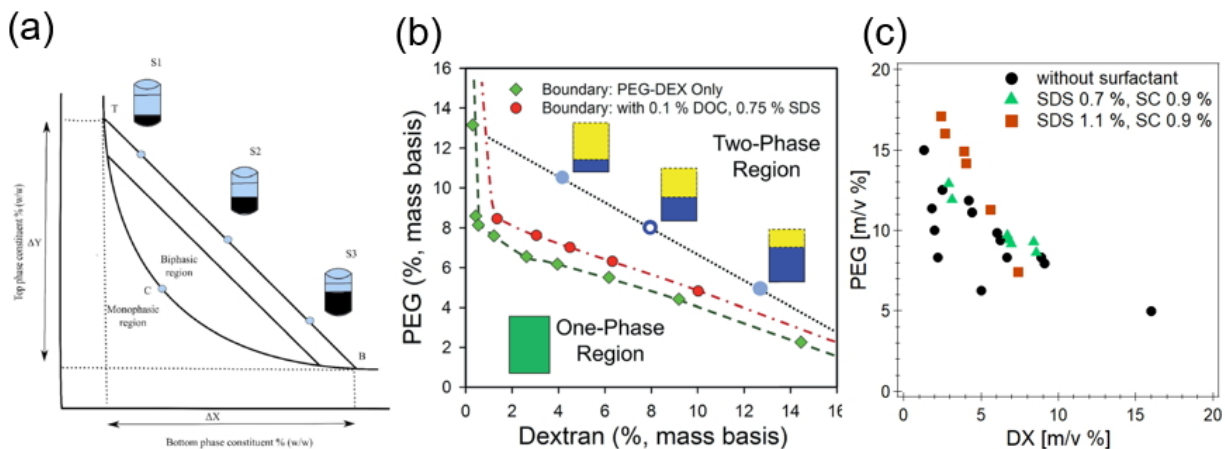


Figure 4.1: Phase diagrams with two-different polymers. (a) General phase diagram. (Reprinted with permission from reference [7]. Copyright 2016 American Chemical Society.) (b) Phase diagram with and without surfactant in PEG 6 kDa and DX 70 kDa. (Reprinted with permission from reference [25].) (c) Phase diagram with and without surfactant in PEG 6 kDa and DX 70 kDa done by ourselves [21].

phases but it is hard to explain how which the *SWNTs* go to top or bottom phases in those polymers. One background theory expresses partition coefficients described as below [58].

$$K_i = \frac{C_{Top,i}}{C_{Bottom,i}} = \exp\left(-\frac{\mu_{Top,i}^0 - \mu_{Bottom,i}^0}{k_b T}\right), \quad (4.3)$$

where  $\mu_{Top,i}^0$  and  $\mu_{Bottom,i}^0$  are the standard chemical potentials in the top and bottom phases for a surfactant  $i$ ,  $k_b$  is Boltzmann constant, and  $T$  is absolute temperature. With Eq.(4.3) and Fig.4.2, separation is explained by partition coefficients  $K_i$  and the values of  $K_i$  vary with surfactants.

In a diameter separation, for example in Fig.4.2(a), where *DOC* concentrations fixed, and *SDS* concentration is selected depending on the separation boundary, which is determined by an operator who wants to extract a certain chirality which is related to the diameter. That concentration combination of *SDS* and *DOC* determines coefficient  $K_i$  based on chemical potential differences in the equation. Diameter separation is done with *DOC*, on the other hand, metallic and semiconducting separation is done with *SC* in Fig.4.2(b). This is a similar concept that varying the concentration of *SDS* but different pairing surfactant *SC* with the fixed *SC* concentration. One more hidden fac-

tor is  $\text{NaClO}$  which is an oxidant agent to facilitate for metallic and semiconducting separation. Let me discuss the role of  $\text{NaClO}$  in the next redox section.

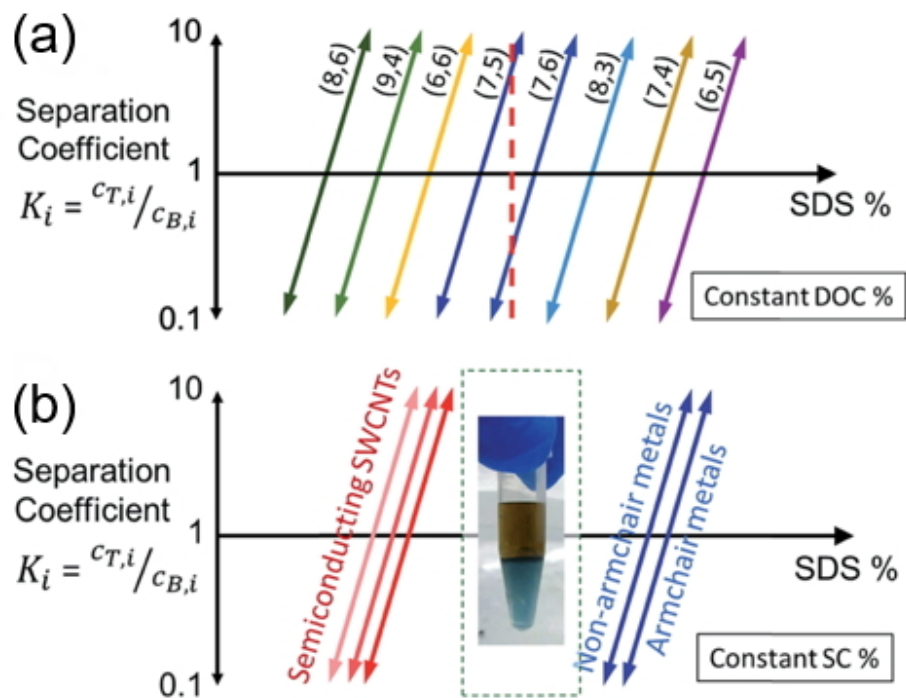


Figure 4.2: Separation coefficient diagrams. (a) Separation coefficient with varied SDS concentration at fixed DOC for diameter separation. (Reprinted with permission from reference [25].) (b) Separation coefficient with varied SDS concentration at fixed SC for metallic and semiconducting separation. (Reprinted with permission from reference [25].)

Although the separation of  $\text{SWNTs}$  with surfactants is explained with partition coefficients, there are still puzzles how different surfactants are selectively covering  $\text{SWNTs}$  and placing in different phase; empirically,  $\text{SDS}$  is in the top phase  $\text{PEG}$ , and  $\text{DOC}$  for diameter separation or  $\text{SC}$  for metallic or semiconducting separation are in the bottom phase  $\text{DX}$ . This puzzle may be solved by hydrophobicity and structure of surfactants.

There is hydrophobicity difference in two polymers,  $\text{PEG}$  and  $\text{DX}$ . Hydrophobicity is closely related to the concentration of the polymers. Therefore, when these two polymers form a biphasic system, two polymers show hydrophobicity differences and  $\text{PEG}$  is more hydrophobic than  $\text{DX}$  [94]. In the presence of surfactants, specifically, among

SDS, DOC, and SC, SDS shows more hydrophobic property than DOC and SC [81]. From these inherent differences in polymers and surfactants, there exist distinct affinities between polymers and surfactants; PEG tends to pair with SDS and DX tends to pair with DOC and SDS. Therefore, SDS goes up to the PEG phase, whereas DOC and SC goes down to the DX phase. Then, the last puzzle is left the reason how surfactants selectively adhere on SWNTs.

As can be seen in Fig.4.3, there are two chemical structures of SDS and DOC. SDS has a long chain while DOC does not have a long chain. From this structural difference, wrapping SWNTs conditions are different; the long chain of SDS is relatively easy to cover larger-diameter SWNTs and DOC is for smaller-diameter SWNTs.

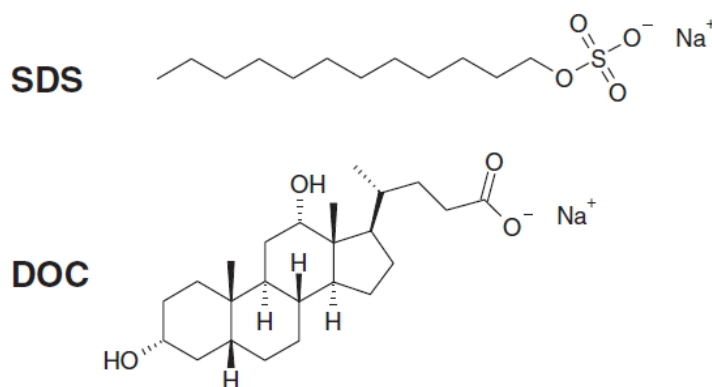


Figure 4.3: Chemical structure of SDS and DOC. (Reprinted with permission from reference [91]. Copyright 2004 WILEY-VCH Verlag GmbH & Co. KGaA, Weinheim.)

### Redox for Metallic and Semiconducting Separation

Reduction-oxidation reaction, redox in short, is a typical chemical reaction resulting from the electron transfer between molecules. Redox chemistry also adds a novel method to enhance the efficiency of sorting metallic and semiconducting SWNTs. Fig.4.4 captures the results of redox sorting with five distinct conditions: fully reduced, semi-reduced, ambient, semi-oxidized, and fully oxidized. As can be seen for fully reduced, ambient, and fully oxidized cases all SWNTs go to one phase, in other words, the sorting fails. However, for semi-reduced and semi-oxidized cases we observe two different colors in the top and bottom phases where the sortings work. Note that the color configurations are opposite between semi-reduced and semi-oxidized. This means that

metallic is in top phase and semiconducting is in bottom phase for semi-reduced and vice versa for semi-oxidized.

The principle of these phenomena is accounted for band gap which we discussed in chapter 2. The oxidation process carries out by adding various oxygen or losing electrons. If we assume there are two different band gap SWNTs, one has larger band gap than the other, the smaller band gap SWNT is easy to lose electron and be oxidized. According to this principle, metallic SWNTs are most SWNT to be oxidized since they have no band gap, readily losing electron. Smaller band gap semiconducting SWNTs are the next easiest to be oxidized, and larger band gap semiconducting SWNTs are hardest. Oxidized SWNTs are wrapped by SC and go down to the bottom phase of DX. Some explanation of NaClO is one of standard oxidation agents and even small amount of NaClO signifies the separation. For example, typical amount of adding oxidation agent, NaClO is 6 mL - 8 mL for 1 mL of total amount of solution; here concentration of NaClO is 1/100<sup>th</sup> of original solution purchased at Sigma-Aldrich, 425044.

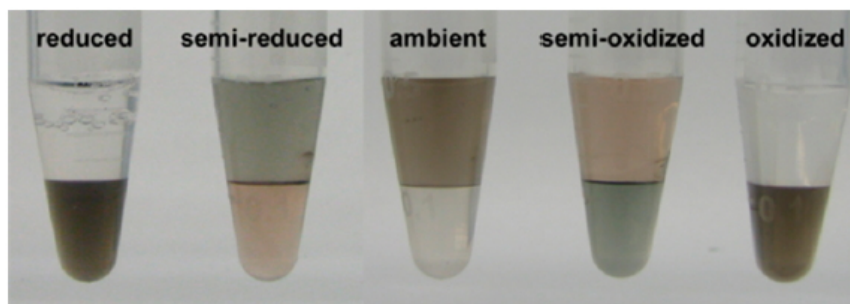


Figure 4.4: Separation results in reduced or oxidized solutions. (Reprinted with permission from reference [33]. Copyright 2015 American Chemical Society.)

### Brief Scheme of the Aqueous Two-Phase Extraction

If we put all of these together, forming the biphasic system of polymers (PEG and DX), and coming the interplay of hydrophobicity of polymers (PEG and DX) and surfactants (SDS, DOC, and SC), and chemical structure of surfactants (SDS, DOC, and SC), we can imagine how SWNTs are wrapped by surfactants and are separated in the ATPE process. Due to the diameter differences for each chirality SWNTs, there are curvature differences. These curvatures are related to chemical structure of surfactants. According to the proper concentration of SDS and DOC which are correlated with diameters of SWNTs, there are two groups: relatively larger diameter group wrapped

SDS and smaller diameter group with DOC. And then two groups are moving along the hydrophobicity so that in the end, larger diameter SWNTs go to the top PEG phase and smaller diameter ones go the bottom DX phase in concentration dependent ATPE Fig.4.5. In addition, density of smaller-diameter of SWNTs which is wrapped by DOC is higher than larger diameter SWNTs, this is another reason going to the bottom phase.

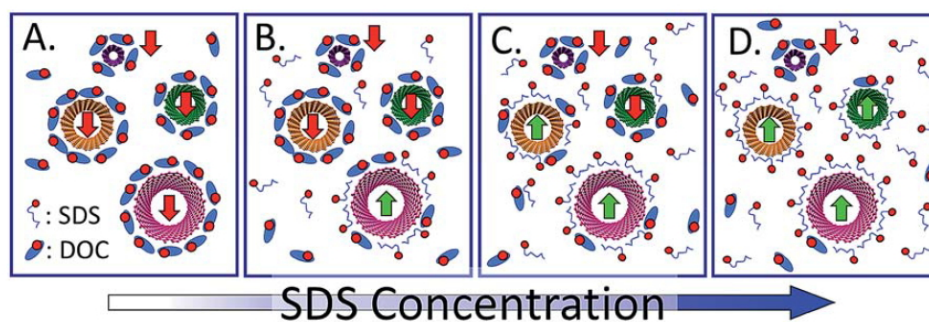


Figure 4.5: A schematic of separation of SWNTs in biphasic system. (Reprinted with permission from reference [25].)

## 4.2 Process

ATPE process consists of three steps: pre-process, main process, and post-process. Pre-process consists of preparing solutions of SWNT and other stocks for the main step. First, we need to disperse SWNTs in water with surfactants and purify the solutions for removing impurities. Stocks in bulk of solutions essential for ATPE are polymers and surfactants doing steps smoothly and quickly because we do not make certain concentration of solutions each time. Once pre-process are done, we can move the main process. This main process is ATPE itself, tracking concentration of solution is a main point. And executing many times delivers high purity SWNT solution. The last step is measurement parts which confirms contents of solutions. UV-vis and Raman measurements are able to show chirality in solution. Then, removing polymers and reduce concentration of surfactants so as to use sorted SWNTs. Below steps are simplified process of ATPE.

1. Pre-process: Make SWNT solutions and prepare stocks

2. Main process: Proceed [ATPE](#) repeatably
3. Post-process : Characterize sorted solutions for chirality classification and do polymer exchange

#### 4.2.1 Schemaitc of ATPE Process and Result with Surfactant Concentration

Through the understanding of the [ATPE](#) separation principle, we can obtain sorted [SWNTs](#) by repeating sequential [ATPE](#) steps in Fig.4.6. Because each [ATPE](#) results in two outputs top and bottom, which contain mixtures of [SWNTs](#) with several chiralities. Therefore, we need to repeat many steps in order to obtain high purity of a certain [SWNT](#). A crucial control parameter is varying the concentration of surfactants.

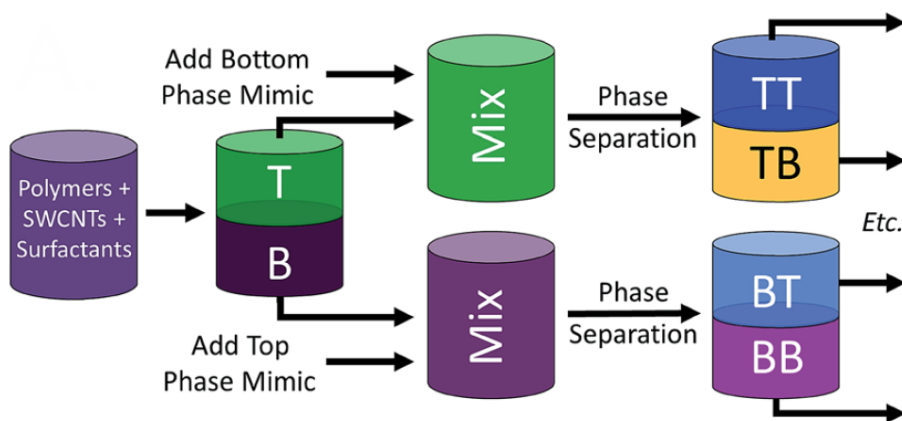


Figure 4.6: A schematic of ATPE process. (Reprinted with permission from reference [25].)

Fig.4.7 captures one of the [ATPE](#) results to isolate [SWNTs](#) of a specific chirality represented by [SWNT](#) diameter in terms of the [SDS](#) concentration while the [DOC](#) concentration is fixed at 0.045 %. This result is extremely impressive because most of the chirality of [SWNTs](#) are on the green curve except several points, which demonstrates that controlling a ratio of surfactant concentrations determines a chirality of sorted [SWNTs](#). Combining this relation with aforementioned synthesis method, we can predict the range of diameter of [SWNTs](#) and design [ATPE](#) considering the concentration of surfactants.

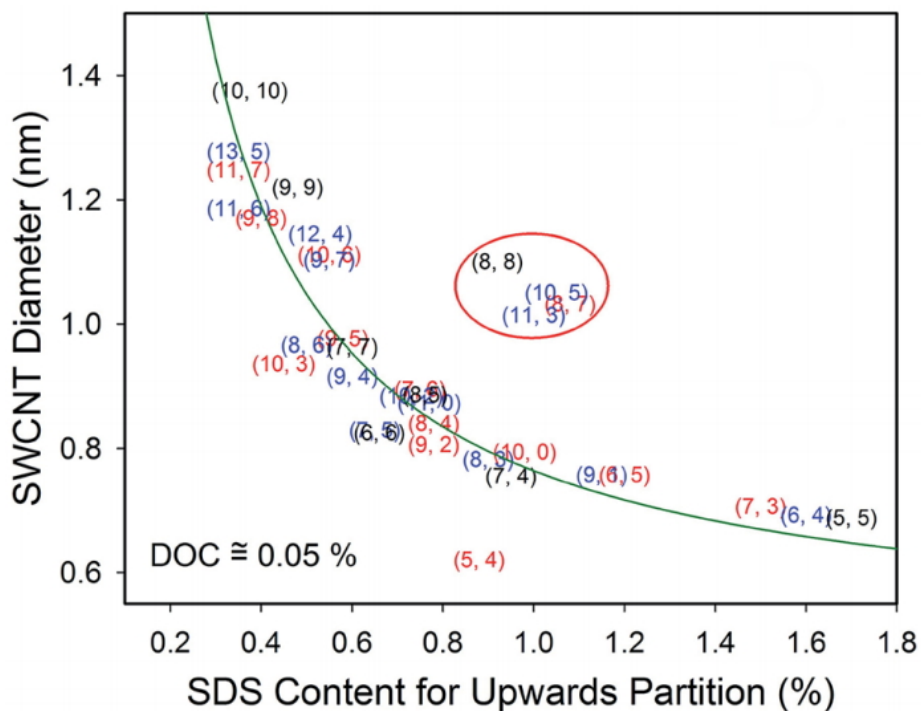


Figure 4.7: The relation between the concentration of SDS and the diameter of SWNTs at a fixed DOC 0.45 %. (Reprinted with permission from reference [25].)

#### 4.2.2 Pre-Process: Make SWNT Solution and Prepare Stocks

There are four sub-steps the pre-process, prepares essential SWNT dispersions and necessary stocks during ATPE and it consists of 4-sub steps.

1. Dispersing SWNTs in surfactants

ATPE process works in solution-base. However, because CNTs are hydrophobic CNTs are not easily dispersed in water; therefore we need to make homogeneous solutions with the help of surfactants. There are two surfactants commonly used for dispersing CNTs; DOC is for SWNTs and SC is for MWNTs.

For dispersing SWNTs, we apply concentration of DOC is 1.6 % which is the optimal concentration for dispersion [12]. The concentration of CNTs is 1 mg/mL which is commonly used. Because CNTs are nano-particles which may be hazardous to human-beings through inhalation, we need to proceed the dispersion

process inside a glove box. In order to make 1 mg/mL CNT concentration, a surfactant mixed solution at a known weight is put in the glove box and CNTs are added.

## 2. Doing bath and tip sonications

Although surfactants are in Milli-Q water (MQW), CNTs are not dispersed in the surfactant solution because of highly attractive van der Waals force between CNTs. Therefore, external forces are needed to break aggregated CNT particles. Once CNTs are in surfactant solution, the first step is bath sonication for 10 minutes, initial dispersion followed by tip sonication for 2 hours.

We use a Q125 sonicator made by QSONICA in a 2-seconds-on and 1-second-off mode with 71 % amplitude. There are two probes depending on the amount of solution volume, the 1/8 inch diameter of a tip is used for 500  $\mu$ L - 15 mL and the 1/4 inch diameter of a tip is used for 10 mL - 50 mL. We can clearly observe well-dispersed CNT solutions after tip sonication.

## 3. Centrifuging to remove impurities

Our raw CNTs typically in powder form and are not 100 % pure, contains also 95 % of carbon junks such as amorphous carbon, and carbon soot. In addition, there are catalysts as well. For instance, SG65i which is purchased from Sigma-Aldrich, has 95 % of CNTs, that means 5 % of impurity exists. Ultra-centrifugation removes these impurities. There are two steps of ultra-centrifugation. The first step is at 20,000 rpm for 1 hour 45 minutes and the second step is at 60,000 rpm for 45 minutes in Optima XE-100 ultracentrifuge made by Beckman Coulter. This process is time consuming and has risks because high speed spinning may generate extremely big force even with tiny weight of particles. Therefore, we must be cautious balancing the solutions when loading samples in a ultra-centrifuge. We take 60 % - 80 % of supernatants for top partition which means pure solution in each step and rest of solution for bottom partition except pellets which are stuck at the bottom of tubes. These top and bottom solutions are used for ATPE process. Table 4.1 collects information of raw CNTs which we use for separation.

## 4. Preparing polymer and surfactant stocks

In the main process of ATPE, we need to make different surfactant concentrations in every step promptly. If we prepare larger volumes of stocks, this is an efficient process before starting main process. There are two polymers, three surfactants, and an oxidant. The concentration of solutions are recommended by Jeffrey

Product	Distributor	Product number	CNT Type	Synthetic method	Average diameter	Median length
SG65i	Sigma-Aldrich	773735	SWNT	CoMoCAT	0.78 nm	1 $\mu\text{m}$
SG76	Sigma-Aldrich	704121	SWNT	CoMoCAT	0.83 nm	1 $\mu\text{m}$
SWNT	Sigma-Aldrich	704113	SWNT	CoMoCAT	0.7 - 1.3 nm	1 $\mu\text{m}$
MWNT	Sigma-Aldrich	698849	SWNT	CVD	12 nm	10 $\mu\text{m}$
Purified SWNT	NanoIntegris		SWNT	HiPCO	0.8 - 1.2 nm	100 - 1 $\mu\text{m}$

Table 4.1: Information of carbon nanotubes which we used for ATPE [46, 47, 48, 45, 44]

A. Fagan [25]. Detail information is in Table 4.2. Concentration unit of polymers is mass per mass [% m/m] and surfactants is mass per volume [% m/v]. (For instance, 1 % m/v = 1 g/10mL)

Product	Maker	Solution				Remark
		Target concentration	Target amount	Polymer or surfactant	MQW	
PEG 6k	Alfa Aesar	25 %	402 mL	134 g	402 mL	
DX 70k	TCI	20 %	400 mL	100 g	400 mL	
SDS	Sigma-Aldrich	4.5 %	400 mL	18 g	400 mL	OibXtra > 99 %
DOC	Sigma-Aldrich	4.0 %	400 mL	16 g	400 mL	OibXtra > 98 %
SC	Sigma-Aldrich	4.5 %	400 mL	18 g	400 mL	OibXtra > 99 %
NaClO	Sigma-Aldrich	1/100 <sup>th</sup>	100 mL	1 mL	99 mL	10 - 15 % Chlorine

Table 4.2: Table of information of stocks for ATPE [25].

### 4.2.3 Main Process: Proceed ATPE Repeatably

The main process can be divided into two different steps.

1. Preparation of SWNT Solutions

Basically, overall ATPE progress is undergoing at DOC concentration, 0.04 %. Because the DOC concentration in pre-process is set as 1.6 %, we need to lower the DOC concentration before starting the ATPE. Two different sorting options are existent, one is for diameter separation at the beginning after the preparation step and the other is for metallic and semiconducting separation. For diameter separation keeping the DOC concentration as 0.04 % is not a big problem because diameter separation needs SDS and DOC combination. On the other hand, for metallic and semiconducting separation, DOC concentration should be lower than 0.02 %, that is the reason why those two recipes are different. Another interesting point is the choice of sorting methods relies on the raw materials. Specifically, SG65i and purified SWNT by Nanointegris start with diameter separation and SG76 and SWNT by Sigma-Aldrich with metallic and semiconducting separation. Here are the condition of preparation steps in Table 4.3.

Material	Preparation #1 [%]				Preparation #2 [%]			
	PEG	DX	DOC	SC	PEG	DX	DOC	SC
SG65i & SWNT by NI*	9 - 10	5 - 6	0.40 - 0.45		9 - 10	5 - 6	0.2 - 0.225	
SG76 & SWNT by SA*	9 - 10	5 - 6	0.35 - 0.40		9 - 10	5 - 6	<0.045	0.9

Table 4.3: Recipes of preparation steps [18]. \*NI (NanoIntegris), SA (Sigma-Aldrich)

## 2. Main Procedure: Sorting CNTs

As we discussed, diameter separation is done by SDS and DOC. While concentration of DOC is fixed, at 0.04 %, SDS concentration is varied with diameters as the overall guide line of the separation. And metallic and semiconducting separation is done by SDS and SC. Often metallic and semiconducting separation is proceeding after diameter separation, and concentration of DOC should be under 0.02 % not to be affected by diameter separation effect [25]. A biphasic system is made when the vial is left in ambient condition by natural gravity or low speed centrifuge. Low speed centrifuge accelerates separation speed and time, so we apply 1,500 rpm for 3 minutes with ST8 bench top centrifuge manufactured by ThermoFisher.

Fig.4.8 captures the highlights of ATPE procedure for CoMoCAT and HiPCO SWNTs: SG65i, SG76, and SWNTs by Sigma-Aldrich and NanoIntegris. Diameter range of these SWNTs is 0.7 - 1.3 nm so that concentration range of SDS is between 0.6 % and 1.0 % for diameter separation. When we start with diameter separation, the first aim is grouping larger diameter SWNTs and smaller diameter SWNTs whose boundary concentration of SDS is around 0.75 %. Then, we move to metallic and semiconducting separation. For this separation, concentration of SC is fixed, at 0.9 % and SDS concentration is up to 1.1 %. NaClO is added in order to oxidize the solution at the end of mixture. Its amount is 6 - 8  $\mu\text{L}$  per 1 mL of total volume. Here we use NaClO for 1/100<sup>th</sup> diluted solution. Whenever separation with handling higher concentration surfactants, a serious care is required to form a biphasic system. In order to obtain pure SWNT solutions, repeated ATPEs are done.

The successful sorting recipes are obtained through concentration monitoring at each step with the following assumptions. PEG and DX are separated and only exist in each top or bottom phase. For example, when we discard top phase, we consider and calculate only the bottom DX phase. Another assumption is that surfactants are homogeneously distributed so that concentration of surfactants in solution is same. In this way, we have calculated and proceeded with assumptions and the process went well.

In case of SG76 and SWNT by Sigma-Aldrich, it starts with metallic and semiconducting separation. However, once it is done that separation, the rest of steps are same.

The summary of this simple metallic and semiconducting separation recipe with SG65i is as below. It is only four steps to complete metallic and semiconducting separation well. Steps (1) and (2) are for diameter separation, and steps (3) and (4) are metallic and semiconducting separation.

1. Surfactants : SDS 0.7 %, DOC 0.04 % / Polymers : PEG is around 9 - 10 % and DX is around 5 - 6 %
2. Surfactants : SDS 0.75 %, DOC 0.04 % / Polymers : PEG is around 9 - 10 % and DX is around 5 - 6 %
3. With greenish solution, surfactants : SDS 0.7 %, SC 0.9 % / Polymers : PEG is around 9 - 10 % and DX is around 5 - 6 % / NaClO 2  $\mu\text{L}/\text{mL}$

4. With black purplish solution, surfactants : SDS 1.1 %, SC 0.9 % / Polymers : PEG is around 9 - 10% and DX is around 5 - 6 % / NaClO 2  $\mu$ L/mL

#### 4.2.4 Post-Process: Characterize solution for chirality and do polymer exchange

After ATPE is done, there are two essential tasks; one is characterization step that is crucial to confirm the chirality in solutions. We perform two optical characterization methods: UV-vis and Raman spectroscopy measurement. These will be discussed next section of optical characterization in detail.

The other important step is polymer exchange. This step to remove polymers and lower surfactant concentrations for real applications. There are two ways to achieve this task using centrifuge and pressure. Both methods have same concept, dilute the SWNT solution by adding DOC 0.04 % and filtrate polymers with membrane. Here, the filtration process is assisted by centrifuge or pressure.

Amicon Ultra-15 tubes with membrane 10 kDa made by Millipore-Sigma are used for centrifuge. Centrifuge condition is related to the concentration of polymers, normally PEG is faster than DX. Adding SWNT solution 2 mL and 0.04 % DOC 10 mL can fill the volume of the tube around 13 mL. We normally repeat the exchange five times diluting surfactant concentration and removing polymer as much as possible. Amicon Stirred Cell with Ultrafiltration Discs 100kDa with membrane exploits pressure. This method is able to filtrate relatively fast with bulk amount depending on the size of Amicon Stirred Cell. Our recipe with Amicon Stirred Cell is in progress for handling larger volumes of sorted solutions.

### 4.3 Optical Characterization

As discussed in chapter 2, semiconducting SWNTs have unique band gap energy values related to the chirality and that band gap energy is quantified by absorption spectrum. This absorption spectrum is obtained by UV-vis spectroscopy. Raman spectra can also inform not only chirality of SWNTs but also other characteristics such as chirality and defect modes.

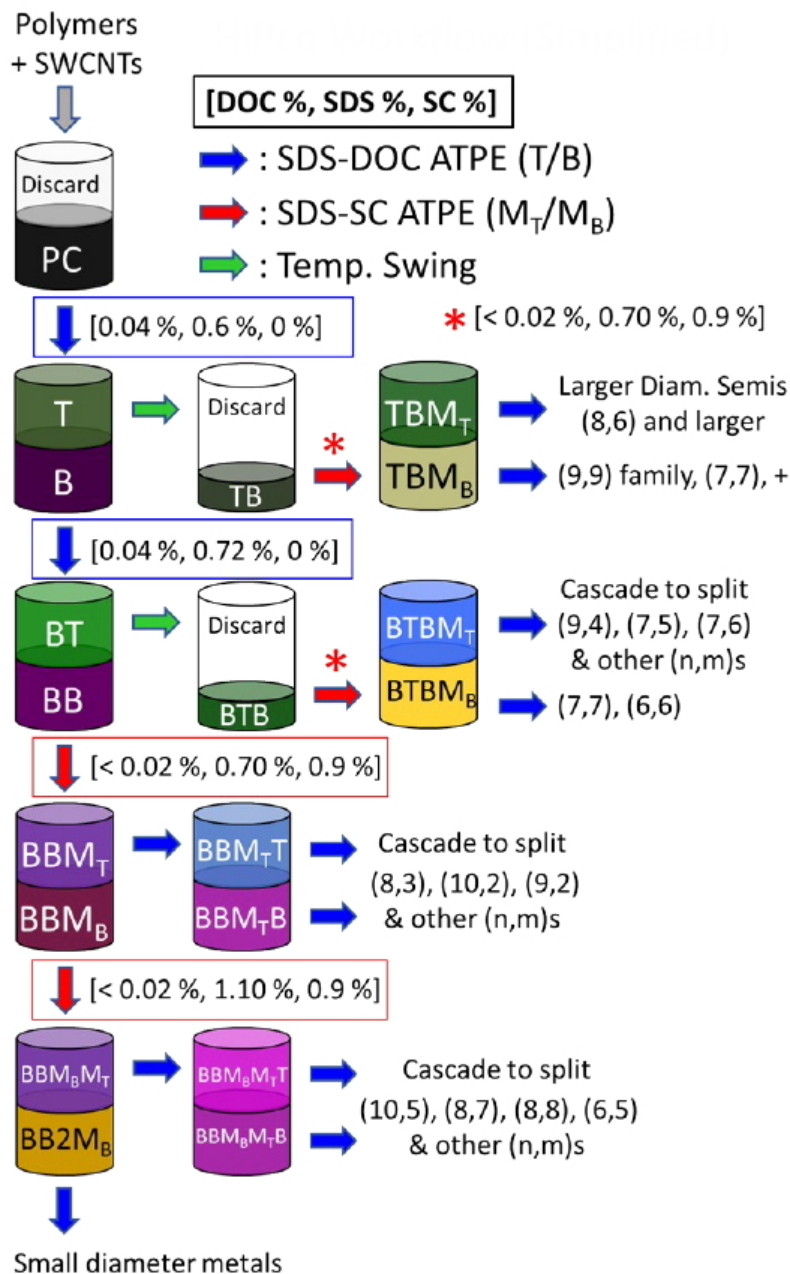


Figure 4.8: Generalization of ATPE process for CoMoCAT and HiPCO SWCNTs. (Reprinted with permission from reference [25].)

### 4.3.1 Absorption Spectroscopy

Absorption spectroscopy with UV-vis is the easiest and quickest method to figure out chirality indices and composition of SWNTs in solution. The principle is shining the broad band white light, typically 200–2,000 nm wavelength on the SWNT solutions and measuring the transmitted light. In this way, we can obtain absorption spectrum from differences between incident and transmitted light. In the UV-vis measurement, absorption spectrum is a plot of absorbance which is defined as an equation below,

$$\text{Absorbance} = \log_{10} \frac{\phi^i}{\phi^t} = -\log_{10} T, \quad (4.4)$$

where  $\phi^i$  is the intensity of the incident light,  $\phi^t$  is the intensity of the transmitted light, and  $T = \frac{\phi^t}{\phi^i}$  is the transmittance of the material. So, absorbance is negative log of the transmittance. The absorbance is represented intensity as a function of wavelength, where we interpret the wavelength of strong peaks which is translated to band gap energy.

Fig.4.9(a) is a series of absorbance plots as a function of wavelength with sorted SWNT solutions. Although y-axis is arbitrary units, we can readily identify peaks and distinguish differences between chirality. When we look into certain spectrum, there are at least two peaks in a spectrum which may be from sorted pure SWNTs since there are possible. The peaks may correspond to transitions of  $E_{11}$ ,  $E_{22}$ ,  $E_{33}$ , etc. In these plots,  $E_{11}$  region is above 800 nm in wavelength. Two sorted peaks at 1,000 nm and 600 nm in (6,5) spectrum may be assigned that. 1,000 nm is  $E_{11}$  and 600 nm is  $E_{22}$  of (6,5) SWNTs. Because the transition energy of  $E_{11}$  is smaller than  $E_{22}$ , the wavelength of  $E_{11}$  should be longer than  $E_{22}$ 's.

In principle, emission spectrum is related to absorption spectrum shown in Fig.4.9(a) and Fig.4.9(b). Fig.4.9(b) is a photoluminescence map of a SWNT solution. Emission wavelength is shown in x-axis and excitation wavelength is in y-axis. Emission wavelength of (6,5) indeed matches well with absorbance wavelength as we know. Here, hidden information comparing two plots is that we do not secure the excitation wavelength with respect to the absorbance wavelength, but there are certain excitation wavelength which makes high intensity of emission wavelength. I presume that this is because of van Hove singularity, which is the narrow band coming from the 1-dimension nature of SWNTs. This property appears in the Raman spectroscopy, which we will discuss in next subsection.

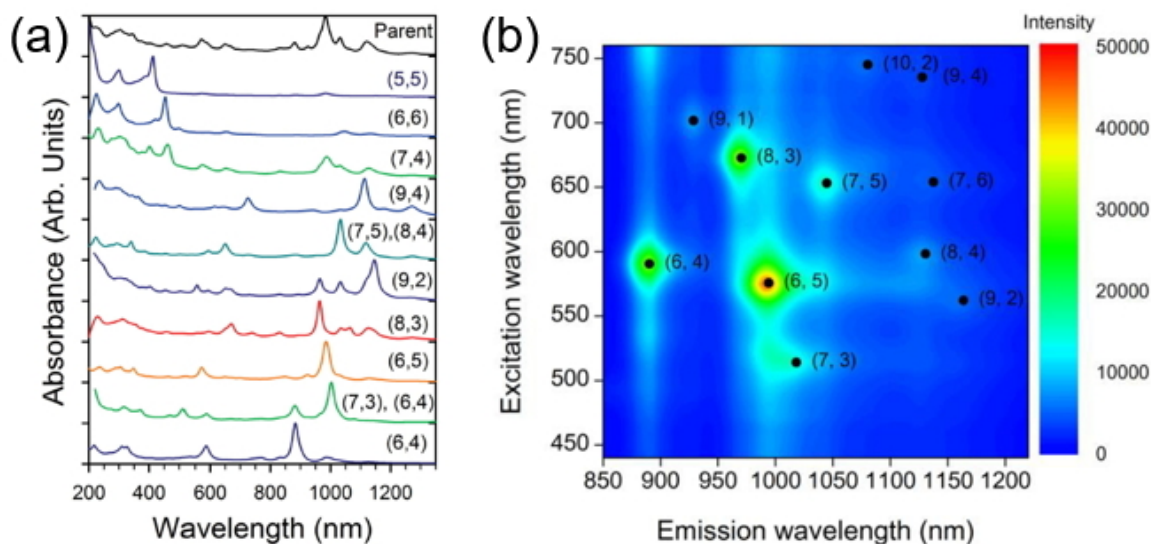


Figure 4.9: (a) Absorbance results with sorted solutions of SWNT. (Reprinted with permission from reference [27]. Copyright 2014 WILEY-VCH Verlag GmbH & Co. KGaA, Weinheim.) (b) Photoluminescence map of (6,5) SWNT solution. (Reprinted with permission from reference [6].)

### 4.3.2 Background Extraction

When we analyze absorbance spectra, we notice that a slope in shorter wave length area which is below 400 nm, becomes steeper than that in longer wavelength. Certain spectrum is remarkably steeper than others. And non-existence area of absorbance should be zero intensity, but there are still certain amount of intensity exist. This phenomenon is explained as background intensity shown in Fig.4.10. This plot shows absorbance of before sorting in, black line, and after sorting in, red line. In the sorted solution, two specified areas are indicated as area A and area B. Area A is a real intensity coming from absorbance intensity and area B is background intensity. Naumove *et al.* explain several causes of background intensity in terms of extrinsic and intrinsic factors [68].

- Extrinsic factors
  1. Ultrasonication: From the turbulence of surfactant solution, there is light scattering which prevents absorption. Three different tip sonication results

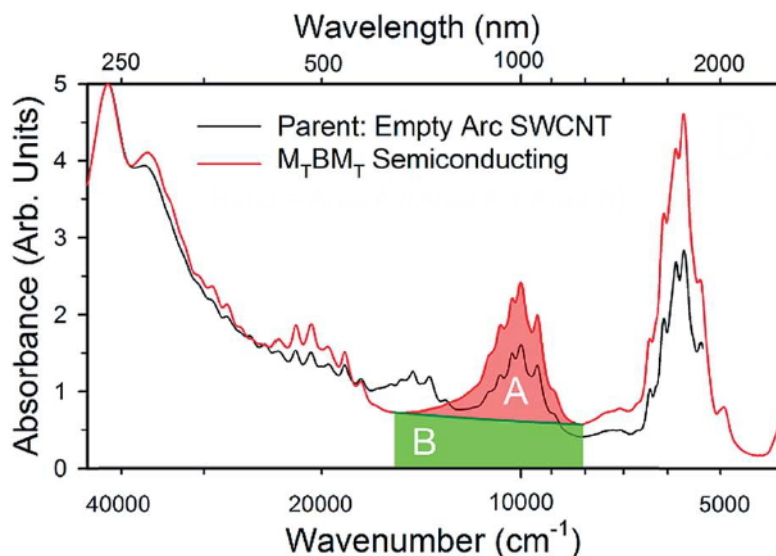


Figure 4.10: Absorbance spectrum with background spectrum. (Reprinted with permission from reference [25].)

show that longer sonication absorbance graph has higher background intensity and return to the initial level after centrifugation.

2. Chemical functionalization: Treating the side walls of SWNT with chemical elements, delocalized electrons in  $p_z$  orbital are removed and optical performance is degraded. Oxidized SWNT solution shows broader peaks and steeper slopes.
3. Amorphous carbon impurities: Amorphous carbon has strong plasmonic absorption in a short wavelength region. This is a reason why the slope of near-ultraviolet wavelength region is steeper than in other region.
4. Aggregation: Aggregated SWNTs are similar to the functionalization effects. This bundling effect broadens the spectrum and shifts the peak to longer wavelength (red shift). Making a good dispersed solution is an essential task.

- Intrinsic factors

1. Spectral congestion: With many chirality in a solution, there are many absorbance peaks in a plot and summing up those absorbance peaks lifts up

the plot. Sorted SWNTs have low background intensity compared to unsorted SWNT solution.

2. SWNT length effect: The end of SWNTs is considered as a defect in the  $\pi$ -electron system. From this reason, population of shorter length of SWNTs acts as more defect than longer length of them, resulting in stronger background signals.
3. Metallic SWNT contributions: Signals in metallic SWNTs are more intense arising from the  $\pi$ -plasmon resonance than those in semiconducting SWNTs.

### 4.3.3 Analysis with Protocol through Background Extraction

Due to previous reasons on background intensity in absorbance spectrum, we have put a much efforts on establishing a systematic protocol to extract the background intensity for obtaining a pure absorbance spectrum with which we try to calculate the purity of SWNT solutions such as metallic xx % or semiconducting xx % in a solution [17]. Sequences of the protocol are described as below.

1. Modeling background:

As we discussed in the background extraction subsection, we can model it as below [68],

$$B_{\lambda} = \frac{N}{\lambda^m}, \quad (4.5)$$

where  $B_{\lambda}$  background intensity with respect to the wavelength  $\lambda$ , and  $N$  and  $m$  are fitting parameters.

2. Determining coefficient  $A$  and  $m$  by fitting:

Because the linear regression has high fidelity, we have a trick to transform Eq.4.5 to the linear form by taking a logarithm,

$$\ln B_{\lambda} = \ln A - m \ln \lambda, \quad (4.6)$$

Unfortunately, this model does not fit all the absorbance spectra. However, we can secure the best fitting results by setting the different fitting range. Recommended range of the fitting range is 440 - 880 nm for semiconducting and 200 - 500 nm for metallic SWNTs. Once recommendation results do not fit well, we can adjust fitting region in the [graphic user interface \(GUI\)](#).

3. Subtracting the fitted background curve from the original absorbance curve.
4. Modeling a single peak of each SWNT:  
The absorbance peak of single chirality SWNT is known as a Lorentzian shape.
5. Finding peaks and multi-fitting with Lorentzian model for deconvolution:  
In order to deconvolute the mixed chirality SWNT solution, we need to extract peak wavelengths and multi-fitting with the Lorentzian model.
6. Calculating curve areas from fitting and purity of metallic or semiconducting:  
Based on the fitting results, we can calculate the area of curve and grouping metallic or semiconducting regions. As we know the chirality,  $M_{11}$ ,  $S_{11}$ , and  $S_{22}$  region are pretty much fixed. For the SG65i and SG76 cases,  $M_{11}$  ranges between 430 and 590 nm,  $S_{11}$  lies in between 850 and 1070 nm, and  $S_{22}$  is around 500 - 810 nm. Actually,  $S_{11}$  region is narrower than the real range, upto 1,700 nm, because of the equipment limitation, upto 1,100 nm. By using the ratio of the areas, we can quantify the purity of the sorted solutions.

Fig.4.11 shows the ATPE analysis protocol program. (a) is the main page of the control panel. As can be seen, we can set the fitting and transition regions. There are also the Raman analysis section, but it is under development. The analysis results are displayed in the information panels located in the middle, and data is stored automatically in excel file. When it performs analysis, there are graphs popping up with estimating the results and renewing the setting values in real time.

#### 4.3.4 Raman Spectroscopy

Raman spectroscopy gives the information of SWNT structure, electronic, and phonon properties. The principle is shown in Fig.4.12. There are three scattering modes which are Rayleigh scattering, Stokes scattering, and anti-Stokes scattering. Rayleigh scattering is a common and normal scattering mode, but the rest of two are related to Raman spectroscopy. When an incident light shines into a material, there are losing energy or gaining energy due to phonons. If it is the losing energy case, it is Stokes scattering and the gaining case is anti-Stokes scattering. Raman spectroscopy are sensitive to detect these energies and shows as a function of frequency with the common unit of  $\text{cm}^{-1}$ . Stokes case represents a longer wavelength than incident wavelength, so it is located in the positive side. Anti-Stokes case is vise-versa. Basically, Raman spectroscopy also measures the light of energy from excitation. Results should be affected by incident

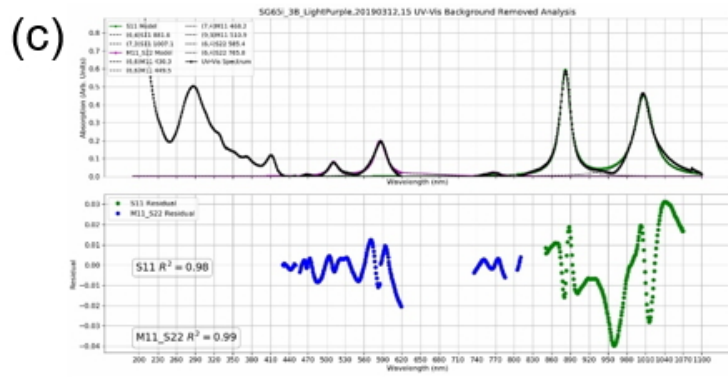
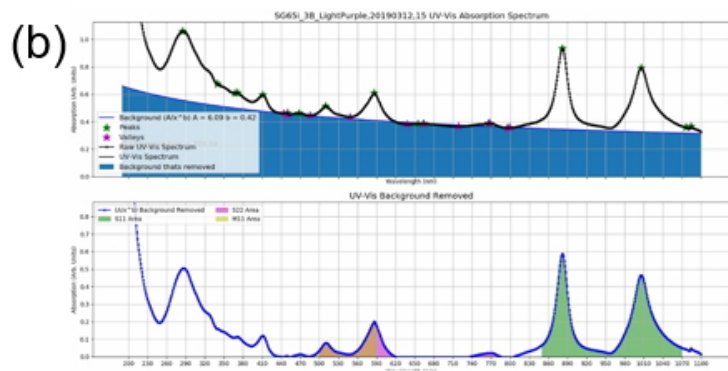
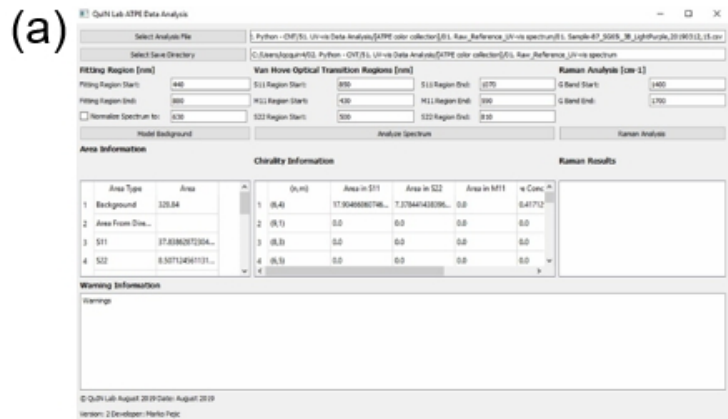


Figure 4.11: Analysis protocol program of background extraction. [17] (a) Main control panel of analysis protocol program. (b) Plot of background extraction result. (c) Plot of deconvolution results.

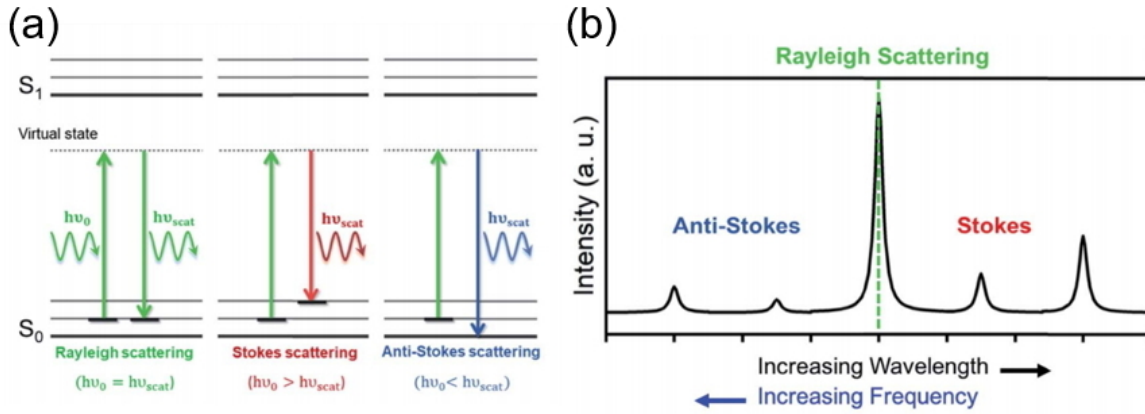


Figure 4.12: Picture of the principle of Raman spectroscopy. (Reprinted with permission from reference [84].) (a) Image of scattering mode. (b) Image of position in wave number domain.

wavelength of the light if it has discrete energy bands like **SWNTs**. There are different Raman results depending on the wavelength related to chirality observed.

From the **CNT** perspective, there are three remarkable modes: **radial breathing mode (RBM)**, D, and G mode. **RBM** mode is known as quite diameter dependent modes and there are several models [23, 52, 86]. A D mode is related to the defects in **CNTs**. The spectra are taken before and after treatment, with which we are able to judge whether **CNTs** are damaged or not due to the treatment. G modes are divided into two,  $G^+$  and  $G^-$ . Shapes of those two modes indicate metallic or semiconducting. These modes are explained below equation and coefficient are arranged in Table 4.4 [23].

$$\omega = \omega_0 + \frac{\beta}{d_t^n}, \quad (4.7)$$

where  $\omega$  is Raman frequency,  $\omega_0$  is the value for  $d_t \rightarrow \infty$  fit by Raman data,  $n$  is exponent,  $\beta$  is diameter coefficient, and  $d_t$  is diameter of **SWNT**.

### 4.3.5 Separation Results by Aqueous Two-Phase Extraction

Our **ATPE** results show possibility of separation of **SWNTs**. It does not give pure separation results yet, but we have semiconducting 100 % based on our protocol analysis. Here we will present several sorting results: common colors using SG65i and SG76,

Mode	Raman Frequency [ $\text{cm}^{-1}$ ]	Exponent	Diameter coefficient	Reference
RBM	0	1	248	[52]
	18	1	215	[86]
	10	1	218	[86]
	17	1	223	[86]
D	1356	1	-16.5	[28]
G <sup>+</sup>	1591	0	0	
G <sup>-</sup>	1591	2	(-45.7:-79.5)	[51]

Table 4.4: Raman modes in SWNTs [23].

simple separation of SG65, simple separation of SWNTs from HiPCO. And we will examine parent solutions which is before separation SWNT solution and polymer effect.

### Common colors using SG65i and SG76

This section we presents the results of separation with SG65i and SG76 solutions. These are synthesized by the CoMoCAT method as mentioned and the diameter range of SWNTs is 0.7 - 0.9 nm. Both solutions primarily contain (6,5) and (7,6) chirality. As can be seen in Fig.4.13, there are eight colors of solutions in a 14.7 mL vial, commonly observed during separation. Light purple, purple, blue, blue green, forest green, yellow, orange, and purple brown from the left to right. The color of (6,5) is purple and (7,6) is green. Even though we cannot go pure single chirality sorting, we can obtain 100 % pure semiconducting solution which is pale blue. For the metallic case, we secure up to 79.5 %. Those percentages are calculated by the protocol analysis code which we

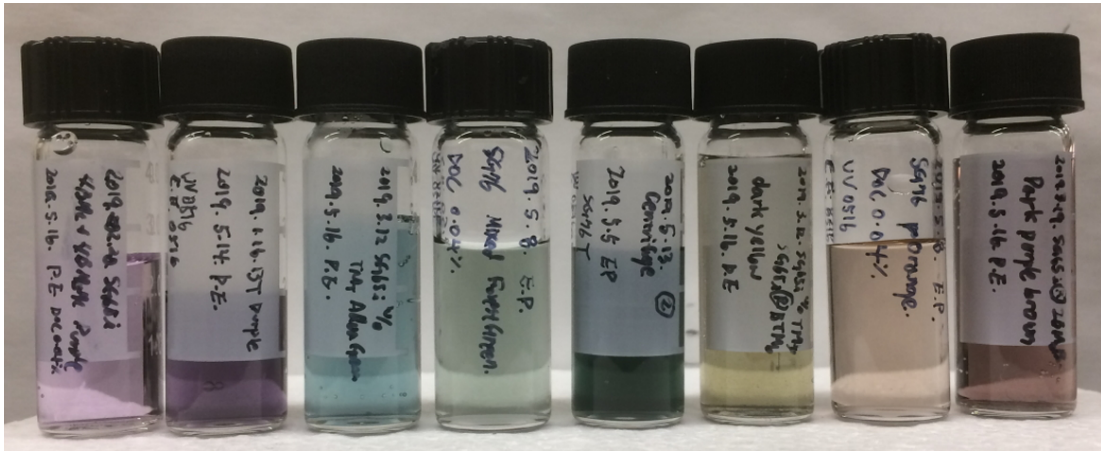


Figure 4.13: Common colors of ATPE separation results from SG65i and SG76.

mention previously. Fig.4.14 collects there are absorbance data for eight color solutions. These are normalized data by a signal at 630 nm and plots in waterfall modes to compare each other. Yellow and orange colors are metallic and the other is semiconducting dominant. Unfortunately, our UV-vis equipment measures up to 1,100 nm, it cannot detect (7,6) in  $S_{11}$  region but we can figure out by color. Detailed analysis is arranged in below Table 4.5 below.

Among eight colors, six colors solution are measured by Raman spectroscopy. Incident laser is at 532 nm and data are presented in Fig.4.15 and Fig.4.16. Fig.4.15 shows RBM mode and Fig.4.16 is D and G mode. As Raman spectrum data includes background intensity which is measured without light, it is extracted and plots are drawn using a waterfall method. When samples are drop casted on a silicon substrate, silicon factors are also observed independently. In Fig.4.15, there are three different peaks from silicon so that we can interpret Raman peaks only between  $200 - 300 \text{ cm}^{-1}$ . We tried to match with the absorbance data results, but there are no consistent results found. Absorbance data are good for identifying chirality indices. However, metallic and semiconducting properties are clearly distinct in the G mode around  $1,600 \text{ cm}^{-1}$  indicated in Fig.4.16. Description: metallic has broad shoulder in Raman shift whereas semiconducting has strong  $G^+$  peak. As we observed in absorbance data, orange color

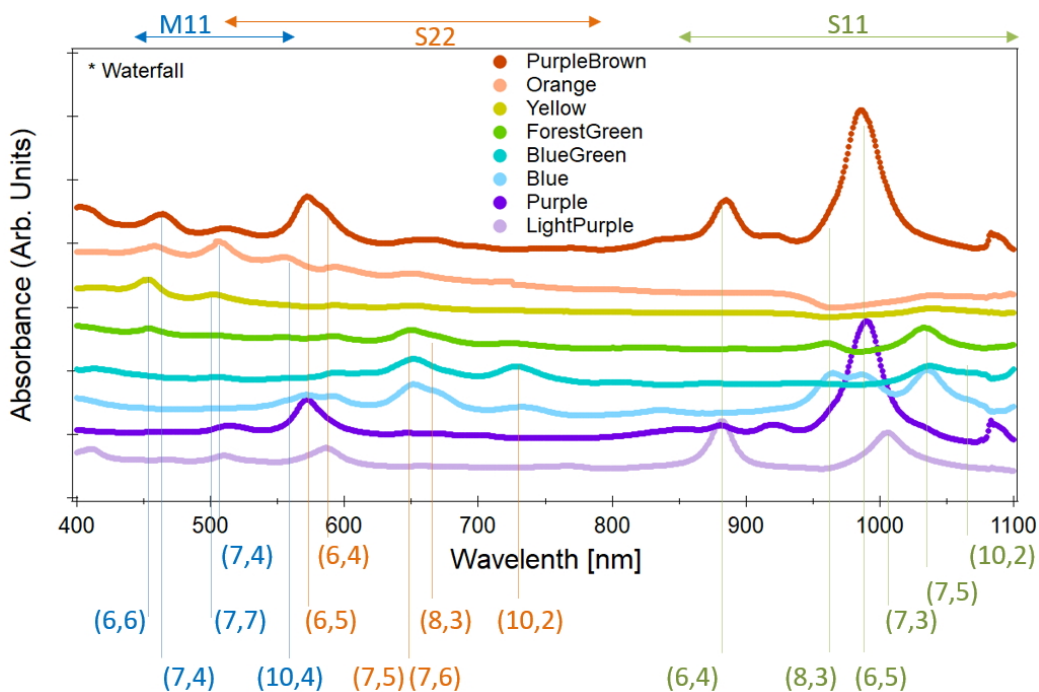


Figure 4.14: Absorbance spectrum for common colors of ATPE separation results from SG65i and SG76.

solution shows about 79 % metallic property. In this Raman spectrum, it also clearly shows metallic property and others are semiconducting.

### Simple Separation with SG65i

As we have understood and equipped ATPE separation method, we tried to make it simple in order to fabricate devices starting with metallic and semiconducting solutions. The first trial is with SG65i. Dominant clarity in SG65i is (6,5) and (7,6) and metallic, and with this, we can extract solutions of blue green, purple and yellow via five-times ATPE separation. From these separations, blue green is semiconducting 96.0 %, purple is semiconducting 88.2 %, and there are two different deep yellow colors, one is from blue green which is  $TM_b$  showing metallic 65.7 % and the other is from purple,  $2BM_b$ , 69.1 % metallic. These are described in detail in Table 4.6. This simple process is quite convenient to yield bulk amount. In order to make a better metallic solution, we must determine more accurate  $NaClO$  amount. Fig.4.17 shows bulk amount of blue

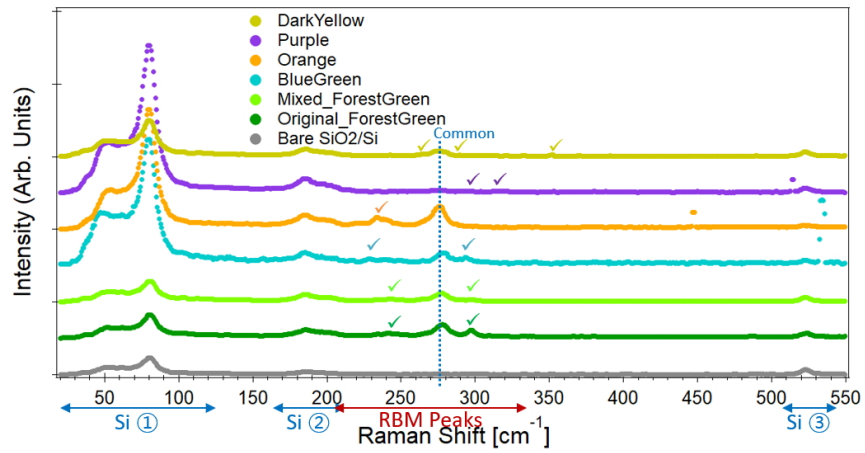


Figure 4.15: RBM mode in Raman spectroscopy for common colors.

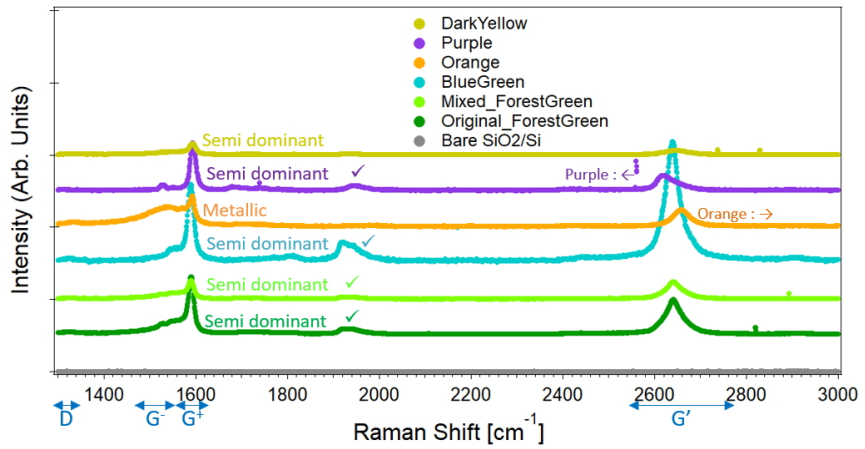


Figure 4.16: D and G mode in Raman spectroscopy for common colors.

Color	Dominant chirality	Semiconducting	Metallic
Light purple	(6,4) 77.2 %	98.8 %	1.2 %
Purple	(6,5) 81.0 %	87.7 %	12.3 %
Blue	(7,5) 60.1 %	100 %	0 %
Blue green	(7,5) 53.1 %	92.4 %	7.6 %
Forest green	(7,6) 70.4 %	86.4 %	13.6 %
Yellow	(6,6) 37.1 %	52.1 %	47.9 %
Orange	(9,3) 32.0 %	20.4 %	79.6 %
Purple brown	(6,5) 66.5 %	88.3 %	11.7 %

Table 4.5: Absorbance data for common color solutions from SG65i and SG76.

green and purple in 250 mL bottles.

### Simple Separation with HiPCO SWNTs

We also tried to apply a simple separation method in HiPCO in order to sort metallic and semiconducting solutions. Because both solutions have large range of diameters, 0.7 - 1.3 nm, compared to SG65i and SG76, it seems that the separation does not give good results with simple steps. At the beginning, at least several steps are added for initial diameter sorting followed by metallic and semiconducting sorting in several steps as well. The colors and detail values are displayed in Fig.4.18 and Table 4.7, respectively.



Figure 4.17: Simple process sorting results with SG65i in bulk bottles.



Figure 4.18: Simple process sorting results with HiPCO SWNTs.

Color	Dominant chirality	Semiconducting	Metallic
Blue green	(7,5) 64.5 %	96.0 %	4.0 %
Purple	(6,5) 81.0 %	88.2 %	11.8 %
Deep yellow TM <sub>b</sub>	(6,6) 65.7 %	34.3 %	65.7 %
Deep yellow 2BM <sub>b</sub>	(6,6) 69.1 %	30.9 %	69.1 %

Table 4.6: Absorbance data for simple sorting process with SG65i.

Color	Dominant chirality	Semiconducting	Metallic
Greenish Blue	(7,5) 42.1 %	89.2 %	10.8 %
Brown - TM <sub>b</sub>	(9,3) 37.4 %	19.5 %	80.5 %
Pink	(10,4) 40.9 %	49.8 %	50.2 %
Brown - T <sub>2</sub> M <sub>b</sub>	(6,6) 66.0 %	19.3 %	80.7 %

Table 4.7: Absorbance data for simple sorting process with HiPCO.

### Polymer Exchange Effect on Absorbance

Polymer exchange step is an inevitable process at the end of ATPE in order to remove polymers for applications because we think polymers hinder the good quality or property on the applications. Checking this concern, we need to assess absorbance results with and without polymers. We have to also measure with polymers during ATPE as we do not remove polymer while sorting. Comparison polymer effects is represented on Fig.4.19.

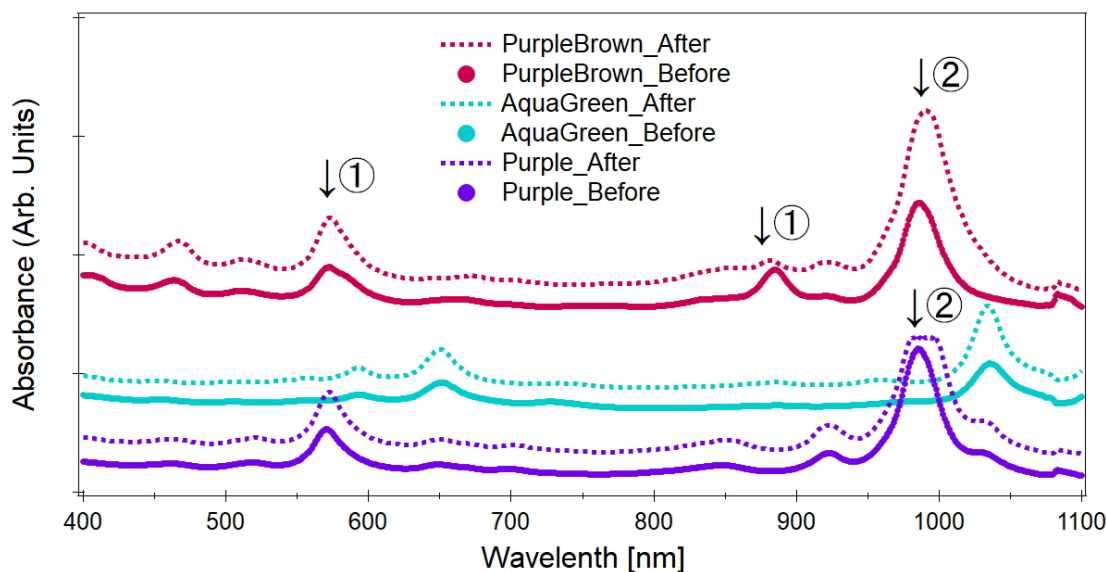


Figure 4.19: Absorbance comparison with and without polymer.

We have three color samples which chirality covers all measurement range: purple, aqua green, purple brown. And the plots in straight line are with polymer before polymer exchange and the plots in dotted line are without polymer after polymer exchange. Overall, the absorbance data with polymer indicate peaks well so that absorbance measurement with polymers during ATPE process is still acceptable. However, there are couple of checking points we had better take into account. ① Fig.4.19 shows the width of peaks are different between before and after. This may be related to aggregation of SWNTs as we discussed earlier. During polymer exchange process, we observed the extracted SWNTs which are on the side wall of the membrane and looked black. After polymer exchange, those particles are taken together and kept in a vial. This extraction of SWNTs affects deformation of peak shapes. Being noticed this phenomenon, we have done tip sonication with pulsed mode, 2-seconds-on and 1-second-off for 1 hour with aqua green solution in Fig.4.19. As can be seen, after sonication result becomes sharper peaks of the width. So we have learned that a tip sonication step is required after polymer exchange in order to disperse SWNTs well. The next caution point is ② we observed the peak wavelength red shift about 5 nm in different solutions. This may be explained by surfactant effect since surfactants are able to shift peak wavelength. Or it may come from contamination because we re-use polymer exchange tools. Even though we use the tools only for similar color solution, combination of chirality is different in similar colors.

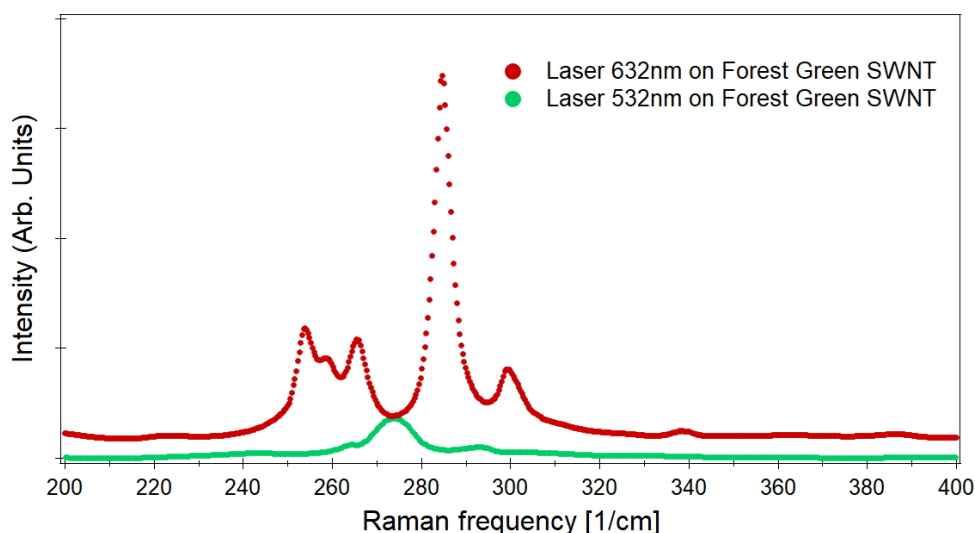


Figure 4.20: Raman spectroscopy RBM results of forest green solution with 532 nm and 632 nm incident laser.

### Raman Spectroscopy with Different Incident Laser

Raman spectroscopy also gives us information of [SWNTs](#) regarding diameter, metallic or semiconducting, defect, etc. The diameter separation is crucial for sorting because it is related to the chirality. However, results of Raman spectroscopy is hard to obtain the defined diameter information from without background information as the results are dependent on the incident laser. As we discussed, photoluminescence of [SWNTs](#) shows different emission light wavelength in Fig.4.9(b). From this reason, results of Raman spectroscopy of forest green color and purple color have different shape of [RBM](#) modes observing in Fig.4.20 and Fig.4.21. Fig.4.20 is the result of forest green solution and Fig.4.21 is purple. Forest green is (7,6) dominant solution and purple is (6,5) dominant solution. And incident lasers are at 532 nm and 632 nm. According to the Fig.4.9(b), emission light of (7,6) is about 660 nm and (6,5) is about 575 nm. This information is well-matched with Raman spectroscopy. As can be seen in Fig.4.20 and Fig.4.21, Raman spectroscopy peaks of forest green are well-observed in 632 nm incident laser which is closed to 660 nm, but incident laser 532 nm does not show well peaks. On the other hand, purple solution does not show Raman peaks well. Therefore, for the Raman spectroscopy measurement, we need some prerequisite information of [SWNTs](#) and prepare proper wavelength of lasers for isolating distinctive peaks to quantify diameters.

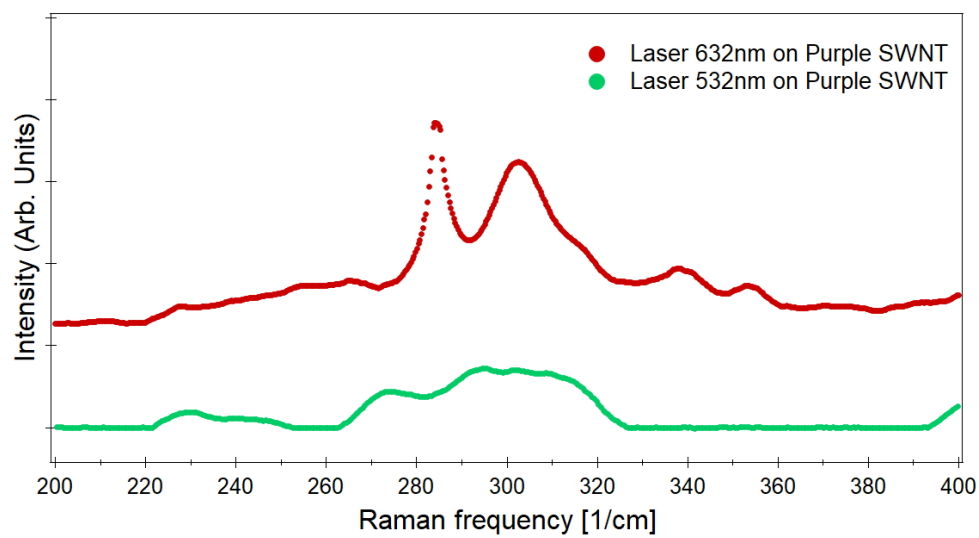


Figure 4.21: Raman spectroscopy RBM results of purple solution with 532 nm and 632 nm incident laser.

# Chapter 5

## Preparation of Carbon Nanotube Films

Sorted CNTs can make device in a substrate as one-dimensional wire, two-dimensional film, or three-dimensional bulk material for fabricating photonic, electrical or mechanical devices. Typically CNTs can be coated on substrates with various methods, which are grouped into two categories: direct deposition and solution based deposition [40]

### 5.1 Methods of making films

#### 5.1.1 Direct Deposition

As we discussed in the synthesis chapter, chapter 3.1, a CVD growth is a common method to synthesize CNTs together with arc-discharge, laser ablation. This CVD method needs catalysts as a seed of growth, which is deposited on substrates where we want to grow CNTs. Several treatments have been applied in order to align the CNTs while growth, either vertical or in-plane alignment in combination with patterned catalysts and external fields. This method is good to make CNTs directly on the points where we want to deposit, but there are several disadvantages. It remains huge amount of unused catalysts, is hard to control density of CNTs, does not place in many substrates at a time, and exposes substrates to high temperature and pressure which can affect negative influence on devices [40].

## 5.1.2 Solution-Based Deposition

Fabricating with solution-based deposition does not need high temperature and pressure as it does not put substrates in a chamber, and proceeds in ambient condition. However, the key factor of this process is how much CNTs are well dispersed in solvents. With surfactants, polymers or functionalizations, CNTs are well dispersed in solvents. Adhesion between CNT films and substrates and drying conditions are more consideration factors. There are many methods to deposit CNT solutions as below [40].

- **Langmuir-Blodgett (LB) method:** This is done by floating the CNTs on water and lifting up or dipping a substrate. Uniformly dispersed CNTs on water is related to the uniform film quality. Iteration of deposition makes thicker and denser films.
- **Self-assembly:** This process is with chemically treated with, silane or polymer, surface of substrates interact with CNTs by electrostatic Coulomb forces and CNTs form and adhere that on the substrates by van der Waals forces. This method is known as a quick and cheap process.
- **Dip coating:** CNTs are coated by picking-up a substrate from a CNT solution. Advantage of this coating is that CNTs are coated both substrate sides. Depending on the solution viscosity, pick-up time, and drying condition determine thickness, uniformity, and adhesion of the film.
- **Spin coating and drop casting:** Two methods are basically similar as CNT solution drops on a substrate, but spincoating is spinning and try to make the solution uniform. Solution viscosity and dry condition will also determine the quality of the film. These are easiest and quickest way of making films.
- **Electrophoretic deposition:** CNT films are formed on conductive substrates which have locally charged area by DC electric field. In order to do that, substrates are needed to be patterned by metal layers before applying the field.
- **Dielectrophoresis:** This method is the opposite way of electrophoretic deposition. CNTs are deposited between metals and operated by AC electric field.
- **Spray coating :** This method exploits the concept of using spray which we use in everyday life. CNTs are sprayed onto a heated substrate. A nozzle size and pressure are crucial control factors to determine the quality of CNT films.

- Vacuum filtration method: Diluted CNTs are filtrated on a membrane which passes solvent except CNTs and make highly uniform and reproducible films. It requires transfer steps for putting the films onto a substrate.
- Mayer rod: A rod on which CNTs are coated sweeps substrates and CNTs are coated on the substrates. This method has an advantage of easily scaling-up.

## 5.2 Method of making films: Vacuum filtration

As discussed regarding methods of film making in chapter 5.1, vacuum filtration (VF) is one of the methods which can make uniform, film size controlled, surfactant removed, and location independent films. Especially, removing surfactants is a crucial point in order to make better contacts between CNTs and metal pads for electronic devices because surfactants that are wrapping CNTs can separated CNTs from metal pads. One disadvantage of VF is that a membrane transferring step is required on a target spot after filtration. However, this can be a advantage when we coat CNT films wherever we want to deposit and when we keep the filtration membrane and deposit it whenever we need. In this chapter, we will discuss about our own recipe of vacuum filtration. There are three steps in making films on a substrate: preparing apparatus and solution, making a film on a membrane with VF, and transferring the film on a substrate.

### 5.2.1 Preparing Apparatus and Solution

Several apparatus are required for the VF process. The main part of this apparatus consists of a cylinder, a filter, and a flask in Fig.5.1(a). Conceptually, CNTs in a solution, water with low concentration of surfactants, are filtered out and deposited on a membrane. Therefore, CNT solutions are added in the cylinder and the solutions are passing through the filter. Between the cylinder and the filter, a membrane is located and CNTs are deposited on the membrane. The rest of water and surfactants are penetrating the membrane and filter and remaining in the flask. In this case, evacuation through the hose assists a faster filtration speed.

For the control of the thickness of CNT films, we calibrate the color of CNT solutions and film thickness. Fig.5.1(b) shows 5 bottles of 1 mL solutions at different concentration, consequently different darkness in color of solutions. Solution ⑤ is a

mixed SWNT solution and shows 40 nm thickness and solution ④ is (6,5) dominant SWNT solution which is same thickness, 40 nm. The rest of three solutions are more dilute than previous two solutions, corresponded films show thinner thickness. These reference results are obtained with 2-inch diameter membrane. Due to the ignorance of the exact amount of CNTs in a solution, we calibrate our solutions with these reference samples in terms of darkness in color and estimate the thickness of films after VF. The VF assembly is purchased from Sigma-Aldrich for 1-inch and 2-inch size. Membranes are used to fit the size of each assembly. 50 nm-pore size of Nuclepore polycarbonate membrane made by Whatman for the VF. These membranes are hydrophilic and wetting agent is polyvinylpyrrolidone (PVP) and they are well dissolved in N-Methyl-2-Pyrrolidone (NMP). The membranes have different level of smoothen surfaces, so we Place a shiny side up and store the film by being shiny side down.

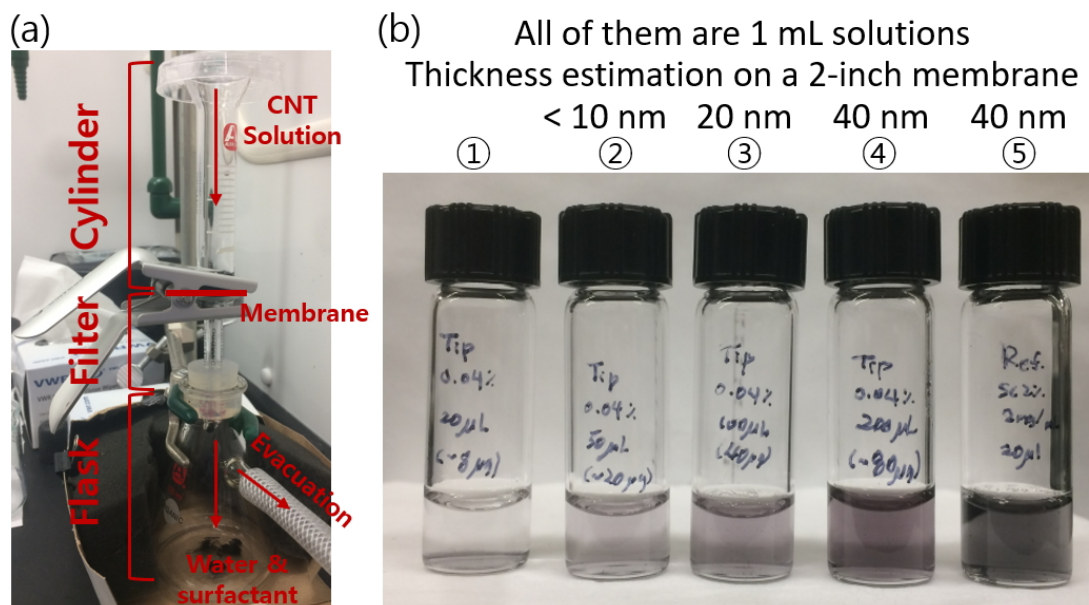


Figure 5.1: (a) Vacuum filtration apparatus and (b) thickness of CNT films for reference solution.

## 5.2.2 Making Film with Vacuum Filtration

Doing VF step is a waiting step because we need to wait until finishing filtration. However, adding solution part before starting pumping and the last suction part are

crucial points in order to make a good film. Once we prepare the solution which is compared with reference color solution for the target thickness, we do not fill the solution at a time. As soon as the solution reaches on a membrane, filtration is starting. So we need to fill MQW first about 4 mL and then add a CNT solution. Then we gently mix the solution with MQW in order to make the uniform solution. This is a important step at the beginning. Normally, the total 5 mL solution is used for 40 nm thick film and it takes about 5 minutes. After waiting for a while to pump out, the last moment of the filtration is an another critical point. Because the water solution is removing from the center of the membrane, increasing the speed of filtration is a factor for determining film uniformity at the end of the step even though previous uniformity of filtration was okay. Increasing a pumping power as much as possible is a key factor. When all solution is filtered out, we wait for a couple more minutes, take out the membrane, and gently blow with nitrogen gas to dry the membrane out. Fig.??(a) is a result of the VF to make a CNT film on a membrane. The black circular shape is a CNT film on a 2-inch membrane. Fig.??(b) is a transferred film on a substrate, where a blue colored area is a film and a purple colored region is thermally grown SiO<sub>2</sub> on Si substrate. A transferring process will be discuss in detail next subsection.

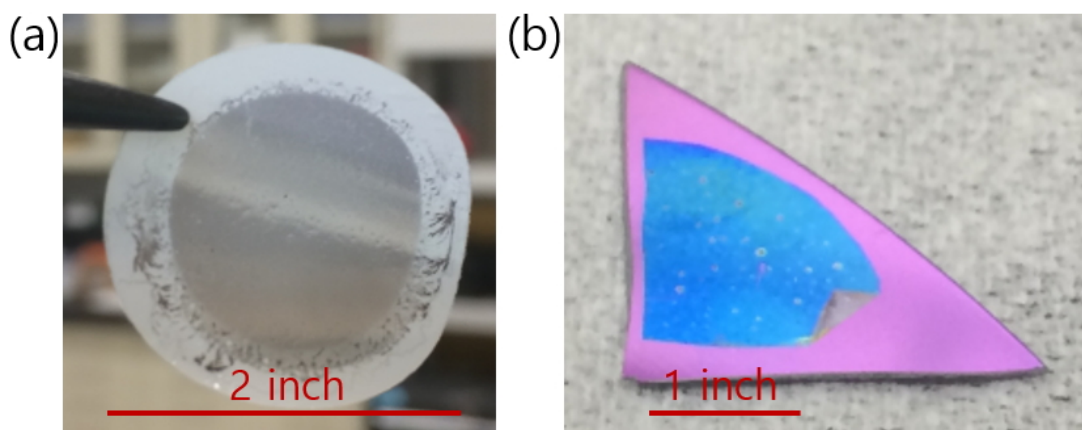


Figure 5.2: (a) CNT film on a membrane after vacuum filtration (b) transfer on a substrate with vacuum filtrated film.

### 5.2.3 Transferring on a Substrate

Transferring CNT films has a freedom of time and place for coating. We are able to adjust the size of the films within a membrane size and deposit them at any position of

substrate without the time limitation. The recipe of this transferring process is sketched in Fig.5.3. Basically, a CNT film is stuck on a substrate through van der Waals force. Nevertheless, the force is not strong enough that it is assisted by water. The first step, putting a drop of water on a substrate. This water increases adhesion for sticking a CNT film on a substrate well, but residue of water can make defects in CNT film which is not desirable for next step. The next step is to gently press the CNT film on membrane. As CNT should be on a substrate, CNT film side should be faced down to the substrate side, and covering it with a Kimwipe which prevents contamination during pressing the film. When the Kimwipe is removed, a film does not attach on the substrate sometimes. Then, try the step again from the beginning. Pressing the film gently, hardly, and uniformly results in a good quality of the film.

Once the film is on the substrate, next step is removing the membrane with NMP because NMP dissolves membrane. But it takes time to remove all the membrane clearly. We put the film on the substrate in NMP for more than one hour and rinse the film with new NMP because old NMP may contain dissolved membrane stuffs which can be re-deposited on the CNT film. Similarly, we rinse it in isopropyl alcohol (IPA) same manner; putting the CNT film in IPA for more than one hour and rinsing with new IPA. If there remain residues of the membrane on the CNT film, we can observe something covered with white stuff on the CNT film. In that case, we need to go back and put the film in NMP and repeat the rinsing steps. After all these steps are done, place the substrate on a hot plate, at 120°C for more than one hour. This step helps not only drying the film but also removing the surfactants.[2]

#### 5.2.4 Alignment Film: Another Advantage of Vacuum Filtration

He *et al.* demonstrate aligned SWNT films and they fabricate and characterize devices with aligned films [36]. They pointed out three important factors: surfactant concentration, CNT concentration, and speed of filtration. The membrane which contains a PVP film on the surface of the membrane is hydrophilic that generates negative charge fields. This field interacts CNTs and aligns CNTs with low speed of vacuum filtration process. Specific recipes are as below.

1. Preparing solution:

- DOC which is surfactant concentration is 0.04 %

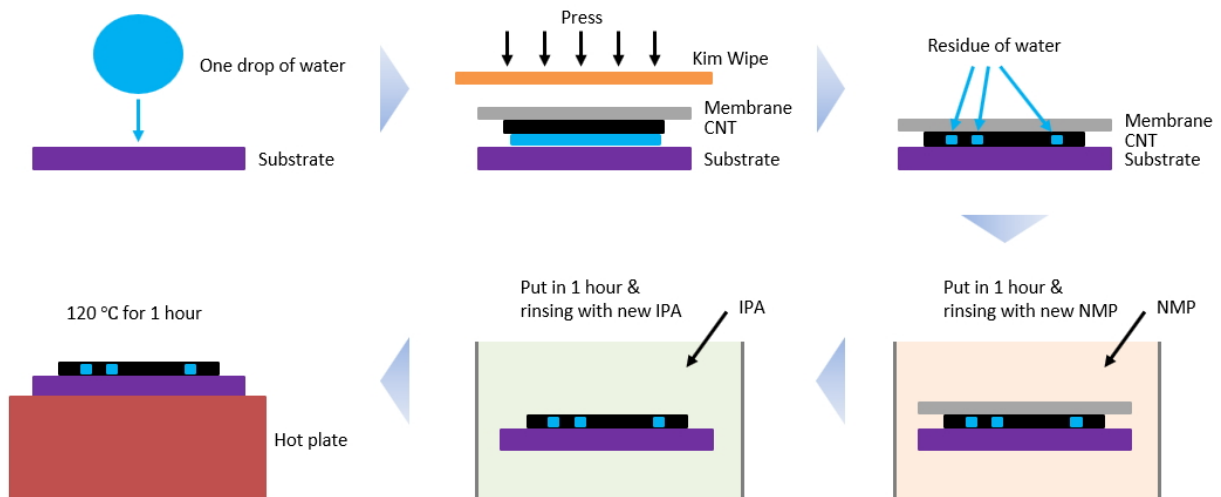


Figure 5.3: Recipe of transferring a CNT film on a substrate.

- Tip sonication: about 2 - 3 hours for arc discharge, about 11 hours for **CoMo-CAT**
    - \* Short length of the **CNTs** are recommended.
    - \* The average length of **CNT** is around 220 nm
2. Filtration speed: depending on the size of membrane
- 1-inch membrane: Around 3 water pressure for 1 - 1.5 hour for arc discharge and 2.5 - 3 hours for **CoMoCAT**
  - 2-inch membrane: around 2 water pressure
  - Indication of the speed: Normally, 8 - 9 minutes per 1 drop
  - End of the filtration speed: At the end of filtration, making the maximum speed of filtration.
3. Etching the surface of film:
- Light etching step: The last deposition layer is not uniform or aligned, it is good to etch in order to obtain well-aligned film for all stack.

## 5.3 Characterization of Films

Films are characterized in terms of thickness and surface roughness by [AFM](#), surface observation by [SEM](#), and resistance measurement by a probe station with Keithley 2450 and HP4156A.

### 5.3.1 Film Thickness and Surface Roughness

Measuring thickness of films is one of initial characterization items because this is a factor to determine resistance. And surface roughness is important when we observe the roughness of the film which is represented as the uniformity of the film. We are able to observe these two aspects by [AFM](#). Scanning the edge of the film after etching films shows the thickness of the films and the center of the film. Fig.5.4(a) is a representative [AFM](#) image, from which we acquire topological information. The width of the film is 30  $\mu\text{m}$  and the cross section for height measurement is done at each side of the film shown in Fig.5.4(b). The thickness is around 40 nm. This film is made by a [CNT](#) solution which is matching with reference solution ④ in Fig.5.1(b) of color thickness. In particular, this [SWNT](#) solution is metallic dominant (7,4) and (6,6) yellow color solution.

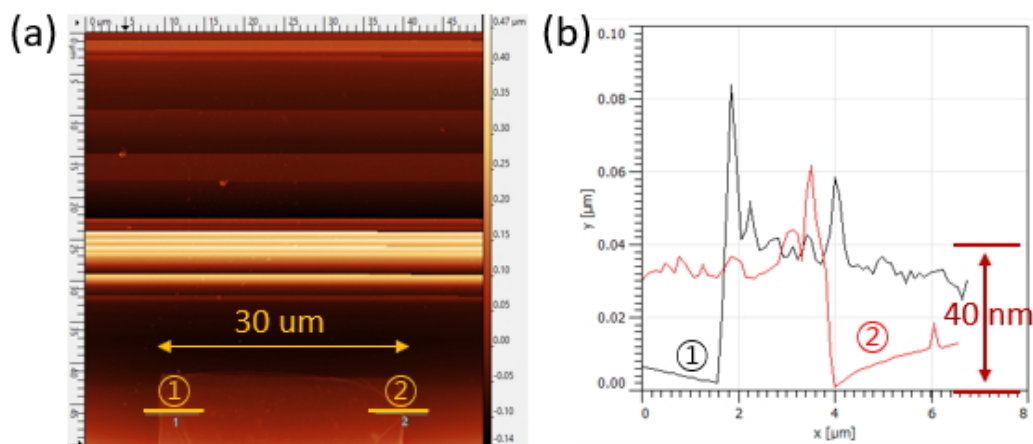


Figure 5.4: (a) [AFM](#) topological image of a CNT film on a silicon substrate. Width of the film is 30  $\mu\text{m}$  (b) The cross section of profiles at positions ① and ② indicated in Figure (a).

Roughness is also observed from scanning in the middle of the film. Fig.5.5(a) is the 2-dimensional image of the scanning result, the size of area is 500 nm by 500 nm.

Fig.5.5(b) is 3-dimensional image converted from Fig.5.5(a).  $R_a$  which is a mean value of the deviation from the height average,  $\sim 0.570$  nm,  $R_q$  which is a root mean square of the deviation from the height average,  $\sim 0.832$  nm, and  $R_{max}$  is a maximum difference between heights,  $\sim 19.7$  nm. Compared to the film thickness, 40 nm, the maximum thickness difference is almost 50 %. If we consider the diameter of SWNT is around 1 nm, this variation is quite large. Therefore, this big difference may be due foreign material contamination. In addition, we do not observe individual SWNTs in AFM results even though it is measured with lower than 1 nm resolution. This is because size of the tip and densely packed SWNTs which AFM probe cannot distinguish each SWNT.

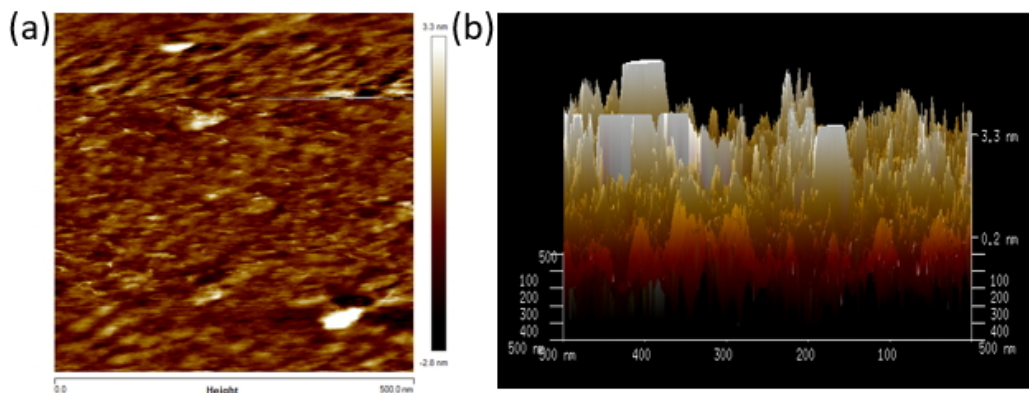


Figure 5.5: (a) Scanning the middle of the CNT film which is same in figure (4.4) (b) 3-dimension plotting for film surface.

In order to Observe the individual SWNTs, new measurements were attempted with small size of AFM tips. We try to understand the reason why we do not observe the single SWNT appearance with the size of AFM tip. Fig.5.6 sketches the configuration of a bigger size tip. The bigger size tip does not capture the single CNT. Tip size measured for Fig.5.4 and Fig.5.5 is average 8 nm and maximum 12 nm. Therefore, it is natural that we cannot observe each SWNT as this probe is much larger than the diameter of SWNT 1 nm.

We try to observe individual SWNTs in a spars (7,6) dominant SWNT film with a smaller tip, 2 nm size. As we expected, we are able to observe individual SWNTs and the diameter is around 1 nm what makes sense shown in Fig.5.7(a) and Fig.5.7(b). We assume that aggregated CNTs are larger than 1 nm and obviously they are readily observed in a scanning result. Although we examined the densely packed SWNT film

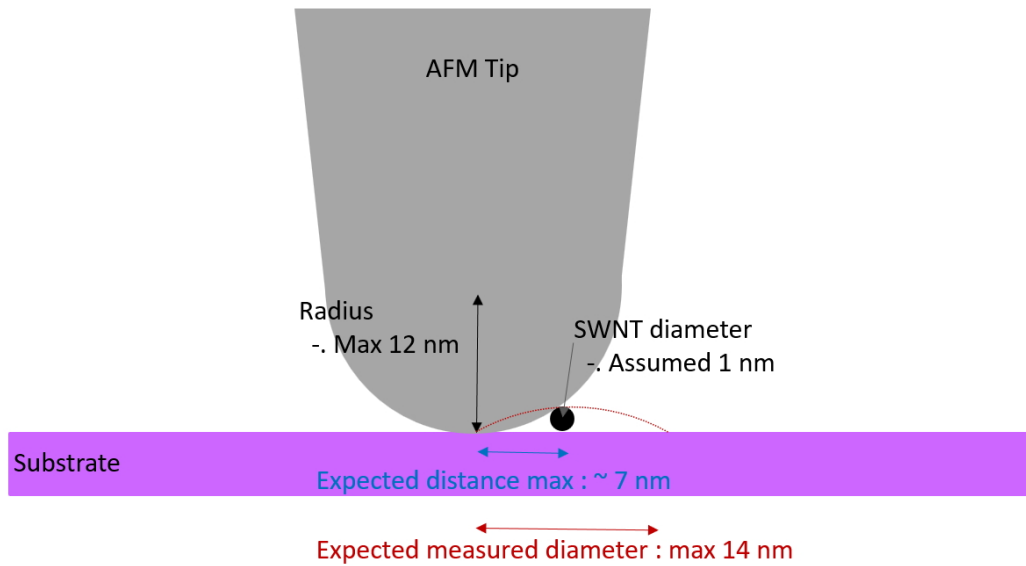


Figure 5.6: A scheme of scanning a strain CNT with a bigger AFM tip.

with the small tip, we were not able to catch individual SWNTs as the tip cannot still separate each SWNTs yet.

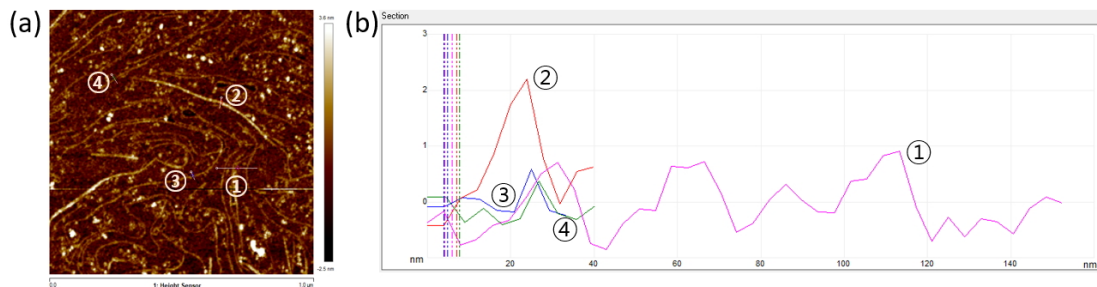


Figure 5.7: (a) AFM result with small probe (b) Height of cross section for thickness measurements.

### 5.3.2 Surface observation by Scanning Electron Microscope (SEM)

We attempt to look at individual SWNTs films under the SEM. There are three different film images in Fig.5.8; Fig.5.8(a) is a (6,5) dominant SWNT randomly oriented film, Fig.5.8(b) is a MWNT randomly oriented film, and Fig.5.8(c) is an aligned mixed

SWNT film. As we expected, the diameter of SWNTs is smaller than that of MWNT, while shape of each MWNT looks clearly visible. When we consider the resolution of the SEM, about 10 nm, the image of SEM may not represent the real size of the CNTs. Thinking with the scale bar, the size of SWNTs in image seems larger than the diameter 1 nm. In conclusion, this SEM image shows the shape of CNTs, but not the actual size of CNTs. In order to obtain the absolute value of CNT size, we may need to use TEM because its resolution is under nm.

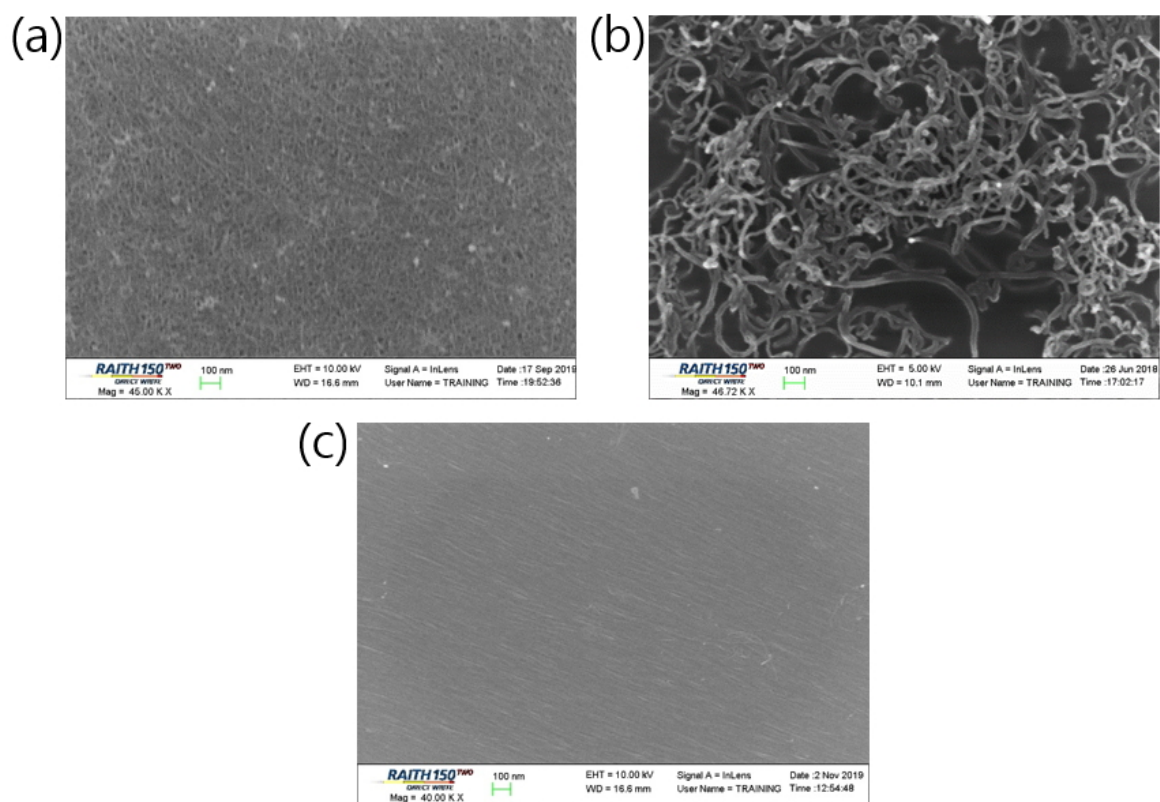


Figure 5.8: CNT films observation under SEM. (a) random direction of (6,5) dominant film (b) random direction of MWNT film (c) aligned with mixed SWNT film.

### 5.3.3 Resistance and Resistivity with Two-Probe Measurement

We measure resistance of CNT films by two metal contacts. A device is fabricated on a  $\text{SiO}_2/\text{Si}$  substrate in Fig.5.9. A metallic SWNT film is transferred to the substrate after

making by the VF method. Contact pads are evaporated with palladium (Pd) and gold (Au) for 2-terminal devices. We design different sizes of the CNT film regions. Arrays of devices are made with different sizes of the SWNT film regions: Size of width and gap. The devices have different width and gap with a uniform thickness, for example, 40 nm. Width varies 10, 20, 30, and 40  $\mu\text{m}$  and gap is 150, 250, 350, and 450 nm. Total 16 devices are included in a 1 cm-by-1 cm substrate. Details fabrication processes will be discussed in next chapter, chapter 5.

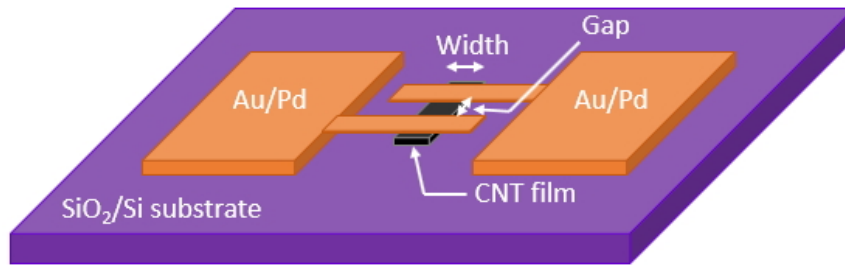


Figure 5.9: The schematic of a 2-terminal device. This is not a real size of ratio.

We measured resistance by voltage sweep, whose sweep range is from -10 mV to 10 mV with interval of 0.1 mV. There are 12 devices measured among 16 devices. Then, resistivity is calculated with a simple formula,  $R = \rho \frac{l}{S}$ , where  $R$  is resistance,  $\rho$  is resistivity,  $l$  is length of resistor and here gap in our device, and  $S$  is the surface of current flow and here width times thickness in our device. Resistivity is an intrinsic property so that it is expected to be a fixed value regardless of any variables. The results are summarized in Fig.5.10. There are all different resistance depending on the structure of SWNT film design. However, the resistivity which comes from the relation between resistance and resistivity with dimension values, is average  $0.448 \Omega \cdot \text{cm}$  and standard deviation  $0.261 \Omega \cdot \text{cm}$ . All resistivity data are positioned same order of data which is  $10^{-1}$ . The resistivity is expected to be  $1 \times 10^{-4} \Omega \cdot \text{cm}$  for the metallic SWNT [85]. Compared to the reference resistivity value, our data is higher about three orders of magnitude. We attribute this with a contact resistance between SWNT and metal pads because this is 2-terminal measurement. If we assume this SWNT is perfect metallic film and resistivity is  $1 \times 10^{-4} \Omega \cdot \text{cm}$ , resistance would be  $31.3 \Omega$  with width  $20 \mu\text{m}$ , gap 250 nm and film thickness 40 nm which are the film structure. From this assumption, contact resistance is estimated about  $740 \Omega$ , which implies that 96 % of the resistance would come from contact resistance.

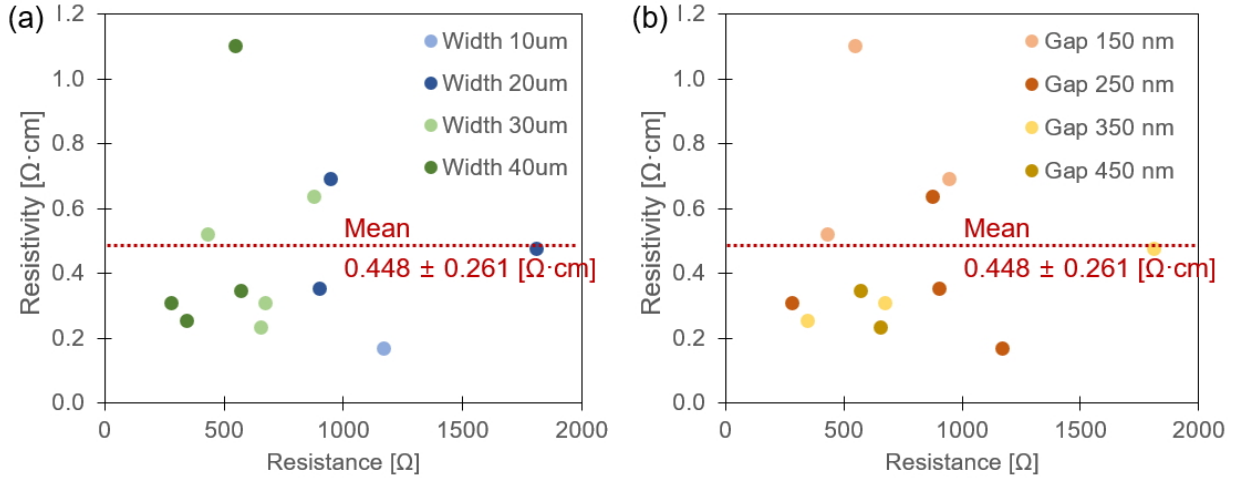


Figure 5.10: Resistivity results of 2-terminal measurement for SWNT film devices with different design factors: (a) for the width and (b) for the gap.

### 5.3.4 Resistance with Four-Probe Measurement

In order to remove contact resistance, we perform 4-terminal measurements directly contacting film with probes. The colinear four-point probe measurement method is used [55]. We measure the aligned SWNT films prepared by vacuum filtration method and the random direction MWNT films with LB method for this measurement []. There are interesting results we observe between different films summarized in Table 5.1, where four different cases are compared in terms of SWNT and MWNT, alignment.

First, we compare values from 2-terminal and 4-terminal measurements. If we assume difference between those two comes from contact resistance, 2-terminal resistance combines contact resistance and CNT resistance. When we take the ratio of two resistance values simply with the following formula, the results are between 92 - 96 % except from the 90 °aligned film. Majority of resistance come from contact resistance as we discussed in previous chapter.

$$\text{Ratio}[\%] = \frac{(2\text{-terminal resistance} - 4\text{-terminal resistance})}{2\text{-terminal resistance}} \times 100 \quad (5.1)$$

We presume the reason for low ratio from the 90 °aligned film is that 4-terminal resistance may already contain large portions of disconnection between CNTs. Nevertheless, the resistivity of the 90 °aligned film is better than random-direction films. As expected, the aligned direction film shows the best resistivity value, but it is still which

can make higher resistivity about 3 times lower than reference value  $1 \times 10^{-4} \Omega \cdot \text{cm}$  because the film may include some semiconducting dominant SWNTs. Metallic SWNT and the MWNT exhibit similar resistivity values. From this assessment, we conclude that aligned CNT films are crucial for high quality electronic devices.

CNT	SWNT-Metallic	SWNT-Mixed	SWNT-Mixed	MWNT
Direction	Random	Aligned	90 °aligned	Random
Film length	150 - 450 nm	1 mm	1 mm	1 mm
R [ $\Omega$ ] 2-terminal	0.77k $\pm$ 0.42k	4.09k $\pm$ 1.43k	23.7k	154k $\pm$ 24.9k
R [ $\Omega$ ] 4-terminal	(assumed 0.03k)	0.19k $\pm$ 0.06k	5.76k	12.2k $\pm$ 1.44k
Contact R ratio [%]	96.0	95.5	75.7	92.1
Resistivity [ $\Omega \cdot \text{cm}$ ]	$4.48 \times 10^{-1} \pm 2.61 \times 10^{-1}$	$3.37 \times 10^{-3} \pm 1.15 \times 10^{-3}$	$1.04 \times 10^{-2}$	$5.51 \times 10^{-1} \pm 6.52 \times 10^{-2}$

Table 5.1: Resistance and resistivity comparison between CNT films.

### 5.3.5 Resistance with Annealing Effect

We also tested annealing effect whether annealing may improve the contact resistance. For this test, MWNT films are made by LB method and the thickness is about 65 nm by AFM images. The size of MWNT pad is 200  $\mu\text{m}$  by 200  $\mu\text{m}$  in order to define the measurement location. Annealing condition is 500 °C for 1 hour with Ar gas flow in the AJA sputter chamber. Inspired by Barnett *et al.*'s work to report their annealing between 200 - 500 °C helps removing surface contamination on MWNTs [8], we did the annealing at 500 °C and compared resistance values before and after annealing Fig. 5.11. Four different MWNT films are studied in this annealing test, and the overall resistance drops about 75 % after annealing. We think that annealing removes contamination like surfactants so that this affects adhesion between MWNTs consequently improves the overall resistance of films.

Characterization of the CNT films, thickness, surface roughness, resistance, and resistivity, is not only observing the CNT property depending on the types of CNTs but also the initial information of device fabrication. We studied different types of sorted

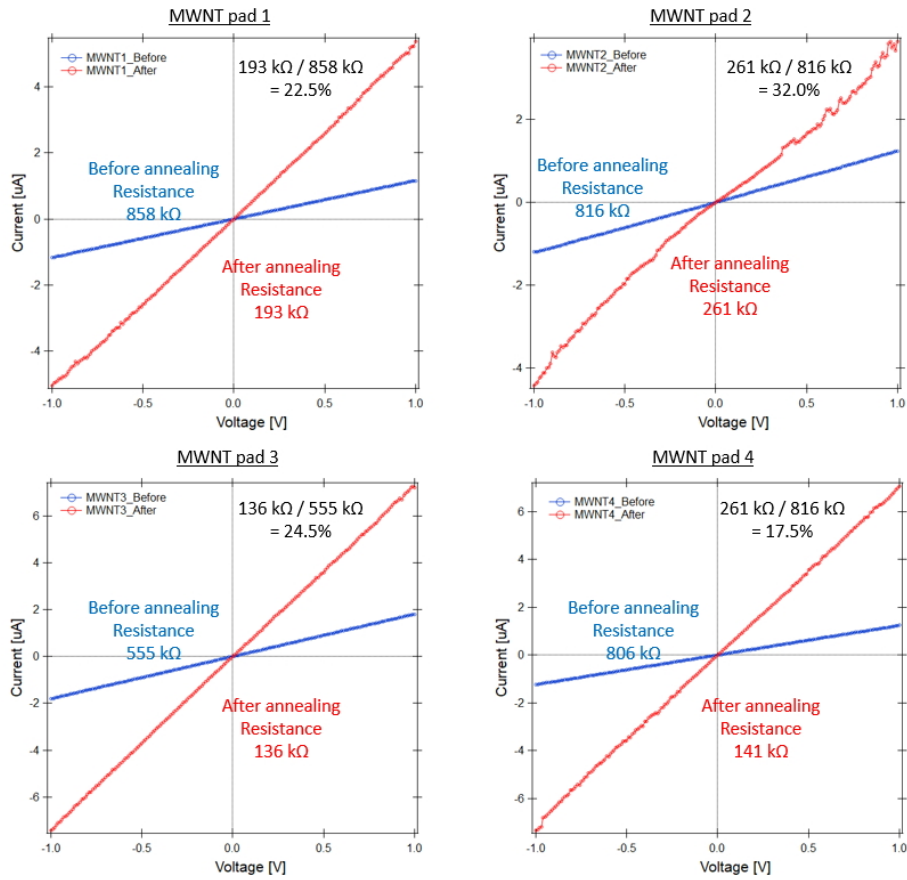


Figure 5.11: Resistance comparison before and after annealing for four different MWNT films.

SWNT films, MWNT films and alignment films. Based on these results, we have fabricated and characterized devices which will be discussed in Chapter 6.

# Chapter 6

## Carbon Nanotube Film Electronics

CNTs have been explored for about three decades as they have attractive electrical, optical, and mechanical properties. Some of those properties are enlisted:

- Electric current density: SWNT ( $\sim 4 \times 10^9$  A/cm<sup>2</sup>) > 1,000 × Cu [38]
- Carrier mobility: SWNT ( $\sim 1 \times 10^4$  cm<sup>2</sup>V<sup>-1</sup>s<sup>-1</sup>) > 10 × Si [97]
- Tensile strength: MWNT ( $\sim 40$  GPa) > 15 × maraging steel [93]
- Young's modulus: SWNT ( $\sim 1.2$  TPa) > 12,000 × rubber [3]
- Thermal conductivity: SWNT ( $\sim 6,600$  Wm<sup>-1</sup>K<sup>-1</sup>) > 17 × Cu [10]
- Various energy band gap in SWNTs: from ultraviolet (UV) (365 nm/3.4 eV) to infrared (IR) (1.6 μm/0.77 eV)

Utilizing the above properties, tremendous applications have recently been demonstrated. Examples of these are thin-film transistors [83], infrared bolometers in both classical and quantum fields [49], bio-sensors [64], single photon source [35], and improved CNT computers [37].

### 6.1 Motivation

My initial goal was to make a Josephson junction with CNT films. A Josephson junction is a basic device used in superconducting quantum computers as a quantum bit

(qubit). A Josephson junction consists of two superconductors sandwiched around an insulator or a normal metal [89]. This structure leads to non-linear behavior. For superconducting qubit, Aluminum (Al) is commonly used due to superb material properties with long coherence length (1600 nm) at a transition temperature of 1.18 K. It also has mature nano-fabrication processes with a high quality insulator, Al oxide [22]. Al superconducting qubits are typically cooled down to below 100 mK in a dilution refrigerator, where GHz qubit operations are implemented. These operations related to the thermal energy  $k_b T$ , where  $k_b$  is Boltzmann constant and  $T$  is temperature, at 100 mK corresponds to 2.1 GHz frequency. However, if THz level operation is equipped, there is a possibility we can operate qubits at higher temperatures (Frequency level at 100 K is about 2.1 THz). Niobium can be a candidate because its critical temperature is 9.25 K. However, the coherence length of niobium is as short as 40 nm at that critical temperature, so the distance between superconductors of the Josephson junction needs to be smaller than 40 nm as well [22]. In this context, CNTs would be a better material because they are ballistic. This could increase the junction distance by prolonging the coherence length, in the length of hundreds of nm even at room temperature [50]. Tianyi Li *et al.* demonstrated a ballistic Josephson junction using graphene and niobium up to a distance of 450 nm [61], so CNTs are anticipated to exhibit similar performance. There were several groups researching CNT and niobium combination Josephson junctions, but all of them used single strand of a CNT to connect across Josephson junction [66, 16, 72], and no film level junction devices have yet been demonstrated.

We have not seen the Josephson effect with CNT films so far, but we have studied low frequency noise (specifically  $1/f$  noise) properties with different kinds of CNT films: semiconducting SWNTs, metallic SWNTs, and MWNTs. Temperature-dependent noise studies will provide crucial information about the qualities of CNT films, which are important for low temperature operation with CNT film devices.

## 6.2 Low Frequency Noise

### 6.2.1 Types of Noises

Understanding noise properties in our measurement data is a fundamental step so as to analyze real signals from devices. If detectors cannot distinguish noise and real signals, we cannot make valid conclusions from our data. This noise can be divided into three regions in frequency domain in Fig.6.1. First is the low frequency noise which can be dominated by  $1/f$  noise or random telegraph noise. The dominant noise sources are

shot noise and thermal noise in the middle frequency range. These noise sources are independent of frequency and called as a white noise. At higher frequencies, quantum noise may start to dominate [60].

Noise can be described by **power spectral density (PSD)** as seen in Fig.6.1. Basically, noise data comes from time sampling measurements of voltage, current, or resistance. These data are measured in time domain, but can be converted to frequency domain as well. Time-sampling data can be converted to the frequency domain by Fourier transform, and if the data are discrete then fast Fourier transform is used. The **PSD** is simply expressed as below,

$$S_x(\omega) = \lim_{T \rightarrow \infty} \frac{2\langle |X_T(i\omega)|^2 \rangle}{T} \quad (6.1)$$

where  $S_x$  is **PSD** and  $x$  is a measurement observable,  $X$  is the Fourier transform of  $x$ ,  $T$  is measurement time, and  $\omega$  is angular frequency ( $\omega = 2\pi f$ ).

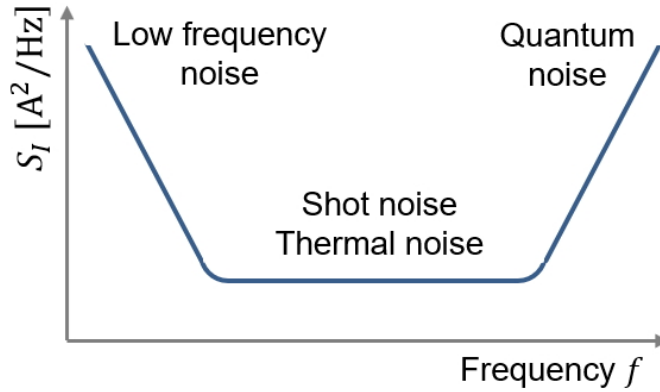


Figure 6.1: Types of noises in a frequency domain [60].

### 6.2.2 $1/f$ Noise and Random Telegraph Noise in Low Frequency Noise

Among noise types, here we are focusing on low frequency noise in terms of two different forms,  $1/f$  noise and a random telegraph noise.  $1/f$  noise has been studied many decades but its origin has not been explained well even though it is ubiquitous in nature. This was studied by F. N. Hooge who found the empirical relation described by Hooge's law as below [39]:

$$\frac{S_I(f)}{I^2} = \frac{S_V(f)}{V^2} = \frac{S_R(f)}{R^2} = \frac{S_G(f)}{G^2} = \frac{A}{f}. \quad (6.2)$$

where  $S_I(f)$ ,  $S_V(f)$ ,  $S_R(f)$ , and  $S_G(f)$  are PSD of current, voltage, resistance, and conductance, respectively and  $A$  is a coefficient from measurements. The so called  $1/f$  noise term comes from the power exponent of frequency  $f$  and typically it is around 1, but it can be between 0.5 and 1.5.

One phenomenological model to explain the  $1/f$  noise is random telegraph noise, which comes from the fact that electrons are captured or emitted in current flow through a channel, explained as generation and recombination noise model. In a two-level system, sampling measurements in time domain yields and a Lorentzian PSD shape written as [39],

$$S_x(f) = \langle(\Delta x^2)\rangle \frac{4\tau}{1 + (2\pi f \tau)^2} \quad (6.3)$$

where  $x$  refers to a measurement parameter: current, voltage, or resistance.  $\Delta x$  is the fluctuation amplitude and  $\tau$  is a characteristic time of the random process.

Researchers have been studying  $1/f$  noise and random telegraph noise with CNTs, both in a wire and a film level. Collins *et al.* first observed the  $1/f$  noise of CNTs in 1-dimensional wires, 2-dimensional films, and 3-dimensional mats [19]. From Eq. (6.2), they found the relation between coefficient  $A$  and  $R$ .

$$S_v(f) = A \frac{V^2}{f^\beta}. \quad (6.4)$$

$$A/R = 10^{-11} \Omega^{-1} \quad (6.5)$$

where the power exponent  $\beta$  is assumed to be 1. However, real measurements gives  $\beta$  to be between 0.96 and 1.12.

Snow *et al.* moved on a further step from the work of Collins *et al.*. They made two-dimensional networks with CNT films, and described their resistance  $R$  in terms of CNT lengths. It makes sense that resistance  $R$  is related to the size of CNT [80] and they found the voltage PSD relation,

$$S_v(f) = 9 \times 10^{-11} \frac{R}{L^{1.3}} \frac{V^2}{f^\beta}, \quad (6.6)$$

$$A/R = 9 \times 10^{-11} / L^{1.3} \Omega^{-1}. \quad (6.7)$$

where  $L$  is a distance between electrodes in unit of  $\mu\text{m}$ .

In case of random telegraph noise, it has been studied as a generation and recombination noise in CNTs arising from the interface between CNTs and dielectric materials.

It might also be observed in charge traps which form at the Schottky barrier between the CNT films and the metal. It has been shown that random telegraph noises are more prominent in semiconducting SWNTs than metallic SWNTs [15]. Similar results are reported that random telegraph noise signals are seen with SWNT film Schottky junctions [4]. There are also studies with metallic and semiconducting SWNT with 1-dimensional level [77]. From this literature, we performed a systematic study of  $1/f$  noise to explore the film level of metallic and semiconducting SWNTs and aligned films with mixed SWNTs.

## 6.3 Device Design

Our device design is simple as shown in Fig.5.9. From a basic Josephson junction, 2-terminal devices are fabricated with various CNT film widths and gaps. Pd and titanium (Ti) are used for inter-layer metallization followed by either Au or niobium (Nb) in order to overcome the contact resistance between CNTs and metals [63]. Design of experiments are summarized:

- CNT film: Semiconducting SWNT film, metallic SWNT film, MWNT film
- Film alignment: Random direction and aligned direction
- Metal: Pd/Au and Ti/Nb
- Width: 10, 20, 30, and 40  $\mu\text{m}$
- Gap between two electrodes: 150 - 450 nm

According to the different combination of SWNT electrical property film orientation and metal choices, we classify four cases:

- Case 1: Metallic SWNT film, Random direction, Pd/Au
- Case 2: Metallic SWNT film, Random direction, Ti/Nb
- Case 3: Semiconducting SWNTs, Random direction, Ti/Nb
- Case 4: Mixed SWNTs, Aligned direction, Pd/Au

## 6.4 Device Fabrication

There are three stages in order to fabricate devices: preparing the device substrates, patterning CNTs, and doing metallization. Depending on the size of the structures, we choose either photolithography or electron-beam lithography followed by evaporation or sputtering for metallization. The final step is liftoff of the rest of metal parts. All fabrication steps have been done in [Quantum-Nano Fabrication and Characterization Facility \(QNFCF\)](#).

### 6.4.1 Preparing Substrates

We perform a two-time lithography: once for the CNT region and once for the metal pads. Metal deposition is done after lithography. Two -step lithography needs alignment so that cross marks are required. The size of the cross is 100  $\mu\text{m}$  long and 3  $\mu\text{m}$  wide width. As this needs its own lithography and metallization steps, this is the starting point of the fabrication. We standardized the substrate design and made a bulk batch of device substrates with cross marks starting from a 4-inch heavily p-doped Si wafer with thermal oxide, 300 nm. The size of each substrate is 1 cm by 1 cm, and total 69 pieces are in a 4 inch wafer cut by dicing saw, model is DAD3240 produced by DISCO. Photolithography is done with a mask-less aligner. Ti adhesion layer of 5 nm and gold of 50 nm are deposited by an e-beam evaporator. Detailed steps and information are given below,

- Step 1: Cleaning a 4 inch wafer
  1. UV-ozone cleaning: 25 °C, 15 minutes (UV-Ozone cleaner by Novascan)
  2. Oxygen plasma asher: [Descum 3 = recipe 6]  
RF power 50 W, pressure 100 mTorr, Temperature 25 °C, O<sub>2</sub> flow 10 sccm, 120 seconds (CV200RFS by Yield Engineering Systems)
  3. Solvent cleaning: Putting the wafer in acetone with bath sonication for 5 minutes, and rinsing it with methanol and IPA
- Step 2: Resist spin coating
  1. Photoresist: S1805 by Microposit
  2. Spinning: at 5,000 rpm for 60 seconds (Twincoater by Reynoldstech)

3. Resist thickness measurement: about 680 nm measured by Filmetric F50
- Step 3: UV exposure, develop, and descum
    1. Maskless aligner (MLA): MLA 150 by Heidelberg - Dose  $65 \text{ mJ/cm}^2$ , digital mirror device (DMD) 600, defocus 0
    2. Develop: MF-319 45 seconds and deionized water (DI) water 60 seconds
    3. Oxygen plasma asher: [Descum 2 = recipe 8]  
RF power 50 W, pressure 100 mTorr, Temperature 25 °C, O<sub>2</sub> flow 10 sccm, 20 seconds (CV200RFS by Yield Engineering Systems)
  - Step 4: Evaporation and liftoff
    1. E-beam evaporation: Ti 5 nm and Au 50 nm (Nanochrome by Intlvac)
    2. Liftoff: Putting in Remover PG which is NMP based solution by MicroChem for minimum an hour and bath sonication for 5 seconds to 10 seconds. Then rinsing with Remover PG and IPA
  - Step 5: Dicing
    1. dicing device chips with 1 cm by 1 cm

## 6.4.2 Preparing Carbon Nanotube Pads

Once transferring the CNT film with a step of CNT film transfer, explained section 4.2.3, on a cross marked substrate, we need to etch the CNT film for forming the proper shape of device pads. As CNT only consists of carbon, it is easily removed by reactive-ion etching (RIE) or oxygen plasma etching. As oxygen plasma etching with CV200RFS by Yield Engineering Systems is relatively easy and takes shorter time compared to RIE etching with Oxford plasmalab system 100 ICP 380, we decided to use oxygen plasma etching. With several recipe tests, we established etching conditions for different applications. For the etching CNT film, we perform the following steps of lithography and etching.

- Spin coating: photoresist S1811, at 5,000 rpm for 60 seconds which thickness is around 1,450 nm
- MLA: dose  $100 \text{ mJ/cm}^2$

- Develop: MF-319 45 seconds and [DI](#) water 60 seconds
- Oxygen plasma asher: Recipe 10 for 150 seconds for [CNT](#) thickness 40 - 80 nm  
RF power 1,000 W, pressure 300 mTorr, Temperature 25 °C, O<sub>2</sub> flow 50 sccm, 150 seconds
- Removing photoresist: Remover PG bath for at least 30 minutes, and rinsing with Remover PG and [IPA](#)

### 6.4.3 Metallization

We deposit metals on devices using two methods depending on the size of patterns and lithography processing time. Devices are fabricated by two lithography methods: one is photolithography which is relatively quick but with a low spatial resolution (minimum feature size 1  $\mu\text{m}$ ). On the other hand, [e-beam lithography \(EBL\)](#) is slow but has much higher spatial resolution. My device design has two patterns: one for the large metal pads to act as probe contacts and the other is for the arm pads between the [CNT](#) and the metal. As the big pads are as large as 200  $\mu\text{m}$ , they do not need high resolution. Therefore, it is efficient to use photolithography. For arm pads, we need a small gap distance on the order of a few hundred nm. Therefore we need to use [EBL](#). In order to maximize the fabrication efficiency, we pattern and perform metallization of the big pads first with photolithography, and then repeat for arm pads using [EBL](#). However, if only fabricating few devices, we can use [EBL](#) for everything and perform metallization once.

- Case 1: metallization of big pads and arm pads separately
  1. Spin coating: S1805 at 5,000 rpm for 60 seconds
  2. [MLA](#): dose 65 mJ/cm<sup>2</sup>
  3. Develop: MF-319 45 seconds and [DI](#) water 60 seconds
  4. Oxygen plasma asher: [Descum 2 = recipe 8]  
RF power 50 W, pressure 100 mTorr, Temperature 25 °C, O<sub>2</sub> flow 10 sccm, 20 seconds (CV200RFS by Yield Engineering Systems)
  5. E-beam evaporation: Ti 5 nm and Au 50 nm
  6. Liftoff: Remover PG bath and rinsing with Remover PG and [IPA](#)

7. Spin coating: PMMA 950K A3 bi-layer at 5,000 rpm for 35 seconds, thickness 210 nm
  8. EBL: accelerating voltage at 25 kV, aperture 10  $\mu\text{m}$ , dose 285  $\mu\text{C}/\text{cm}^2$
  9. Develop: [MIBK:IPA 1:3] 30 seconds and IPA 30 seconds
  10. Deposition of metal : For Pd/Au - e-beam evaporation or for Ti/Nb - sputtering
  11. Liftoff: Remover PG bath and rinsing with Remover PG and IPA
- Case 2: metallization once with two step EBL for big and arm pads
    1. Spin coating: PMMA 950K A3 bi-layer at 5,000 rpm for 35 seconds, thickness 210 nm
    2. EBL:  
For arm pads - accelerating voltage at 25 kV, aperture 10  $\mu\text{m}$  dose, 285  $\mu\text{C}/\text{cm}^2$   
For big pads - accelerating voltage at 10 kV, aperture 60  $\mu\text{m}$  dose, 235  $\mu\text{C}/\text{cm}^2$
    3. Develop: [MIBK:IPA 1:3] 30 seconds and IPA 30 seconds
    4. Deposition of metal : E-beam evaporation for Pd/Au and sputtering for Ti/Nb
    5. Liftoff: Remover PG bath and rinsing with Remover PG and IPA

CNT etching and metallization processes are displayed in Fig.6.2 and Fig.6.3.

## 6.5 Device Characterization

### 6.5.1 Fabrication Results

Microscope images of fabrication results and SEM observation results are presented in Fig.A.1. Fig.A.1(a) captures the overall image of devices in case 1, metal pads are in yellow of Pd/Au, blue colors are metallic SWNT films, and purple regions are SiO<sub>2</sub>/Si substrate. Devices in rows have different width(W) of CNT film, 10  $\mu\text{m}$  to 40  $\mu\text{m}$  from top to bottom, and columns have different gap(G), 150 nm to 450 nm from left to right. The size of metal contact pads are 200  $\mu\text{m}$  by 200  $\mu\text{m}$ . And the size of 200  $\mu\text{m}$  by 200  $\mu\text{m}$  SWNT is dummy SWNT islands for measuring SWNT film resistance directly with probes. One of the devices of width 100  $\mu\text{m}$  and gap 250 nm is zoomed in Fig.A.1(b).

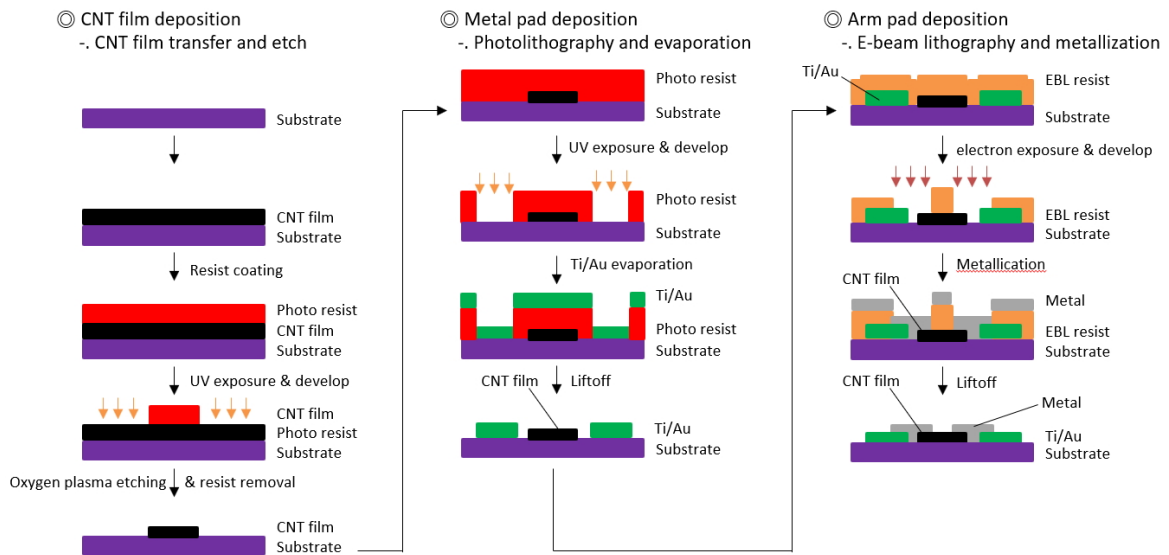


Figure 6.2: Fabrication process - Case 1.

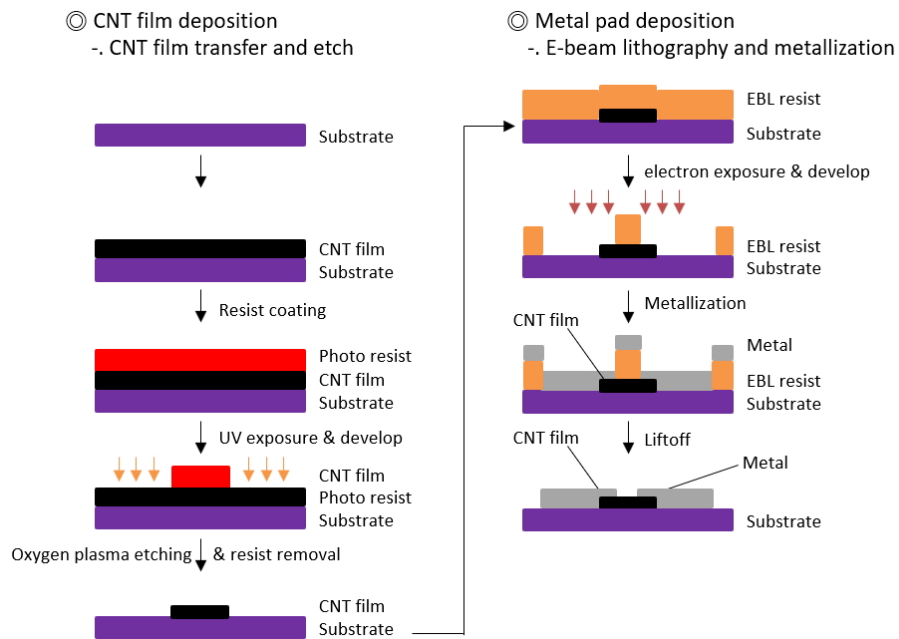


Figure 6.3: Fabrication process - Case 2.

Metal and SWNT film color in Fig.A.1(b) is same as Fig.A.1(a) but substrate color looks brown due to the automatic white balance in microscope. Since the gap is not observed well due to the limited spatial resolution in optical microscope, SEM observation was done and its representative image is in Fig.A.1(c). This observation is gap of the device, gray color up and down side are metal and black between two is SWNTs. The real measurement of gap is 280 nm which is 30 nm larger than the design value of 250 nm.

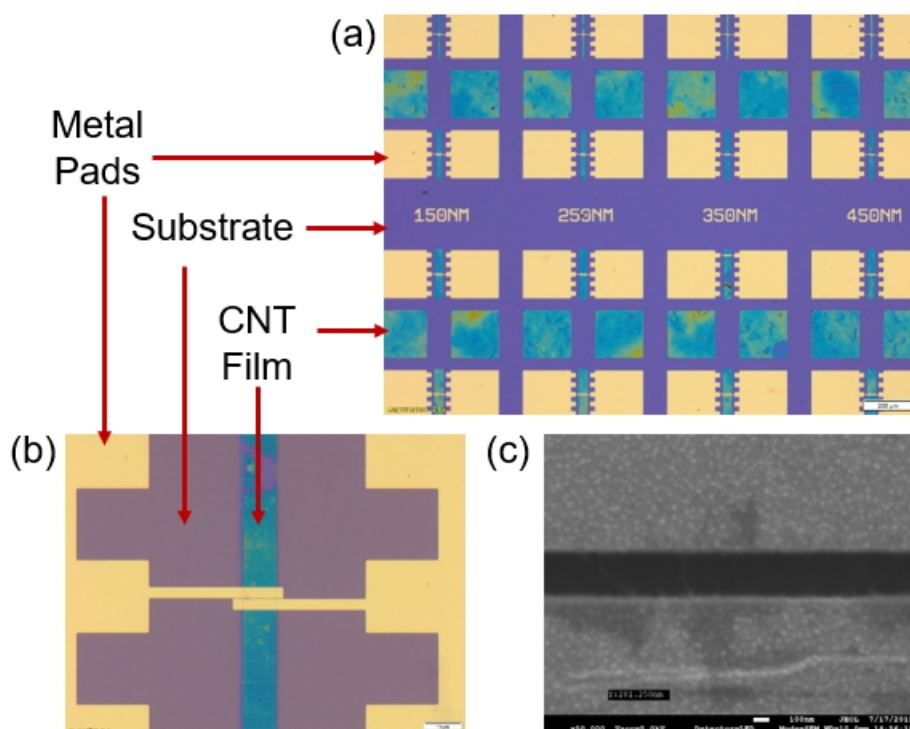


Figure 6.4: (a) The microscope image of overall fabricated devices. Scale bar is 200  $\mu\text{m}$  (b) Zoomed in view of microscope image for the device width 10  $\mu\text{m}$  and gap 250 nm. Scale bar is 10  $\mu\text{m}$ . (c) SEM image of observation of gap for the device whose design values are width 10  $\mu\text{m}$  and gap 250 nm. Scale bar is 100 nm.

## 6.5.2 I-V Characteristics

We measure I-V characteristics at both room temperature and low temperature and the results are presented in Fig.6.5. Except case 3, three samples have linear I-V relations at room temperature. However, they become non-linear as the temperature goes

down. In particular, case 3 looks worst because its resistance goes above 2.5 M $\Omega$  even though the sweep voltage is 1 V which is 5 $\times$  or 10 $\times$  larger than other sweep conditions and temperature is around 50 K which is higher than others. Low temperature resistances increase more than 20 times than room temperature resistances except case 4. We presume that contact between CNT film and metal is a key point of the resistance changes: becoming higher resistance at low temperature or being non-linear I-V relation come from Schottky contact. The combination of aligned SWNT film and Pd/Au show the best result in our experiments.

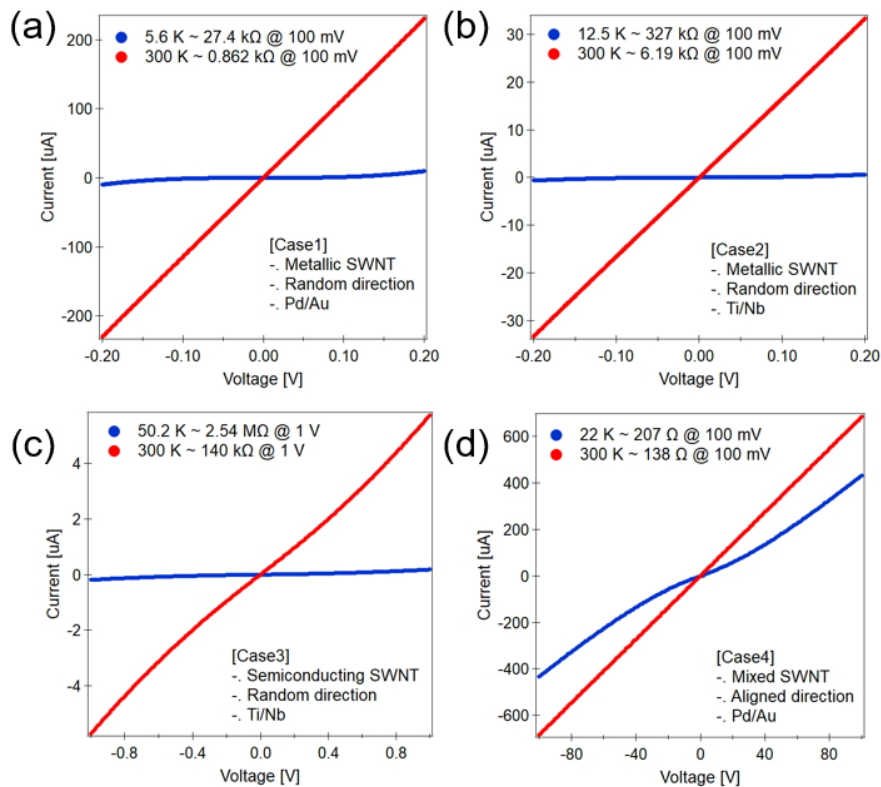


Figure 6.5: I-V measurement results for four cases at room temperature and low temperature. All the measurements are voltage sweep results. (a) Results for case 1. Voltage range is -200 mV to 200 mV, interval 1 mV. (b) Results for case 2. Voltage range is -200 mV to 200 mV, interval 1 mV. (c) Results for case 3. Voltage range is -1 V to 1 V, interval 1 mV. (d) Results for case 4. Voltage range is -100 mV to 100 mV, interval 1 mV.

### 6.5.3 Temperature-Dependent Resistance

Temperature-dependent resistance measurements are done to determine contact types: ohmic or Schottky contact. Unfortunately, all four cases show Schottky contact that relative resistances increase as temperature decreases in Fig.6.6. Relative resistance in case 1 dramatically increases as temperature goes down. An interesting observation is that the shape of curve appears to be common depending on the metal. Case 1 and case 4, both Pd/Au, both seem to have an exponential trend, whereas case 2 and case 3, which are both Ti/Nb appears to have a logarithmic trend. In addition, Pd/Au cases show that relative resistance begins to increase around 90 Kelvin. On the other hand, the relative resistance of Ti/Nb devices gradually increases through the temperature range.

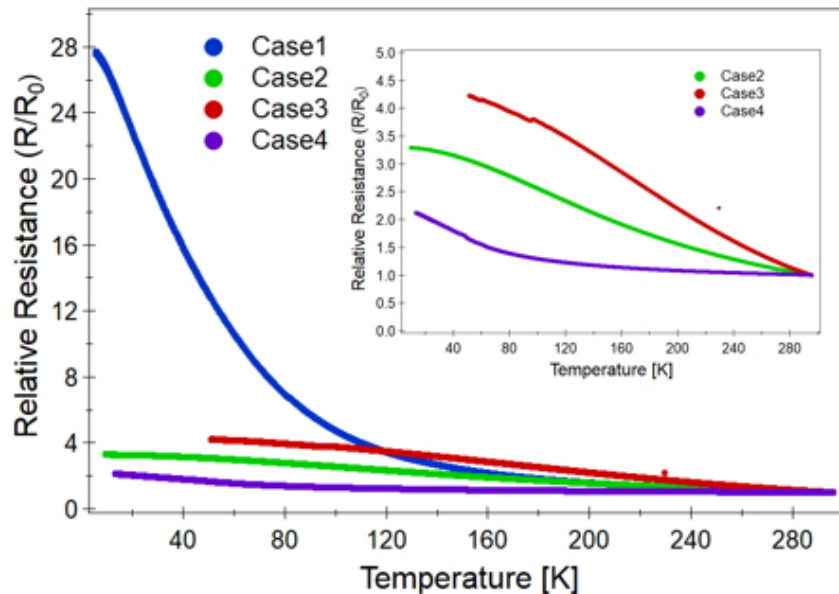


Figure 6.6: Temperature-dependent resistance measurements results. Four cases results are normalized by room temperature resistance and represents as a function of temperature. Inset reprinted plot removing case 1 in order to adjust range of y-axis.

### 6.5.4 Low Frequency Noise

We measure fluctuating current signals in time domain under the a voltage bias. Voltage bias points are determined from the two-terminal I-V sweep results. There are

three different regions in the I-V characteristics: a non-linear region, a linear region, and a transition region between the non-linear and the linear regions. Sampling times are 5 ms and 20 ms. Visualization and analysis of the sampling data by using a low-frequency noise spectrum analysis program built in Python [29]. This program uses Welch’s method which is an advanced algorithm to estimate the PSD from the time-domain signal. We have also compared Welch’s method to two other methods, one using periodogram and the other FFT. While the results are similar, Welch’s method can smoothen the estimated PSD, so it is more suitable to analyze low frequency data systematically. Fig.6.7 shows the window of results to calculate low frequency data. Fig.6.7(a) shows the sampling results where x-axis is in time and y-axis is in current. Fig.6.7(b) is the histogram of sample data which can observe whether it has two-level systems or not, intuitively. Fig.6.7(c) is the calculate PSD data which is in green with fitting curves, the orange is a  $1/f$  curve, and the blue one is a Lorentzian curve. According to these plots, we can distinguish  $1/f$  from random telegraph noise quickly. And then collecting the results from different measurement condition, we can interpret the data and draw conclusions.

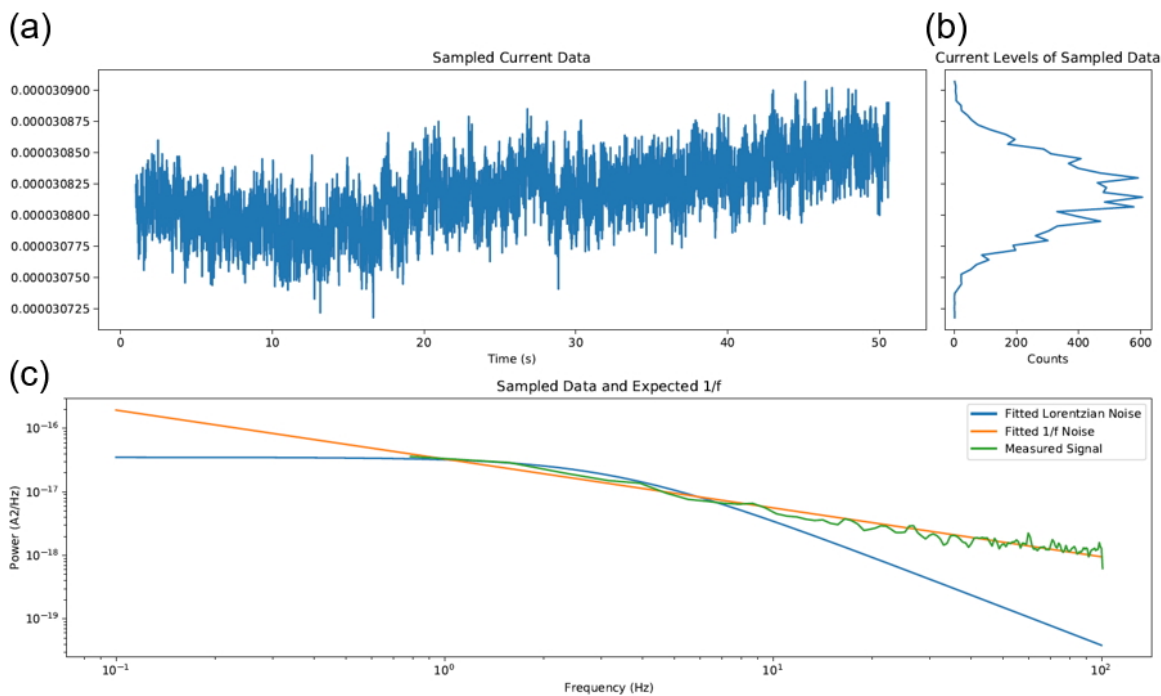


Figure 6.7: Graphical user interface of low frequency analysis coding python [29].

Fig.6.8 collects the PSD data for four cases with temperature dependence. Basically,  $S_I$  values are temperature-dependent because the current flow is related to the temperature. From the temperature-dependent resistance data, resistance goes up as temperature goes down. From this reason, PSD in low temperature are located in lower position compared to PSD from high temperature. All the measurements shows a  $1/f$  noise trend and the details of data analysis with coefficients will be addressed in the discussion section. We observe artificial spikes the cause of around 60 Hz which may come from the electronic clock frequency, but we do not understand the other spikes especially many spikes observed in case 3 and case 4. In Fig.6.8(d), 300 K PSD graph is lower than the 150 K PSD one. This is the reason that resistances between two are similar. We can observe this results in temperature-dependent resistance data. However, we need to study the reason why there are many spikes observed between 10 Hz and 100 Hz region.

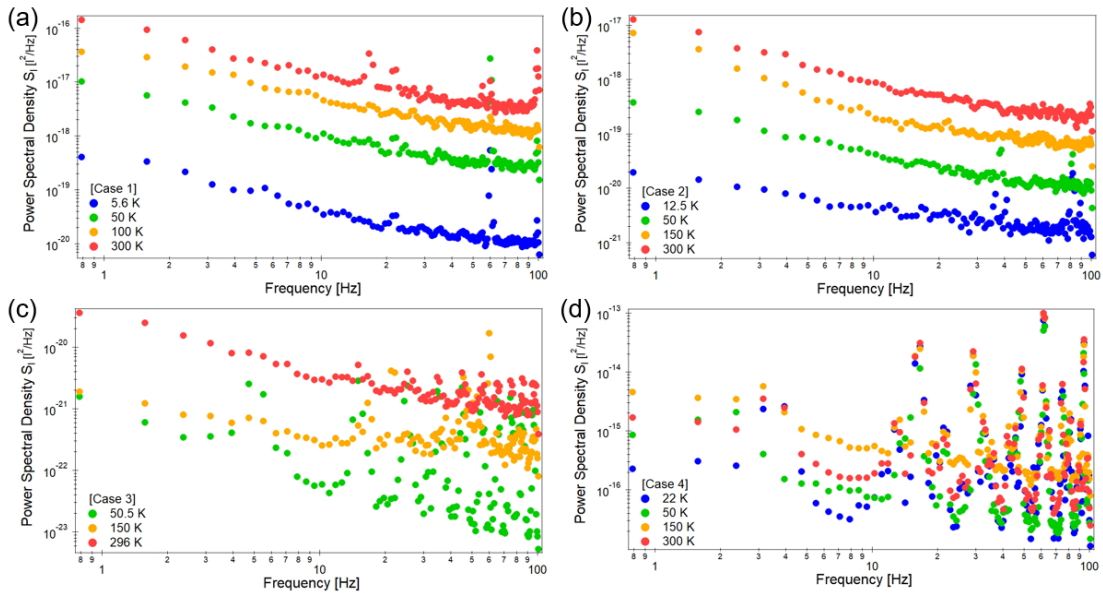


Figure 6.8: PSD data of each case with different temperatures.

## 6.6 Discussions

Behnam *et al.* demonstrated resistivity data as a function of temperature and interpret within [variable-range hopping \(VRH\)](#) and [fluctuation-induced tunneling \(FIT\)](#)

with the behavior contexts [9]. In Fig.6.9(a), the log-log plots of temperature-dependent resistivity data are fit by VRH below 40 K and FIT above 40 K [9]. Those two may come from the different transport where electrons are located. It is reasonable to think that electrons can hop between SWNTs at low temperatures, because they will contract leaving gaps between them at that temperature. On the other hand, tunneling through the Schottky barrier can be more dominant at higher temperature where SWNTs will not contract. Compared to this result, our data do not follow their observation. In order to match the plot shape, we plot the data in log-log scale, but the resistance saturates as temperature decreases in Fig.6.9(b). Note that while their y-axis is resistivity and our y-axis is relative resistivity, the shapes can be compared. According to their explanation, quality of our SWNTs is better than theirs under certain temperature, because the hopping process is not observed below 40 K due to better resistance. Inset of Fig.6.9(b) shows the full range of temperature, in that Ti/Nb metal devices exhibit early saturated shape from higher temperature to lower temperature. We presume that because the contact between SWNT and Ti is worse than that between SWNT and Pd, resistance increases quickly when it cool down. Resistance of the semiconducting film is higher than that of the metallic film which is expected because the contact barrier of semiconducting film is higher than metallic's. Aligned film with mixed SWNTs which assumed to have 2/3 semiconducting and 1/3 metallic, SWNTs shows the lowest resistance increasing ratio. This means that alignment is a dominant factor for the overall resistance, which is also seen in resistivity comparison in Table 5.1.

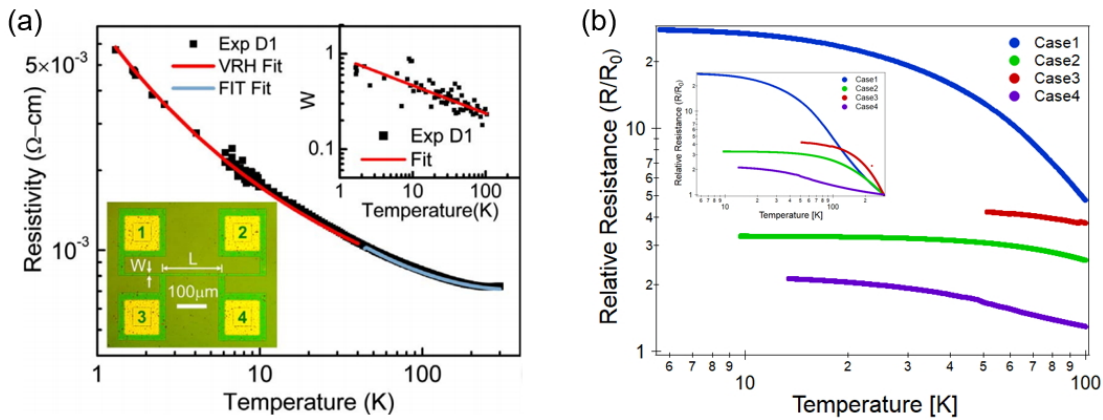


Figure 6.9: (a) Log-log plot of temperature-dependent resistivity from SWNT film fitting with VRH and FIT. (Reprinted with permission from reference [9]. Copyright 2010 American Physical Society.) (b) Log-log plot of temperature-dependent relative resistance from our device results.

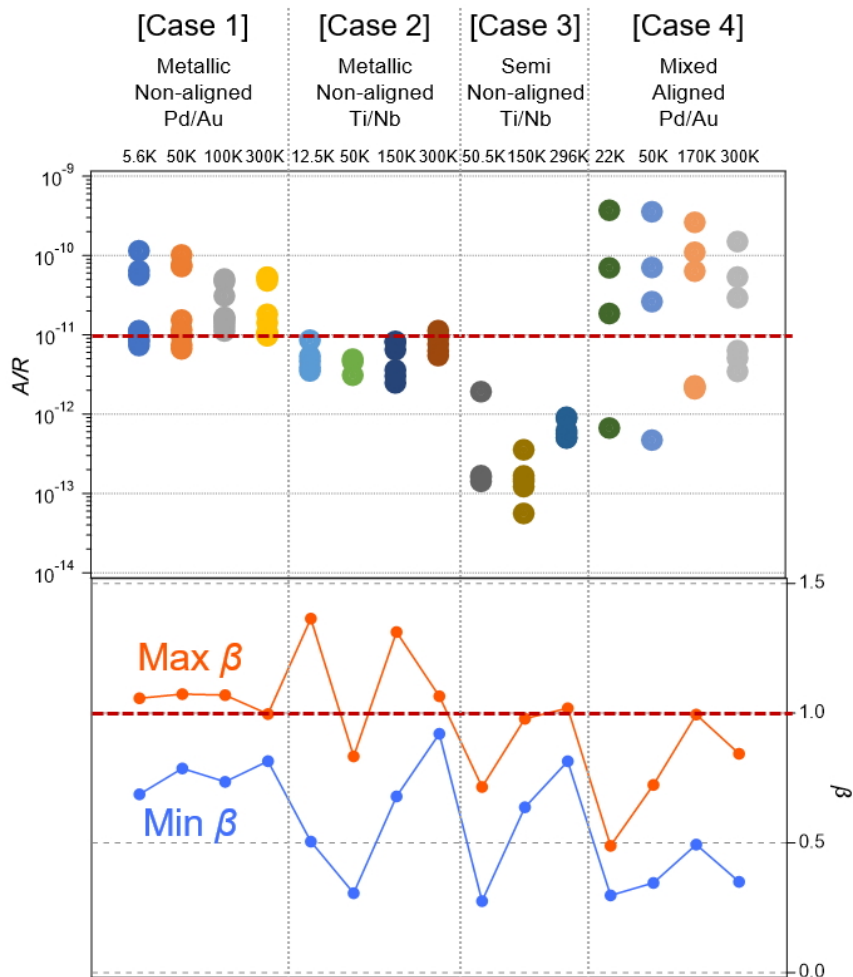


Figure 6.10:  $1/f$  noise coefficient,  $A/R$  and  $\beta$  comparison between cases.

When we evaluated  $1/f$  the noise coefficients  $A$  and  $\beta$  in Fig. 6.10, we conclude some differences between designs. We also extract  $A/R$ , which is expected to be constant  $10^{-11}$ , and  $\beta$  which is expected to be 1 [19]. In order to compare their data and see what trends are in, we set in  $A/R$  and  $\beta$  the minimum and maximum values to show the variation in a plot. We expected the case 4, aligned film with Pd/Au, has lower resistance and good contact from temperature-dependent resistance result. However, case 1 follows similar to the reference results without temperature dependent. Case 4 also shows larger variation within PSD in samples data and lower  $\beta$  values. For the Pd/Au devices in case 1 and case 4,  $A/R$  values are close to the reference value  $10^{-11}$

even though there are unusual data points. In case of Ti/Nb devices, case 2 and Case 3,  $A/R$  values are smaller than Pd/Au cases. Especially, case 3 shows lowest  $A/R$  values. This can be interpreted that resistance here is lower than others given the same  $A$  value. Semiconducting property of SWNT and contact barrier between Ti and SWNT is worse than others. As we can adjust Fermi level by applying gate voltage, we may observe  $A/R$  value differences at different gate voltages which we will explore in future. Overall, we observe  $1/f$  noise behavior with respect to  $A/R$  values in terms of metallic and semiconducting SWNTs, Pd/Au and Ti/Nb, and film alignments. We need to study further for aligned film with Pd/Au, case 4, as it shows best resistance property, but it does not follow reference results.

# Chapter 7

## Conclusion

### 7.1 Summary

We have demonstrated sorting of SWNTs, making films, and fabricating devices, using raw CNTs from commercial vendors. We have studied unique and outstanding properties of CNTs and their use in various applications as well. For sorting, ATPE generates simple and well-separated results. In order to calculate the purity of SWNT in terms of the mean percentage of metallic and semiconducting SWNTs, we have learned background extraction in absorbance spectrum, and made an analysis algorithm to obtain purity of SWNTs in a solution. From the ATPE process, we have a sorted 100 % semiconducting SWNT solution in our analysis algorithm. Then, we make CNT films with a vacuum filtration method which makes uniform films. In addition, electronic devices with CNT films are crucial with good contacts. In that case, between CNTs junctions should be clean as much as possible. In order to do that, polymer exchange process after ATPE is required and washing process during vacuum filtration is essential. Making our own transferring recipe, we are easily prepare and deposit films on substrates wherever and whenever we want. This process overcomes the preparation of CNT films on substrates without time and place limitation.

Characterizing different CNT films, we have learned the alignment of CNT film is crucial for high performance CNT electronic devices. Finally, we are able to measure devices with our devices fabricated in QNFCF our own devices. Although our initial goal for devices was to make Josephson junction and we are still working to achieve this goal, we are able to observe low frequency noise with respect to different SWNT film properties, metallic and semiconducting, different metal materials, Pd/Au and Ti/Nb,

and aligned film. By comparing  $1/f$  noise coefficients,  $A/R$ , we have observed different metal material gives their unique results.

## 7.2 Future Work

In this last section, I like to consider future stages. First, the [ATPE](#) process needs standard recipe with electronic pipettes. Using electronic pipettes, we are able to set a standard recipe regardless of people who are doing [ATPE](#). And then we can set recipes for sorting pure [SWNT](#) chirality. In this recipe, we need to do with different synthesizing [SWNTs](#) as those have different diameters. We plan to automate this process by python codes.

Next is film alignment with vacuum filtration method. We observed aligning films are truly beneficial to electronic devices. Therefore, this task is one of the urgent work. Last is to observe Josephson effect in a [CNT](#) film Josephson junction. While we study superconductivity and ballistic properties with vacuum filtration, we will improve fabricating skills in order to make good contacts. Because [CNT](#) films are a 2-dimension structure coming from combination of 1-dimension, we believe [CNT](#) films can be novel structure to explore fundamental physical phenomena like superconducting properties.

# References

- [1] "Aqueous Two-Phase System (ATPS): An Overview and Advances in Its Applications". *Biological Procedures Online*, 18(18), (2016).
- [2] Advice about VF film transfer method from Natsumi Komatsu.
- [3] P. M. Ajayan, L. S. Schadler, C. Giannaris, and A. Rubio. "Single-Walled Carbon Nanotube-Polymer Composites: Strength and Weakness". *Advanced Materials*, 12(10):750–753, (2000).
- [4] Yanbin An, Hemant Rao, Gijs Bosman, and Ant Ural. "Random Telegraph Signal and 1/f noise in Forward-Biased Single-Walled Carbon Nanotube Film-Silicon Schottky Junctions". *Applied Physics Letters*, 100:213102, (2012).
- [5] Michael S. Arnold, Samuel I. Stupp, and Mark C. Hersam. "Enrichment of Single-Walled Carbon Nanotubes by Diameter in Density Gradients". *Nano Letters*, 5(4):713–718, (2005).
- [6] Hiroki Ashiba, Yoko Iizumi, Toshiya Okazaki, Xiaomin Wang, and Makoto Fujimaki. "Carbon Nanotubes as Fluorescent Labels for Surface Plasmon Resonance-Assisted Fluoroimmunoassay". *Sensors*, 17(11), (2017).
- [7] Ehsan Atefi, Darcy Fyffe, Kerim B. Kaylan, and Hossein Tavana. "Characterization of Aqueous Two-Phase Systems from Volume and Density Measurements". *Journal of Chemical Engineering Data*, 61(4):1531–1539, (2016).
- [8] Chris J. Barnett, Cathren E. Gowenlock, Kathryn Welsby, Alvin Orbaek White, and Andrew R. Barron. "Spatial and Contamination-Dependent Electrical Properties of Carbon Nanotubes". *Nano Letters*, 18(2):695–700, (2018).

- [9] Ashkan Behnam, Amlan Biswas, Gijs Bosman, and Ant Ural. "Temperature-Dependent Transport and  $1/f$  Noise Mechanisms in Single-Walled Carbon Nanotube Films". *Physical Review B*, 81:125407, (2010).
- [10] Savas Berber, Young-Kyun Kwon, and David Tománek. "Unusually High Thermal Conductivity of Carbon Nanotubes". *Physical Review Letters*, 84(20):4613–4616, (2000).
- [11] D. S. Bethune, C. H. Klang, M. S. de Vries, G. Goman, R. Savoy, J. Vazquez, and R. Beyers. "Cobalt-Catalysed Growth of Carbon Nanotubes with Single-Atomic-Layer Walls". *Nature*, 363:605–607, (1993).
- [12] Adam J. Blanch, Claire E. Lenehan, and Jamie S. Quinton. "Optimizing Surfactant Concentrations for Dispersion of Single-Walled Carbon Nanotubes In Aqueous Solution". *The Journal of Physical Chemistry B*, 114(30):9805–9811, (2010).
- [13] C. J. Bradley and A. P. Cracknell. *The Mathematical Theory of Symmetry in Solids: Representation theory for point groups and space groups*. Clarendon Press · Oxford, 1972.
- [14] Michael J. Bronikowski, Peter A. Willis, Daniel T. Colbert, K. A. Smith, and Richard E. Smalley. "Gas-Phase Production of Carbon Single-Walled Nanotubes from Carbon Monoxide via the HiPco Process: A Parametric Study". *Journal of Vacuum Science Technology A*, 19(4):1800–1805, (2001).
- [15] Hyun-Jong Chung, Tae Woo Hjm, Sung Won Kim, Young Gyu You Sang Wook Lee, Sung Ho Jhang, Eleanor E. B. Campbell, and Yung Woo Park. "Random Telegraph Noise in Metallic Single-Walled Carbon Nanotubes". *Applied Physics Letters*, 104:193102, (2014).
- [16] J. P. Cleuziou, W. Wernsdorfer, V. Bouchiat, T. Ondarcuhu, and M. Monthieux. "Carbon Nanotube Superconducting Quantum Interference Device". *Nature Nanotechnology*, 1:53–59, (2006).
- [17] Python code by Marko Pejic with HeeBong Yang and Prof. Na Young Kim.
- [18] Collected and summarized Jeffrey A. Fagan's ATPE recipe.
- [19] Philip G. Collins, M. S. Fuhrer, and A. Zetti. " $1/f$  Noise in Carbon nanotubes". *Applied Physics Letters*, 76(7):894–896, (2000).

- [20] Rasel Das, Zohreh Shahnava, MD. Eaqub Ali, Mohammed Moinul Islam, and Sharifah Bee Abd Hamid. "Can We Optimize Arc Discharge and Laser Ablation for Well-Controlled Carbon Nanotube Synthesis". *Nanoscale Research Letters*, 11(510), (2016).
- [21] Phase diagram experiments done by Marko Pejic and HeeBong Yang.
- [22] R. J. Donnelly. *Physics Vade Mecum*, chapter 'Cryogenics'. American Institute of Physics, New York, 1981.
- [23] M. S. Dresselhaus, G. Dresselhaus, R. Saito, and A. Jorio. "Raman Spectroscopy of Carbon Nanotubes". *Physics Reports*, 409:47–99, (2005).
- [24] E. Einarsson and S. Maruyama. *Synthesis of Carbon Nanotubes and Graphene for Photonic Applications*, chapter 2. Woodhead Publishing Limited, 2013.
- [25] Jeffrey A. Fagan. "Aqueous Two-Polymer Phase Extraction of Single-Wall Carbon Nanotubes Using Surfactants". *Nanoscale Advances*, 1:3307–3324, (2019).
- [26] Jeffrey A. Fagan, Erik H. Hároz, Rachelle Ihly, Hui Gui, Jeffrey L. Blackhurn, Jeffrey R. Simpson, Stephanie Lam, Angela R. Hight Walker, Stephene K. Doorn, and Ming Zheng. "Isolation of > 1 nm Diameter Single-Wall Carbon Nanotube Species Using Aqueous Two-Phase Extraction". *ACS Nano*, 9(5):5377–5390, (2015).
- [27] Jeffrey A. Fagan, Constantine Y. Khripin, Carlos A. Silvera Batista, Jeffrey R. Simpson, Erik H. Hároz, Angela R. Hight Walker, and Ming Zheng. "Isolation of Specific Small-Diameter Single-Wall Carbon Nanotube Species via Aqueous Two-Phase Extraction". *Advanced Materials*, 26:2800–2804, (2014).
- [28] A. G. Souza Filho, A. Jorio, Ge. G. Samsonidze, G. Dresselhaus, M. A. Pimenta, M. S. Dresselhaus, Anna K. Swan, M. S. Unlu, B. B. Goldberg, and R. Saito. "Competing Spring Constant versus Double Resonance Effects on the Properties of Dispersive Modes in Isolated Single-Wall Carbon Nanotubes". *Physical Review B*, 67(035427), (2003).
- [29] Low frequency noise analysis python program coding by Alan Malcolm.
- [30] Weilu Gao and Junichiro Kono. "Science and Applications of Wafer-Scale Crystalline Carbon Nanotube Films Prepared through Controlled Vacuum Filtration". *Royal Society Open Science*, 6:181605, (2019).

- [31] Saunab Ghosh, Sergei M. Bachilo, and R. Bruce Weisman. "Advanced Sorting of Single-Walled Carbon Nanotubes by Nonlinear Density-Gradient Ultracentrifugation". *Nature Nanotechnology*, 5:443–450, (2010).
- [32] António Lima Grilo, M. Raquel Aires-Barros, and Ana M. Azevedo. "Partitioning in Aqueous Two-Phase Systems: Fundamentals, Applications and Trends". *Separation Purification Reviews*, 45:68–80, (2016).
- [33] Hui Gui, Jason K. Streit, Jeffrey A. Fagan, Angela R. Hight Walker, Chongwu Zhou, and Ming Zheng. "Redox Sorting of Carbon Nanotubes". *Nano Letters*, 15(3):1642–1646, (2015).
- [34] T. Guo, P. Nikolaev, A. Thess, D. T. Colbert, and R. E. Smalley. "Catalytic Growth of Single-Walled Nanotubes by Laser Vaporization". *Chemical Physics Letters*, 243:49–54, (1995).
- [35] X. He, H. Htoon, S. K. Doorn, W. H. P. Pernice, F. Pyatkov, R. Krupke, A. Jeantet, Y. Chassagneux, and C. Voisin. "Carbon Nanotubes as Emerging Quantum-Light Sources". *Nature Materials*, 17:663–670, (2018).
- [36] Xiaowei He, Weilu Gao, Lijuan Xie, Bo Li, Qi Zhang, Sidong Lei, John M. Robinson, Erik H. Hároz, Stephen K. Doorn, Weipeng Wang, Robert Vajtai, Pulickel M. Ajayan, W. Wade Adams, Robert H. Hauge, and Junichiro Kono. "Wafer-Scale Monodomain Films of Spontaneously Aligned Single-Walled Carbon Nanotubes". *Nature Nanotechnology*, 11:633–639, (2016).
- [37] Gage Hills, Christian Lau, Andrew Wright, Samuel Fuller, Mindy D. Bishop, Tathagata Srimani, Pritpal Kanhaiya, Rebecca Ho, Aya Amer, Yosi Stein, Denis Murphy, Arvind, Anantha Chandrakasan, and Max M. Shulaker. "Modern Microprocessor Built from Complementary Carbon Nanotube Transistor". *Nature*, 572:595–602, (2019).
- [38] Seunghun Hong and Sung Myung. "A Flexible Approach to Mobility". *Nature Nanotechnology*, 2:207–208, (2007).
- [39] F. N. Hooge, T. G. M. Kleinpenning, and L. K. J. Vandamme. "Experimental Studies on  $1/f$  Noise". *Reports on Progress in Physics*, 44(5):479–532, (1981).
- [40] Liangbing Hu, David S. Hecht, and George Gruner. "Carbon Nanotube Thin Films: Fabrication, Properties, and Applications.". *Chemical Reviews*, 110:5790–5844, (2010).

- [41] Harald Ibach and Hans Lüth. *Solid-State Physics: An Introduction to Principles of Materials Science*. Fourth Extensively Updated and Enlarged Edition. Springer, 2009.
- [42] Sumio Iijima. "Helical microtubules of graphitic carbon". *Nature*, 354:56–58, (1991).
- [43] Sumio Iijima and Toshinari Ichihashi. "Single-Shell carbon nanotubes of 1-nm diameter". *Nature*, 363:603–605, (1993).
- [44] NanoIntegris Inc. "Specification of Purified SWNTs by HiPCO", <https://nanointegris.com/our-products/small-diameter-swnts-hipco/>.
- [45] Sigma-Aldrich Inc. "Specification of MWNT", <https://www.sigmaaldrich.com/catalog/product/aldrich/698849?lang=en&region=CA>.
- [46] Sigma-Aldrich Inc. "Specification of SG65i", <https://www.sigmaaldrich.com/catalog/product/aldrich/773735?lang=en&region=CA>.
- [47] Sigma-Aldrich Inc. "Specification of SG76", <https://www.sigmaaldrich.com/catalog/product/aldrich/704121?lang=en&region=CA>.
- [48] Sigma-Aldrich Inc. "Specification of SWNT", <https://www.sigmaaldrich.com/catalog/product/aldrich/704113?lang=en&region=CA>.
- [49] Mikhail E. Itkis, Ferenc Borondics, Aiping Yu, and Robert C. Haddon. "Bolometric Infrared Photoresponse of Suspended Single-Walled Carbon Nanotube Films". *Science*, 312(5772):413–416, (2006).
- [50] Ali Javey, Jing Guo, Qian Wang, Mark Lundstrom, and Hongjie Dai. "Ballistic Carbon Nanotube Field-Effect Transistors". *Nature*, 424:654–657, (2003).
- [51] A. Jorio, A. G. Souza Filho, G. Dresselhaus, M. S. Dresselhaus, A. K. Swan, M. S. Unlu, B. B. Goldberg, M. A. Pimenta, J. H. Hafner, C. M. Lieber, and R. Saito. "G-Band Resonant Raman Study of 62 Isolated Single-Wall Carbon Nanotubes". *Physical Review B*, 65(155412), (2002).

- [52] A. Jorio, R. Saito, J. H. Hafner, C. M. Lieber, M. Hunter, T. McClure, G. Dresselhaus, and M. S. Dresselhaus. "Structural (n,m) Determination of Isolated Single-Wall Carbon Nanotubes by Resonant Raman Scattering". *Physical Review Letters*, 86(6):1118–1121, (2001).
- [53] C. Journet, W. K. Maser, P. Bernier, A. Loiseau, M. Lamy de la Chapelle, S. Lefrant, P. Deniard, R. Lee, and J. E. Fischer. "Large-scale Production of Single-Walled Carbon Nanotubes by the Electric-Arc Technique". *Nature*, 388:756–758, (1997).
- [54] H. Kataura, Y. Kymazawa, Y. Maniwa, I. Umezu, S. Suzuki, Y. Ohtsuka, and Y. Achiba. "Optical Properties of Single-Wall Carbon Nanotubes". *Synthetic Metals*, 103:2555–2558, (1999).
- [55] I. Kazani, G. De Mey, C. Hertleer, J. Banaszczyk, A. Schwarz, G. Guxho, and L. Van Langenhove. "About the collinear Four-Point Probe Techniques Inability to Measure the Resistivity of Anisotropic Electroconductive Fabrics". *Textile Research Journal*, 83(15):1587–1593, (2013).
- [56] Per-Åke Albertsson. "Partition of Cell Particles and Macromolecules in Polymer Two-Phase Systems". *Advances in Protein Chemistry*, 24:309–341, (1970).
- [57] Munawar Khalil, Badrul Mohamed Jan, Chong Wen Tong, and Mohammed Ali Berawi. "Advanced Nanomaterials in Oil and Gas Industry: Design, Application and Challenges". *Applied Energy*, 191(1):287–310, (2017).
- [58] Y. Khripin, Jeffrey A. Fagan, and Ming Zheng. "Spontaneous Partition of Carbon Nanotubes in Polymer-Modified Aqueous Phases". *Journal of the American Chemical Society*, 135(18):6822–6825, (2013).
- [59] H. W. Kroto, J. R. Heath, S. C. O'Brien, R. F. Curl, and R. E. Smalley. " $C_{60}$  : Buckminsterfullerene". *Nature*, 318 : 162 – 163, (1985).
- [60] Prof. Na Young Kim. Lecture note: Introduction to noise process, 2018 Spring.
- [61] Tianyi Li, John Gallop, Ling Hao, and Edward Romans. "Ballistic Josephson Junctions based on CVD graphene". *Superconductor Science and Technology*, 31(4):045004, (2018).
- [62] W. Z. Li, S. S. Xie, L. X. Qian, B. H. Chang, B. S. Zou, W. Y. Zhou, R. A. Zhao, and G. Wang. "Large-Scale Synthesis of Aligned Carbon Nanotubes". *Science*, 274(5293):1701–1703, (1996).

- [63] Seong Chu Lim, Jin Ho Jang, Dong Jae Bae, Gang Hee Han, Sunwoo Lee, In-Seok Yeo, and Young Hee Lee. "Contact Resistance Between metal and Carbon Nanotube Interconnects: Effect of Work Function and Wettability". *Applied Physics Letters*, 95:264103, (2009).
- [64] Merum, Sireesha, Veluru, Jagadeesh Babu, Seeram, and Ramakrishna. "Functionalized Carbon Nanotubes in Bio-World: Applications, Limitations and Future Directions". *Materials Science and Engineering: B*, 223:43–63, (2017).
- [65] Gordon E. Moore. "Cramming More Components onto Integrated Circuits". *Electronics*, 38(8):114–117, (1965).
- [66] A. F. Morpurgo, J. Kong, C. M. Marcus, and H. Dai. "Gate-Controlled Superconducting Proximity Effect in Carbon Nanotubes". *Science*, 286(5438):263–265, (1999).
- [67] Computer History Museum. 1960: Metal oxide semiconductor (mos) transistor demonstrated, <https://www.computerhistory.org/siliconengine/metal-oxide-semiconductor-mos-transistor-demonstrated/>.
- [68] Anton V. Naumov, Saunab Ghosh, Dmitri A. Tsyboulski, Sergei M. Bachilo, and R. Bruce Weisman. "Analyzing Absorption Backgrounds in Single-Walled Carbon Nanotube Spectra". *ACS Nano*, 5(3):1639–1648, (2011).
- [69] Pavel Nikolaev, Michael J. Bronikowski, R. Kelley Bradley, Frank Rohmund, Daniel T. Colbert, K. A. Smith, and Richard E. Smalley. "Gas-Phase Catalytic Growth of Single-Walled Carbon Nanotubes from Carbon Monoxide". *Chemical Physics Letters*, 313:91–97, (1999).
- [70] Adrian Nish, Jeong-Yuan Hwang, James Doig, and Robin J. Nicholas. "High Selective Dispersion of Single-Walled Carbon Nanotubes Using Aromatic Polymers". *Nature Nanotechnology*, 2:640–646, (2007).
- [71] A. Oberlin, M. Endo, and T. Koyama. "Filamentous Growth of Carbon through Benzene Decomposition". *Journal of Crystal Growth*, 32:335–349, (1976).
- [72] E. Pallecchi, M. Gaaß, D. A. Ryndyk, and Ch. Strunk. "Carbon Nanotube Josephson Junctions with Nb Contact". *Applied Physics Letters*, 93(7):072501, (2008).
- [73] L. Pincherle. "Band structure calculations in solids". *Reports on Progress in Physics*, 23:355–394, (1960).

- [74] Jan Prasek, Jana Drbohlavova, Jana Chomoucka, Jaromir Hubalek, Ondrej Jasek, Vojtech Adam, and Rene Kizek. "Methods for Carbon Nanotubes Synthesis - Review". *J. Mater. Chem.*, 21:15872–15884, (2011).
- [75] Merc Pacios Pujad. *Carbon Nanotubes as Platforms for Biosensors with Electrochemical and Electronic Transduction*. Springer Theses Recognizing Outstanding Ph.D. Research. Springer, 2012.
- [76] D. E. Resasco, W. E. Alvarez, F. Pompeo, L. Balzano, J. E. Herrera, B. Kitiyanan, and A. Borgna. "A Scalable Process for Production of Single-Walled Carbon Nanotubes (SWNTs) by Catalytic Disproportionation of CO on a Solid Catalyst". *Journal of Nanoparticles Research*, 4:131–136, (2002).
- [77] Shahed Reza, Quyen T. Huynh, and Gijs Bosmn. "1/f noise in Metallic and Semiconducting Carbon Nanotubes". *Journal of Applied Physics*, 100:094318, (2006).
- [78] R. Saito, G. Dresselhaus, and M. S. Dresselhaus. *Physical Properties of Carbon Nanotubes*. Imperial College Press, 1998.
- [79] Wahyu Setyawan and Stefano Curtarolo. "High-throughput electronic band structure calculations: Challenges and tools". *Computational Materials Science*, 49:299–312, (2010).
- [80] E. S. Snow, J. P. Novak, M. D. Lay, and F. K. Perkins. "1/f Noise in Single-Walled Carbon Nanotube Devices". *Applied Physics Letters*, 85(18):4172–4174, (2004).
- [81] Navaneetha K. Subbaiyan, Sofie Cambré, A. Nicholas G. Parra-Vasquez, Erik H. Hároz, Stephen K. Doorn, and Juan G. Duque. "Role of Surfactants and Salt in Aqueous Two-Phase Separation of Carbon Nanotubes toward Simple Chirality Isolation". *ACS Nano*, 8(2):1619–1628, (2014).
- [82] Takeshi Tanaka, Hehua Jin, Yasumitsu Miyata, Shunjiro Fujii, Hiroshi Suga, Yasuhisa Naitoh, Takeo Minari, Tetsuhiko Miyadera, and Kazuhito Tsukagoshi. "Simple and Scalable Gel-Based Separation of Metallic and Semiconducting Carbon Nanotubes". *Nano Letters*, 9(4):1497–1500, (2009).
- [83] Sander J. Tans, Alwin R. M. Verschueren, and Cees Dekker. "Room-Temperature Transistor Based on a Single Carbon Nanotube". *Nature*, 393:49–52, (1998).
- [84] Martin Testa-Anta, Miguel A. Ramos-Docampo, Miguel Comesana Hermo, Beatriz Rivas-Murias, and Verónica Salgueiri no. "Raman Spectroscopy to Unravel

- the Magnetic Properties of Iron Oxide Nanocrystals for Bio-related Applications”. *Nanoscale Advances*, 1:2086–2103, (2019).
- [85] Andreas Thess, Roland Lee, Pavel Nikolaev, Hongjie Dai, Pierre Petit, Jerome Robert, Chunhui Xu, Young Hee Lee, Seong Gon Kim, Andrew G. Rinzler, Daniel T. Colbert, Gustavo E. Scuseria, David Tománek, John E. Fischer, and Richard E. Smalley. ”Crystalline Ropes of Metallic Carbon Nanotubes”. *Science*, 273(5274):483–487, (1996).
- [86] Christian Thomsen and Stephanie Reich. ”Raman Scattering in Carbon Nanotubes”. *Topics Apply Physics*, 108:115–232, (2007).
- [87] F. Villalpando-Paez, H. Son, D. Nezich, Y. P. Hsieh, J. Kong, Y. A. Kim, D. Shimamoto, H. Muramatsu, T. Hayashi, M. Endo, M. Terrones, and M. S. Dresselhaus. ”Raman Spectroscopy Study of Isolated Double-Walled Carbon Nanotubes with Different Metallic and Semiconducting Configurations”. *Nano Letters*, 8(11):3879–3886, (2008).
- [88] Sivakumar VM, Abdul Rahman Mohamed, Ahmad Zuhairi Abdullah, and Siang-Piao Chai. ”Role of Reaction and Factors of Carbon Nanotubes Growth in Chemical Vapour Decomposition Process Using Methan - A Highlight”. *Journal of Nanomaterials*, 2010(395191):1–11, (2010).
- [89] Paul A. Warburton. ”The Josephson Effect: 50 Years of Science and Technology”. *Physics Education*, 46(6):669–675, (2011).
- [90] R. Bruce Weisman and Sergei MI Bachilo. ”Dependence of Optical Transition Energies on Structure for Single-Walled Carbon Nanotubes in Aqueous Suspension: An Empirical Kataura Plot”. *Nano Letters*, 3(9):1235–1238, (2003).
- [91] Wim Wenseleers, Igor I. Vlasov, Etienne Goovaerts, Elena D. Obraztsova, Anatolii S. Lobach, and August Bouwen. ”Efficient Isolation and Solubilization of Pristine Single-Walled Nanotubes in Bile Salt Micelles”. *Advanced Functional Materials*, 14(11):1105–1112, (2004).
- [92] Young-Gui Yoon, Paul Delancy, and Steven G. Louie. ”Quantum Conductance of Multiwall Carbon Nanotubes”. *Physical review B*, 66:073407, (2002).
- [93] Min-Feng Yu, Oleg Lourie, Mark J. Dyer, Katerina Moloni, Thomas F. Kelly, and Rodney S. Ruoff. ”Strength and Breaking Mechanism of Multiwalled Carbon Nanotubes Under Tensile Load”. *Science*, 287(5453):637–640, (2000).

- [94] B. Yu. Zaslavsky, L. M. Miheeva, G. Z. Gasanova, and A. U. Mahmudov. "Effect of Polymer Composition on the Relative Hydrophobicity of the Phases of the Biphasic System Aqueous Dextran-Poly(Ethylene Glycol)". *Journal of Chromatography A*, 403:123–130, (1987).
- [95] Ming Zheng. "Sorting Carbon Nanotubes". *Topics in Current Chemistry*, 375(13), (2017).
- [96] Ming Zheng, Anand Jagota, Ellen D. Semke, Bruce A. Diner, Robert S Mclean, Steve R. Lustig, Raymond E. Richardson, and Nancy G. Tassi. "DNA-Assisted Dispersion and Separation of Carbon Nanotubes". *Nature Materials*, 2:338–342, (2003).
- [97] Xinjian Zhou, Ji-Yong Park, Shaoming Huang, Jie Liu, and Paul L. McEuen. "Band Structure, Phonon Scattering and the Performance Limit of Single-Walled Carbon Nanotube Transistors". *Physical Review Letters*, 95(14):146805, (2005).

# APPENDICES

# Appendix A

## Summary of Devices

### A.1 Preparing Substrates from 4-inch Wafer

The first fabrication step for devices is CNT film etching and the next step is metallization. Substrates are needed align marks because making an alignment for CNT film design and metallization design. In order to reduce making align marks for preparing substrates, we fabricate substrates in a 4-inch wafer at a time. Once making same 1 cm by 1 cm designs in a wafer, dicing the wafer to obtain 69 substrates.

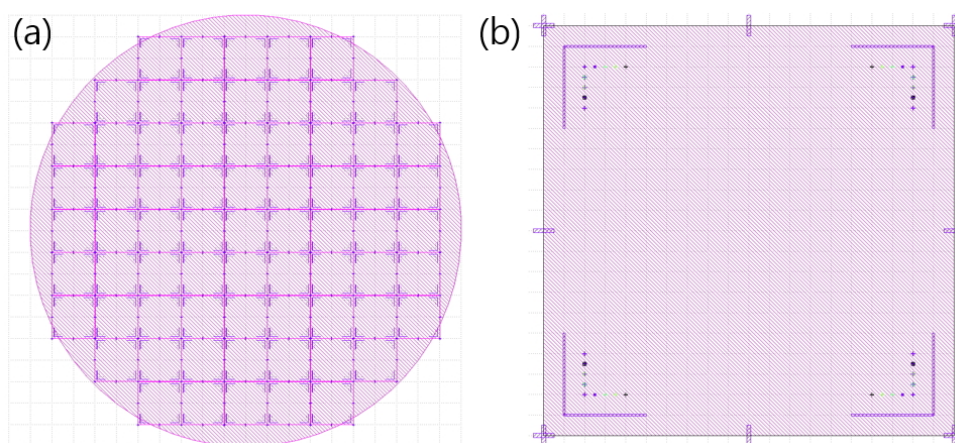


Figure A.1: (a) Drawing for multiple 1 cm by 1 cm substrates. (b) Drawing for an 1 cm by 1 cm substrate.

## A.2 History of Devices

Generation	Period	CNT type	Film Type	Fabrication	Remarks
Gen.1	2018.May.-2018.Jun.	MWNT	LB	MLA	Design protocol for <a href="#">MLA</a> Fabrication practice Resistance > 1 M $\Omega$ Explosion No Josephson effect
Gen.2	2018.Jun.-2018.Aug.	MWNT	LB	EBL	Design protocol for <a href="#">EBL</a> Fabrication practice Annealing effect Explosion No Josephson effect
Gen.3 & Gen.4	2018.Aug.-2018.Nov.	Aligned SWNT	VF	<a href="#">EBL</a> 2-step <a href="#">MLA</a> & <a href="#">MLA</a>	No annealing effect Resistance > 10 k $\Omega$ Explosion No Josephson effect
Gen.5	2018.Nov.-2019.Jan	SWNT	VF	<a href="#">EBL</a> bi-layer	Arm-Pad contact issue Resistance > 10 k $\Omega$ No Josephson effect
Gen.6	2019.Feb.-2019.Jun.	-	-	<a href="#">EBL</a>	Reference Josephson junction Vertical stack Nb-SiO <sub>2</sub> -Nb
Gen.7	2019.Jun.-2019.Aug.	Sorted SWNT	VF	<a href="#">EBL</a> bi-layer, 2-step	Metal dominant film Increasing Pd thickness Cleaning CNT surface Resistance < 1 k $\Omega$ No Josephson effect
Gen.8	2019.Nov.	Sorted SWNT	LB	<a href="#">EBL</a> bi-layer, 2-step	Semiconducting dominant film Sparse <a href="#">LB</a> film Resistance > 1 M $\Omega$
Gen.9	2019.Nov.	Sorted SWNT	VF	<a href="#">EBL</a> bi-layer, 2-step	Metal dominant film No annealing effect Resistance ~ 1 k $\Omega$ No Josephson effect
Gen.10	2019.Nov.-2019.Dec.	Aligned SWNT	VF	<a href="#">EBL</a> bi-layer, 2-step	Cleaned surface Resistance ~ 100 $\Omega$ 2~3x resistance at low temperature

Table A.1: Table of CNT device history.

# Appendix B

## Useful Values

### B.1 SWNT Table [90, 31]

Chirality	$d_t$ (nm)	$E_{11}$	$\lambda_{11}$	$E_{22}$	$\lambda_{22}$	$\lambda_{11}$ UV-vis	$\lambda_{22}$ UV-vis	Remark
(6,4)	0.692	1.420	873	2.146	578	888	583	GaAs 1.43 eV
(7,3)	0.706	1.250	992	2.457	505	1,005	507	
(6,5)	0.757	1.270	976	2.190	566	986	570	InP 1.35 eV
(9,1)	0.757	1.359	912	1.794	691	924	695	
(8,3)	0.782	1.303	952	1.863	665	962	667	
(10,0)	0.794	1.073	1,156	2.307	537	1,175	539	
(9,2)	0.806	1.090	1,138	2.251	551	1,150	555	
(7,5)	0.829	1.211	1,024	1.921	645			
(8,4)	0.840	1.116	1,111	2.105	589	1,125	591	
(10,2)	0.884	1.177	1,053	1.683	737	1,065	739	
(7,6)	0.895	1.107	1,120	1.914	648	1,135	650	
(9,4)	0.916	1.126	1,101	1.716	722	1,117	726	
(10,3)	0.936	0.993	1,249	1.963	632	1,272	638	
(8,6)	0.966	1.057	1,173	1.727	718	1,187	720	
(9,5)	0.976	0.999	1,241	1.845	672	1,267	674	
(7,4)	0.766	2.650	468					
(6,6)	0.825	2.710	458					
(9,3)	0.859	2.430	511					
(8,5)	0.902	2.480	500					
(7,7)	0.963	2.480	500					

Table B.1: Table of SWNT transition energy and wavelength.

## B.2 Physical Constant

$c$ (speed of light)	$2.997\,92 \times 10^8$ m/s
$e$ (electron charge)	$1.602\,176\,62 \times 10^{-19}$ C
$h$ (Planck's constant)	$6.626\,070\,15 \times 10^{-34}$ J·s $4.135\,667\,696 \times 10^{-15}$ eV·s
$\hbar$ ( $h/2\pi$ )	$1.054\,571\,817 \times 10^{-34}$ J·s $6.582\,119\,569 \times 10^{-16}$ eV·s
$k$ (Boltzmann's constant)	$1.380\,649 \times 10^{-23}$ J/K $8.617\,333\,262\,145 \times 10^{-5}$ eV/K
$m_e$ (electron mass)	$9.109\,53 \times 10^{-31}$ kg $0.510\,998\,950\,00$ MeV/c <sup>2</sup>
$m_p$ (proton mass)	$1.672\,621\,923\,69 \times 10^{-27}$ kg $938.272\,088\,16$ MeV/c <sup>2</sup>
$N_0$ (Avogadro's number)	$6.022\,05 \times 10^{23}$ /mol
$R_y$ (Rydberg)	$13.605\,80$ eV
$a_0$ (Bohr radius)	$5.291\,772\,109\,03 \times 10^{-11}$ m
$\Phi_0$ (Magnetic-flux quantum $h/2e$ )	$2.067\,833\,848 \times 10^{-15}$ Wb
$K_J$ (Josephson constant $1/\Phi_0$ )	$483\,597.8484 \times 10^9$ Hz/V
$G_0$ (conductance quantum $2e^2/h$ )	$7.748\,091\,729 \times 10^{-5}$ S
$1/G_0$ ( $h/2e^2$ )	$12.906\,4037$ k $\Omega$